Engineering Human Neural Circuits with Single-Cell Precision

Investigations of Neuronal Dynamics, Development and Interactions *In Vitro*

Doctoral thesis

to obtain a doctorate (PhD)

from the Faculty of Medicine

of the University of Bonn

Johannes Striebel

from Bühl, Germany

2026

Written with authorization of

the Faculty of Medicine of the University of Bonn

First reviewer: Prof. Dr. Volker Busskamp

Second reviewer: Prof. Dr. Andreas Offenhäusser

Day of oral examination: February 5th, 2026

From the University Eye Hospital Bonn

To my family and especially my uncle who helped ignite
my fascination for nature but had to leave us far too early.

Table of contents

List of abbreviations

AI	Artificial intelligence
AMPA	α-amino-3-hydroxy-5-methyl-4-isoxazolepropionic acid
ANOVA	Analysis of variance
AP	Action potential
AP5	(2R)-amino-5-phosphonovaleric acid
Ara-C	Cytosine β-D-arabinofuranoside hydrochloride
ATFB-NHS	N-Succinimidyl 4-azido-2,3,5,6-tetrafluorobenzoate
BDNF	Brain-derived neurotrophic factor
CBX	Carbenoxolone
CC	Correlation coefficient
CEPT	Cocktail for improved cell survival comprised of chroman 1, emricasan, polyamines, and trans-ISRIB
CIP	Calf intestinal phosphatase
CMOS	Complementary metal-oxide semiconductor
CNS	Central nervous system
DIO	Double-floxed inverse open reading frame
DLR	German Aerospace Center
DMEM	Dulbecco’s modified Eagle’s medium
DNA	Deoxyribonucleic acid
Dox	Doxycycline
DPBS	Dulbecco's phosphate-buffered saline

eDIO	Double-floxed inverse open reading frame under the EF1α promoter
EEG	Electroencephalography
EGFP	Enhanced green fluorescent protein
ESA	European Space Agency
EtOH	Ethanol
FACS	Fluorescence activated cell sorting
FBS	Fetal bovine serum
fChrimson	Red-light shifted channelrhodopsin
fMRI	Functional magnetic resonance imaging
FNN	Feedforward neural network
GDNF	Glial cell line-derived neurotrophic factor
HD-MEA	High-density microelectrode array
HEPES	N-(2-Hydroxyethyl)piperazine-N′-(2-ethanesulfonic acid)
hiPSC	Human induced pluripotent stem cell
iNGN	Induced neurogenin cell line
ISI	Interspike interval
ISS	International Space Station
KL	Kullback-Leibler
LTD	Long-term depression
LTP	Long-term potentiation
MEA	Microelectrode array

ML	Machine learning
MRI	Magnetic resonance imaging
mRNA	Messenger ribonucleic acid
NBQX	2,3-dioxo-6-nitro-7-sulfamoyl-benzo[f]quinoxaline
NMDA	N-methyl-D-aspartic acid
PAAm	Poly(allylamine hydrochloride)
PCR	Polymerase chain reaction
PDL	Poly-D-lysine
PDMS	Polydimethylsiloxan
PFA	Paraformaldehyde
PFOCTS	Trichloro(1H,1H,2H,2H-perfluorooctyl)silane
PGMEA	Propylene glycol methyl ether acetate
PR	Participation ratio
PVP	Polyvinylpyrrolidone
RH	Relative humidity
RNA	Ribonucleic acid
ROCK	Rho-associated, coiled-coil containing protein kinase
RT	Room temperature
SAHC	Short-Arm Human Centrifuge
SEM	Standard error of the mean
SNAP	Single-Neuron Network Assembly Platform

TBS	Theta burst stimulation
tdTomato	Tandem-dimer tomato
TetOn	Tetracycline inducible promoter system
UV	Ultraviolet
ZARM	Center of Applied Space Technology and Microgravity

1. Introduction

1.1 Neuroscience *in vitro*

The brain is a complex biological system and a specialized organ with many intricate capabilities. Since the discovery of the major functional building blocks of the nervous system - the neurons - great progress has been made in neuroscience (Ramón y Cajal, 1888; Yuste, 2015). Researchers have discovered that there are many different types of neurons in the central nervous system (CNS) that carry out specialized tasks. Among these are excitatory and inhibitory neurons, each characterized by unique biophysical and functional properties, as well as many supporting cells, such as glial cells (Stevens et al., 2021). For instance, various specialized neuron types collaborate to capture light in the retina, convert it into an electrical signal, further process it and transfer it to the brain, where an internal representation of the observed image is formed (Baden et al., 2019). This information is then combined with other streams of information, initiating subsequent decision-making processes. As outlined, there are many levels, anatomical and functional, in the nervous system that work together to perform complex tasks. All levels and parts in this system are closely connected and collaborate to function: from the ions necessary to generate a neuron's electrical signals, called action potentials (APs) or spikes, over the synapses that transmit signals between neurons to larger ensembles, such as the retina or visual cortex, which carry out processing. Due to the complexity of these circuits, mapping their anatomical and functional properties remains a significant challenge (Kramer and Flavell, 2024). Clinically, both, neuronal dysfunction and loss, are linked to numerous disorders, highlighting the importance of understanding the underlying mechanisms at cellular and network levels to develop more effective treatments (Zoghbi, 2021). Furthermore, concepts and ideas from this field of study have inspired many other fields and contributed to the development of artificial intelligence (AI) (Hassabis et al., 2017).

Many questions and phenomena in neuroscience remain unanswered or are not sufficiently understood, often due to experimental limitations (Figure 1-1). Different methodological approaches are used to study neurons and the nervous system (Chiaradia and Lancaster, 2020). *In vivo* neuroscience has provided significant insight into the

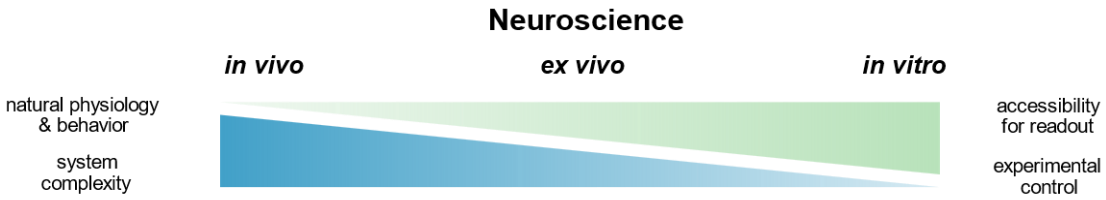

Figure 1-1: Experimental approaches to neuroscience. Most experimental neuroscience research can be categorized according to the mode of the experiments with its specific advantages and limitations.

mechanisms and operating principles of the brain and the peripheral nervous system. The advantage of *in vivo* studies is that neuronal processes can be observed in a natural setting, such as in a freely behaving animal. However, these studies are limited by the accessibility of the neuronal system for recording and intervention. Due to the complexity of the interplay between different brain areas and cell types, it is difficult to observe all processes simultaneously. Thus, it is not possible to have full control over the experiment. *Ex vivo* studies have the advantage of easier control of experimental parameters and offer greater accessibility of the system for measurement, though they face limitations of their own. These preparations are physiologically similar to *in vivo* settings. However, natural inputs, as in a freely behaving animal, are mostly unavailable. *In vitro* studies, on the other hand, have the advantage of tighter control over experimental parameters. They offer greater accessibility for intervention and signal readout, as well as reduced system complexity. However, the *in vitro* situation is simplified and the physiology is less comparable to the natural *in vivo* setting. It also mostly lacks the interplay between other parts of the nervous system.

Depending on the topic of study and the specific question we want to answer, the *in vitro* approach can be the most suitable method for investigation because of the previously mentioned advantages. Applications such as drug screening, disease modeling, the precise study of neuronal interactions like synaptic processes, and the detailed study of information processing in small-scale networks are well suited to *in vitro* analysis and might be more accessible therein. Moreover, the fast and flexible experimental methods of *in vitro* models make them applicable for many different settings and allow for the engineering of setups according to need. In addition, large batches of samples can often be prepared more easily which contributes to the robustness of the results. Though, current *in vitro* models still have limitations. An apparent drawback is their inherently

stochastic formation and resulting random network architecture, which cannot be reproduced and precisely replicated between samples. This makes comparisons and analyses challenging, especially when examining information processing and detailed neuronal interactions. Controlling network topology was shown to produce predictable, and stable activity patterns (Duru et al., 2022; Ihle et al., 2022).

Early on, scientists used electrodes placed close to neurons *in vivo* and *in vitro* to measure and stimulate their electrical activity (Adrian, 1928; Berger, 1929; Piccolino, 1997). The development of the patch clamp method enabled more detailed measurements of the electrophysiological processes of single neurons, including intracellular measurements, and allowed for the investigation of ion channels in the cell membrane (Hamill et al., 1981; Neher and Sakmann, 1976). Technological advances in microfabrication enabled to arrange dozens of microelectrodes on a culture surface to record cultured neurons (Thomas et al., 1972). These microelectrode arrays (MEAs) allowed researchers to monitor the electrophysiological activity of neuronal networks *in vivo* and *in vitro* on a large scale over extended periods of time (Pine, 1980; Strumwasser, 1958). In parallel, calcium imaging was developed and offers simultaneous monitoring of the activity of large numbers of neurons, albeit with much lower time resolution (Ashley and Ridgway, 1968; Tsien, 1980). Over the past decade, substantial progress has been made in developing high-resolution readout techniques for both *in vivo* and *in vitro* neuronal systems. These high-density microelectrode arrays (HD-MEAs) offer high electrode counts, and subcellular resolution while maintaining the high sampling rate. Together, this makes it possible to study *in vivo* and *in vitro* networks in more detail (Jun et al., 2017; Litke et al., 2004; Müller et al., 2015). Unlike patch-clamp techniques, MEA technology offers robust, non-invasive extracellular electrophysiological recordings of whole networks for the long-term study of neural network dynamics with high-resolution and in real-time. However, these advances have not solved all the limitations of *in vitro* systems, such as the irreproducible structure of cultured neuronal networks.

Another advance in the field of *in vitro* neuroscience was the development of induced pluripotent stem cells (iPSCs) and protocols for differentiating them into diverse neural cell types (Habibey et al., 2022a). iPSCs can be generated from different species in large quantities, providing an unlimited source of cells (Takahashi et al., 2007; Takahashi and

Yamanaka, 2006). Importantly, human iPSCs (hiPSCs) can be generated from somatic cells and especially from easily accessible cell sources, such as skin biopsies or blood, to create a personalized stem cell line (Robinton and Daley, 2012). Genetic modifications and specialized culture protocols can guide the development of these cells into specific lineages and cause them to differentiate into desired cell types. Differentiating stem cells into mature, postmitotic neurons is a lengthy process, often requiring extended culture times (Canals et al., 2018; Zhang et al., 2013). However, the process can be accelerated through the forced expression of key neurogenic transcription factors (Busskamp et al., 2014; Pang et al., 2011; Zhang et al., 2013). For instance, introducing and overexpressing the transcription factors Neurogenin-1 and Neurogenin-2 under an inducible promoter system causes hiPSCs to differentiate into postmitotic excitatory bipolar neurons within four days with over 90 % efficiency (Busskamp et al., 2014). This well-characterized induced Neurogenin (iNGN) cell line provides a homogeneous neural population (Busskamp et al., 2014; Kutsche et al., 2018; Lam et al., 2017). These neurons require a maturation period during which they establish network connectivity and function. After 21 days, iNGN neurons possess functional synapses (Lam et al., 2017). Adjusting culturing conditions, such as adding specific small molecules, can also be used alone or in combination with genetic modifications to create the desired cell type. HiPSCs can differentiate into virtually any cell type in the human body (Williams et al., 2012). Notably, hiPSCs raise fewer ethical concerns than embryonic stem cells (ESCs) because they are derived without the use of embryos (Lo and Parham, 2009).

The development of hiPSC-derived neurons has facilitated to create large quantities of homogeneous human neural network cultures in parallel. Combining these cultures with MEA technology allows for the longitudinal monitoring of the networks' electrophysiological activity over extended periods (> 100 days). Even culture periods exceeding one year have been reported (Hales et al., 2010). Researchers have begun to consider how to engineer these *in vitro* cultures to generate circuits of interest (Habibey et al., 2022a; Nikolakopoulou et al., 2020). This has also paved the way for the controlled co-culture of different neuronal and glial cell types or populations. There are various methods to control the structure of *in vitro* networks and guide neuronal growth (Aebersold et al., 2016). Approaches include surface functionalization with molecules or proteins via micropatterning or the use of microfluidics. Microfluidic structures consist of various

compartments, reservoirs, and openings that are connected by channels, which are usually in the size range of hundreds of nanometers to millimeters. These structures can be fabricated from biocompatible materials, such as polymers, glass, and silicon. Microfluidic structures are routinely used for various applications, such as sensing, analysis, and fabrication, in chemistry and biology. Since cells can be incorporated into microfluidic compartments, this technology has been adopted for developing “lab-on-a-chip” and “organ-on-a-chip” technologies. Inspired by these developments, neuroscientists have also begun using microfluidics to structure neuronal networks (Aebersold et al., 2016; Habibey et al., 2022a). Neurons are seeded into microwells and kept in compartments, allowing neurites to grow along microchannels and connect to neighboring compartments. This physical confinement provides a reliable and stable method for structuring networks. Interfacing microfluidics with MEAs creates structured networks on a chip and aligns them over recording electrodes for improved readout, leading to so-called “brain-on-a-chip” systems. Cell types or populations can be kept separate and made to interact in a defined way to give a desired structure to a network. However, controlling the network structure did so far not extend to the level of individual cells; thus, tight control of network connectivity remains elusive.

MEAs can elicit APs by electrically stimulating surrounding cells via the electrodes (Tehovnik, 1996). This method is convenient because stimulation and recording can be performed simultaneously using the same system. However, due to the physical nature of electrical stimulation, this method cannot target a specific neuron or subgroup of neurons, as the electrical pulse spreads through the surrounding culture medium and can stimulate any neuron in proximity to an electrode. A more targeted approach is using optical stimulation methods like optogenetic tools to elicit APs from neurons (Emiliani et al., 2022; Thompson et al., 2014). Optogenetic actuators, ion channels or ion pumps that act upon light of a specific wavelength, were first discovered in bacteria and algae. Researchers have demonstrated that these actuators can be expressed in cells of other organisms, for example in neurons and that shining light on them elicits APs (Boyden et al., 2005; Nagel et al., 2002, 2003). This method allows for more targeted stimulation of neurons and using optogenetic actuators sensitive to different wavelengths enables multiplexing. Optogenetic actuators can be expressed in neurons *in vivo* and *in vitro*. For example, they are used in animal models, or in hiPSC-derived neurons on MEAs. Through combination

with patterned light stimulation, like holographic stimulation, single neurons in a network can be activated separately (Schmieder et al., 2022).

Engineered *in vitro* neuronal systems on MEAs have the potential to help answer many neuroscientific questions, but more work is necessary to overcome their limitations. Here, I present several studies in which I aim to investigate to what extend these systems can be used as a model in neuroscience research and how they can be improved to expand their applicability as a tool for approaching fundamental issues in various subfields. My overarching goal was to develop a method to reproducibly create and study *in vitro* neural circuits with single-cell resolution. As explained in this section, such systems could have advantages in a more detailed investigation of neuronal interactions. To approach this problem in a systematic way, I started out by working with established random neuronal culture systems. First, I asked whether altered gravity has an effect on neuronal function. MEA technology is a highly flexible tool and would be well suited for answering a diverse set of neuroscientific questions, especially about the influence of altered gravity, that needs specialized platforms for induction. So far studies had experimental limitations that could be overcome with MEA technology. A better understanding of the influences of altered gravity on neuronal physiology and improved methods for their study could potentially benefit astronaut health and space travel. Moreover, this could lead to a better understanding of neuronal mechanisms in response to mechanical stimuli with the potential to develop interventions. Building on the expertise gained during this study, especially the observation of a dynamic morphological and functional development of neuronal circuits on MEAs, I asked how the development of *in vitro* circuits unfolds in more detail. Specifically, I wanted to see if these networks recapitulate characteristics of *in vivo* neuronal development and maturation, making them an apt model system. Still, a main question in neuroscientific research is how structure and function in neural circuits are connected (van Atteveldt et al., 2021; Rosenthal et al., 2018; Sporns, 2013), and how they (co-)develop over time. Detailed studies employing HD-MEAs to quantify morphological and functional changes of unconstrained random networks were missing so far. The striking observation of substantial changes in network morphology over time further emphasized the need for a method that can yield reproducible circuit architectures, ideally down to the single-neuron level. Looking at the developmental trajectory of *in vitro* neuronal networks, I asked whether our insights could be used to modify such systems

so that plasticity and learning can be induced. More specifically, I asked whether imposed and controlled network architecture as well as continuous stimulation are relevant factors and sufficient to induce measurable plasticity effects. So far, only some contradictory results have been reported in this area, and only random cultures with limited stimulation times were used. As mentioned, I was especially interested to see if and how neuronal network morphology can be controlled down to the single-cell level. This has not been achieved so far and posed many technical challenges. Such a method might allow for more detailed and reproducible investigation of neuronal interactions. Particularly, I wanted to employ the methodological advances and learnings from the previous studies to build neuronal circuits from the bottom up at single-cell resolution and investigate if they would be useful for precise investigation of neuronal physiology. For example, I wondered if such circuits are more sensitive to interventions. Further, I was interested in their applicability to study otherwise difficult to access phenomena like ephaptic coupling and whether its effects can be measured. Another objective was to see if such a method can be applied to construct more complex circuits and if such circuits can be stimulated precisely.

1.2 Neuroscience in altered gravity

The content of the following section has also been published in Striebel et al. (2023) on which I am a first author under a CC-BY 4.0 license.

Astronauts in space face various challenges, one of them is the exposure to extreme environmental conditions. The most prominent influences are both microgravity and hypergravity, but also elevated radiation levels. These factors significantly impact human health, leading to diminished muscle function (LeBlanc et al., 2000), weakened immune responses (Crucian et al., 2000; Paulsen et al., 2010), and bone density loss (Sibonga, 2013; Smith et al., 1999). Additionally, alterations in brain health and cognitive abilities have been reported (Clément, 2011; Van Ombergen et al., 2017, 2018; Popova et al., 2020; Roberts et al., 2017; Wollseiffen et al., 2019).

Significant progress has been made in mitigating adverse health effects in astronauts to expand space travel. However, the influence of altered gravity on neuronal function

remains poorly understood. Space travel has been shown to affect both brain structure and function. Observed symptoms include spatial disorientation, difficulties with vision and motor control, reduced concentration, and overall cognitive decline (Garrett-Bakelman et al., 2019; Kanas and Manzey, 2008; Roy-O'Reilly et al., 2021). Magnetic resonance imaging (MRI) studies in astronauts have revealed structural modifications in gray matter and reduced neuronal plasticity after long-duration space flight to the International Space Station (ISS) (Demertzi et al., 2016; Van Ombergen et al., 2017; Roberts et al., 2017). Of note, anatomical alterations like an upward shift of the brain and changes in volumes have been reported as well (Van Ombergen et al., 2018; Roberts et al., 2017). Accordingly, it is believed that prolonged exposure to altered gravity may lead to lasting neurodegenerative effects (Roberts et al., 2020). Thus, there is a great need to better understand neuronal processes and dynamics under altered gravity conditions. More specifically, it is essential to investigate how different gravitational environments influence neuronal cellular mechanisms.

Simulated micro- and hypergravity have been used to study the response of different cell types (Galimberti et al., 2006; Maier et al., 2015). For example, cells of the CNS have been investigated morphologically under these conditions. Neurons show alterations in cytoskeletal structures, including microtubule and actin networks (Rösner et al., 2006), leading to changes in neurite extension, neurite surface area, and the distribution of microtubule filaments (Genchi et al., 2015; Pani et al., 2013). Cytoskeletal stability is important to cell physiology and plays a crucial role in maintaining cellular function. Similarly, astrocytes exhibit morphological changes, altered migration patterns, and reduced reactivity in response to hypergravity, which have also been linked to modifications in cytoskeletal dynamics (Lichterfeld et al., 2022). Since cytoskeletal structures are integral to various stages of neuronal development, disruptions may affect the formation, maintenance, or elimination of functional networks and synaptic connections. Consequently, neuronal signal transmission, a fundamental process in brain function, might be influenced. Understanding how gravity variations impact neuronal communication is critical, as disruptions in electrophysiological activity are often associated with neurological and neurodegenerative disorders (Babiloni et al., 2020; Chong et al., 2011).

Despite these findings, there remains a limited understanding of how exposure to altered gravity affects neuronal function, especially at the network level. Studies of intra- and extracellular recordings of earthworm and rat neurons during experiments in the Bremen drop tower facility at the Center of Applied Space Technology and Microgravity (ZARM) and parabolic flights have suggested that AP propagation velocity varies depending on gravitational conditions (Meissner and Hanke, 2002, 2005). A standing hypothesis is that microgravity may increase the frequency of spontaneous neuronal activity. Such changes could be linked to increased cell membrane fluidity in microgravity, as observed in neurons during parabolic flights (Sieber et al., 2014) and in lipid membranes in a sounding rocket providing 6 min of microgravity (Kohn et al., 2017; Kohn and Hauslage, 2019). A decrease in gravitational forces might enhance membrane excitability by increasing the probability of ion channel opening, thereby lowering the threshold for AP generation. Changes in intracellular calcium levels have also been used to assess neuronal activity. Studies using SH-SY5Y neuroblastoma cells reported changes in calcium permeability under microgravity. This was the case in both simulated microgravity generated using a clinostat and during parabolic flights that subjected cells to alternating microgravity and hypergravity phases lasting approximately 22 s each (Hauslage et al., 2016). Additionally, research on human subjects undergoing peripheral nerve stimulation indicated modified synaptic and axonal conductivity and excitability in response to altered gravity (Ritzmann et al., 2017).

These studies highlight the need for further detailed investigation. However, accurately measuring the electrophysiological activity of neurons and neural networks in altered gravity environments presents significant challenges. Current platforms for gravity research, including drop towers, parabolic flights, sounding rockets, and centrifuges that produce altered gravity conditions, impose strict constraints on experimental hardware, including size limitations and structural durability requirements, as well as restricted access to essential support systems, such as power supply. Additionally, any biological experiment setup must meet stringent requirements to maintain live samples. MEA technology might be a suitable method for investigation of human neuronal samples in altered gravity. Previous experiments using MEA technology to study maize root responses to microgravity and hypergravity revealed significant alterations in AP duration

and propagation speed under these conditions (Masi et al., 2015), indicating its applicability.

1.3 *In vitro* networks as a model for brain development

The content of the following section has also been published in Habibey et al. (2022b) on which I am a first author under a CC-BY 4.0 license.

Understanding human brain development is inherently challenging, and a major obstacle is the limited availability of empirical data. Tissue is only available in rare cases and most studies rely on non-invasive imaging techniques like MRI for morphological and functional studies. Functional studies looking at electrophysiological activity are limited to methods that are lacking spatial and time resolution, like functional MRI (fMRI) or electroencephalography (EEG). Detailed studies using electrodes directly inserted in the brain are very limited because of ethical reasons and can only in very rare cases be done over extended periods of time (Manzini et al., 2021; Mezinska et al., 2021).

Complex neural circuits in the brain arise from highly organized and dynamically changing connections between neurons (Bassett and Sporns, 2017; Kriegeskorte and Douglas, 2018). The basis for the developmental trajectory is governed by genetic mechanisms (Tau and Peterson, 2010), but other factors and functional features influence the development early on. Overall, there is a generally foreseeable sequence of developmental stages an individual passes through (Gozdas et al., 2019; Kim and Paredes, 2021; Martinez and Sprecher, 2020; Stiles and Jernigan, 2010). These self-organization principles have been investigated *in vivo* by both human and animal studies (Bassett and Gazzaniga, 2011; Huber et al., 2021; Latifi et al., 2020; Levakov et al., 2021; Li et al., 2021; Tau and Peterson, 2010).

Human brain development encompasses a series of key events: expansion and specialization of neural progenitors, migration of immature neurons, outgrowth and guidance of axons, development of dendritic structures, and the formation of synaptic connections (Budday et al., 2015; Jiang and Nardelli, 2016; Raybaud et al., 2013; Silbereis et al., 2016). Of note, initially a large number of connections between neurons are generated, but many of them are lost in a process called synaptic pruning to sculpt

organized and efficient circuits (Budday et al., 2015; Craig et al., 2006; Craik and Bialystok, 2006; Silbereis et al., 2016). Another characteristic in mammals is that excitatory neurons mature relatively early during embryogenesis, whereas the maturation of inhibitory GABAergic interneurons is delayed (Warm et al., 2022). Functional activity in the developing cortex reflects these processes, with coordinated glutamatergic bursts appearing mid-gestation and subsequently declining as GABAergic inhibition becomes more prominent (Corlew et al., 2004; Kirwan et al., 2015; Luhmann et al., 2016; Teppola et al., 2019). Furthermore, GABAergic transmission initially has a depolarizing (excitatory) effect, transitioning to inhibition as networks mature during early postnatal life (Ganguly et al., 2001; Zafeiriou et al., 2020).

In vitro systems are a route for developmental investigations allowing more controlled analysis of developing neural circuits with reduced complexity (Hattori, 2013; Lancaster et al., 2013; Ndyabawe and Kisaalita, 2019; Pașca, 2018; Pastrana, 2013). Also in this case, the use of hiPSC-derived neuronal cultures offers an option to make these systems mimic human physiology closer, including aspects of early brain development (Odawara et al., 2014; Ronchi et al., 2021; Sasaki et al., 2019; Schmieder et al., 2022). Technological advances in stem cell biology have positioned these culture systems as valuable alternatives to animal models (Ardhanareeswaran et al., 2017), especially for studying human-specific disease mechanisms (Nikolakopoulou et al., 2020). Such human disease models aid in translation of the generated findings. These two- or three-dimensional neural models are typically generated from human ESCs (hESCs) (Ilic and Ogilvie, 2017) or hiPSCs (Hockemeyer and Jaenisch, 2016; Shi et al., 2016). In particular, three-dimensional structures like brain organoids attracted increased interest as an *in vitro* model system for development and function (Qian et al., 2019).

For these cultures to serve as reliable models of neurodevelopment and disease, long-term functional assessment using electrophysiological tools is essential (Habibey et al., 2022c; Mossink et al., 2021; Schmieder et al., 2022). While patch-clamp recordings have been employed to track iNGN-derived neuron functionality across extended timeframes (Lam et al., 2017), they lack the scalability needed to non-invasively monitor entire networks over weeks or months (Habibey et al., 2020, 2022c). MEAs offer a non-destructive approach to record extracellular activity from primary (Habibey et al., 2015a,

2017; Latifi et al., 2016), stem-cell derived (Habibey et al., 2022c; Odawara et al., 2014; Schmieder et al., 2022), and organotypic brain slice cultures (Mannal et al., 2021; Steidl et al., 2006).

When culturing neuronal networks *in vitro*, developmental changes over time can be observed; the most prominent one being morphological changes of the network. Since morphological reorganization is a key aspect in *in vivo* brain development, we were wondering if and which features of brain development are mirrored *in vitro.* When hiPSC-derived neurons are cultured on HD-MEAs, age-dependent increases in spontaneous activity and synchronized bursting have been observed (Lu et al., 2019). These electrophysiological parameters can serve as functional signatures to distinguish between healthy and disease-related phenotypes (Ronchi et al., 2021), making them highly informative for tracking (functional) network development (Akarca et al., 2022). Despite this, long-term electrophysiological investigations of primary or stem cell-derived cultures remain limited (Amin et al., 2016; Habibey et al., 2015b, 2015a; Lu et al., 2019; Odawara et al., 2014, 2016b).

1.4 *In vitro* plasticity and learning

Going a step further, I asked whether *in vitro* neuronal networks could serve as a platform to investigate higher-order processes such as plasticity and learning. Fundamental mechanisms of long-term potentiation (LTP) and depression (LTD) have been demonstrated in cultured networks (Chiappalone et al., 2008; Odawara et al., 2016a). Closed-loop preparations have even been used to control robots or virtual agents navigating their environments (Demarse et al., 2001; Novellino et al., 2007). More recently, a study reported training a cultured network to play the computer game Pong (Kagan et al., 2022), a claim that sparked vigorous debate about experimental interpretation, reproducibility and proper representation of the claims (Balci et al., 2023; Kagan et al., 2023). Negative results have likewise been published, highlighting both the experimental difficulties of such studies, and the need for careful analysis and interpretation as well as systematic investigation (Wagenaar et al., 2006). Parallel to these efforts, microphysiological systems employing brain organoids or engineered neuronal

networks are attracting growing interest as potential substrates for biological computing (Cai et al., 2023; Li et al., 2025; Smirnova et al., 2023).

Most prior work, however, has relied on spontaneously formed cultures with no imposed architecture, leaving network organization entirely to self-assembly. Reports of substantial morphological remodeling over time (Habibey et al., 2022b), have rarely been addressed, even though such structural drift could affect learning performance and complicate stable electrode readouts.

To overcome these limitations, I set out to create a microfluidic-MEA platform that enforces a stable spatial arrangement of neuronal populations in a plasticity experiment. Specifically, my goal was to approximate a feedforward neural network (FNN) in a dish, an architecture that is both reflective of hierarchical motifs in the brain (Luo, 2021; Serre et al., 2007) and foundational in machine learning (ML), where it is often used for pattern recognition and classification. A fixed, multilayered circuit combined with a well-defined task should facilitate direct comparisons between biological data and theoretical or computational models. Moreover, through automated recording and stimulation sessions, I sought to make extended stimulation over long time periods possible. As a first experimental paradigm, I asked whether these structured cultures could perform a simple classification task: distinguishing between two spatially distinct stimulation patterns. Key questions included how such a network adapts or “learns” over time. I was also interested if it would be possible to infer a basic biological learning rule from its dynamics. And, more specifically, if these rules akin to error back-propagation, a central concept of ML, emerge in living neural circuits (Lillicrap et al., 2020).

The experiment was conceptualized and investigated together with Dr. Christoph Miehl in the lab of Prof. Dr. Brent Doiron at the University of Chicago.

1.5 Enabling bottom-up assembly of defined neural networks for analyzing ephaptic coupling

Content of the following section is currently in press Striebel et al. (2025b) and is partly published as a preprint under a CC-BY-NC-ND 4.0 license Striebel et al. (2025a).

Ephaptic coupling refers to the modulation of neuronal activity by endogenous electric fields generated within the tissue itself (Anastassiou and Koch, 2015; Weiss and Faber, 2010). This form of interaction, distinct from chemical and electrical synapses (Figure 1-2), has been proposed to play a role in brain computations (Anastassiou et al., 2011; Pinotsis and Miller, 2023; Weiss and Faber, 2010), sensory processing such as olfaction (Bokil et al., 2001) and vision (Kamermans et al., 2001; Vroman et al., 2013), and even cardiac conduction (Ivanovic and Kucera, 2021; Veeraraghavan et al., 2014). Moreover, disruptions in ephaptic signaling have been linked to pathological conditions including epilepsy (Dudek et al., 1998; Shivacharan et al., 2021) and arrhythmias (Hoagland et al., 2019; Veeraraghavan et al., 2018). Despite its wide-ranging implications, ephaptic coupling remains challenging to study due to the technical difficulties in isolating and manipulating endogenous fields both *in vivo* and *in vitro*.

Since ephaptic interactions are mediated by local field potentials generated by ionic currents and membrane polarization, they are not easily subjected to targeted experimental manipulation. More specifically, electric fields are difficult to block or shield between neurons *in vivo* and *in vitro*. Computational modeling was used broadly to investigate how such fields might influence neuronal excitability and synchronization (Anastassiou et al., 2010; Capllonch-Juan and Sepulveda, 2020; Lin and Keener, 2013; Pinotsis and Miller, 2023; Rabinovitch et al., 2024; Schmidt et al., 2021; Schmidt and Knösche, 2019; Stacey et al., 2015; Wei and Tolkacheva, 2022). Only a few experimental studies have succeeded in probing these effects, often by applying exogenous fields or using specialized techniques (Anastassiou et al., 2011; Blot and Barbour, 2014; Han et al., 2018, 2020). The first experimental investigations of ephaptic effects were carried out on crab nerves that are easier to handle because of their size (Katz and Schmitt, 1940).

Despite accumulating evidence for ephaptic contributions to olfactory processing (Bokil et al., 2001), retinal signaling (Kamermans et al., 2001; Vroman et al., 2013), and potentially

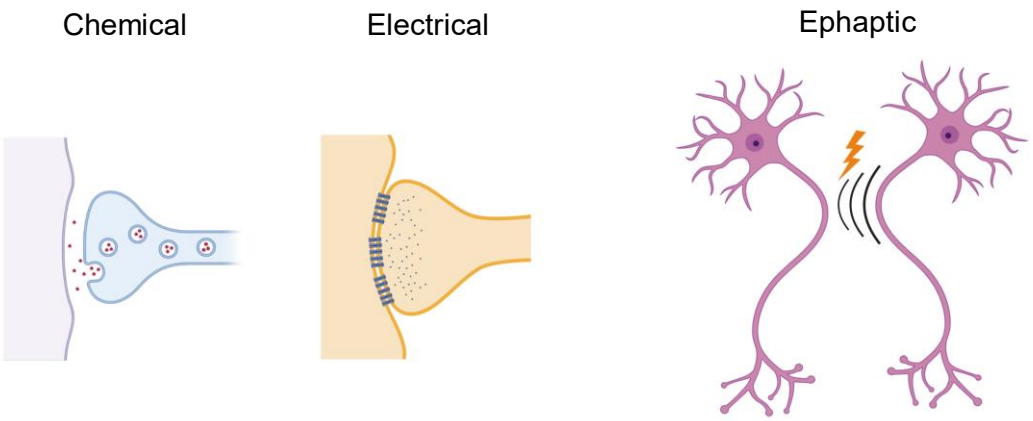

Figure 1-2: Modes of neuronal interaction. The main mode of signal transmission in the nervous system is via chemical synapses. Neurotransmitters are released by the presynaptic compartment into the synaptic cleft and activate the postsynaptic cell. Electrical synapses or gap junctions allow direct transfer of ions between neurons. Ephaptic coupling is mediated by electrical fields that occur naturally during electrophysiological activity of neuronal substrates. *Partly created in BioRender. Kunze, S. (2025) https://BioRender.com/nansftm*

higher-order computations (Anastassiou et al., 2011; Pinotsis and Miller, 2023; Weiss and Faber, 2010), experimental insights into its functional relevance remain limited. The same applies for its role in the heart, where it may supplement gap junction-mediated conduction (Lin et al., 2022). Ephaptic mechanisms have also been implicated in pathological states such as seizures (Dudek et al., 1998; Rabinovitch et al., 2024; Shivacharan et al., 2021; Stacey et al., 2015; Subramanian et al., 2022) and cardiac arrhythmias (Hoagland et al., 2019; Lin and Keener, 2013; Veeraraghavan et al., 2018; Wei and Tolkacheva, 2022).

Traditional *in vitro* electrophysiology offers accessible and controllable environments for neural studies, but spontaneous network formation often results in high variability and low reproducibility. To overcome the limitations of uncontrolled *in vitro* networks, such as batch-to-batch architectural variability, complexity in data interpretation, and morphological changes over time (Habibey et al., 2022b), I developed the Single-Neuron Network Assembly Platform (SNAP). This method allows the construction of reproducible neural circuits with single-cell level accuracy, offering a new level of control for studies of non-synaptic interactions in human iPSC-derived neuronal systems. By generating close axonal contact in defined geometries, I created bottom-up circuits that allowed me to explore ephaptic interactions under well-controlled conditions.

2. Material and methods

The presented thesis is based on a corpus of work that has largely been published already. The methods described here can also be found in these publications (Habibey et al., 2022b; Striebel et al., 2023, 2025a, 2025b).

2.1 Materials

Table 2.1: Reagents

Reagent	Manufacturer	Order No.
Cell culture		
Accutase™	Sigma-Aldrich/Merck	A6964
AP5	Tocris	0105
Ara-C	Sigma-Aldrich/Merck	C6645
Ascorbic acid	Sigma-Aldrich/Merck	A0278
BDNF	Thermo Fisher Scientific	450-02-10
Blasticidin	Thermo Fisher Scientific	A1113903
BrainPhys™ medium and NeuroCult™ SM1 supplement kit	STEMCELL Technologies	05792
Carbenoxolone	Sigma-Aldrich/Merck	C4790
Chroman 1	MedchemExpress	HY-15392
DMEM, high glucose, GlutaMAX™ Supplement, pyruvate	Thermo Fisher Scientific	31966021
Doxycycline hyclate	Sigma-Aldrich/Merck	14021705
DPBS without Ca, Mg (DPBS-/-)	Thermo Fisher Scientific	14190169
Dulbecco's phosphate-buffered saline with Ca, Mg (DPBS+/+)	Thermo Fisher Scientific	14040133
Emricasan	Cayman Chemical	22204
Fetal Bovine Serum (FBS)	Thermo Fisher Scientific	A5256801
GDNF	Thermo Fisher Scientific	450-10-10
Laminin	Sigma-Aldrich/Merck	L2020
Lipofectamine™ MessengerMAX™	Thermo Fisher Scientific	LMRNA001
Matrigel® hESC-qualified Matrix	Corning	354277
mFreSR™	STEMCELL Technologies	05855
mTeSR™1 medium	STEMCELL Technologies	85850
N-2 Supplement (100x)	Thermo Fisher Scientific	17502048
NBQX disodium salt	Tocris	1044
Opti-MEM™ I Reduced Serum Medium	Thermo Fisher Scientific	31985062
PCR Mycoplasma Test Kit II	AppliChem GmbH	A8994
Penicillin-Streptomycin	Thermo Fisher Scientific	15140122
Polyamine Supplement (1000x)	Sigma-Aldrich/Merck	P8483
Poly-D-lysine	Sigma-Aldrich/Merck	A-003-E

Puromycin	Thermo Fisher Scientific	A1113803
ROCK inhibitor Y-27632 Dihydrochloride	STEMCELL Technologies	72304
Trans-ISRIB	Cayman Chemical	16258
TrypLE™ Express	Thermo Fisher Scientific	12604013
UltraPure™ Distilled Water	Thermo Fisher Scientific	10977035
Cloning		
Agar-Agar	Carl Roth GmbH + Co. KG	1347.2
BamHI	New England Biolabs	R3136S
BP/LR Clonase	Thermo Fisher Scientific	11789020/11791020
Carbenicillin Disodium Salt	AppliChem GmbH	A1491
DNA Ligation Kit, Mighty Mix	TaKaRa	6023
E-gel™ 1 Kb Plus DNA Ladder	Thermo Fisher Scientific	10488090
E-Gel™ EX Agarose Gels, 2%	Thermo Fisher Scientific	G402022
HiScribe® T7 ARCA mRNA Kit (with tailing)	New England Biolabs	E2060S
KAPA HiFi HotStart Ready Mix	Roche	KK2601
MinElute Gel Extraction Kit	Qiagen	28604
Monarch® Spin RNA Cleanup Kit (50 µg)	New England Biolabs	T2040S
One Shot™ Stbl3™ Chemically Competent E. coli	Thermo Fisher Scientific	C737303
P3 Primary Cell 4D-Nucleofector Kit L	Lonza	V4XP-3024
Polyethylenimine (PolyScience)	PolyScience	24765
QIAquick Gel Extraction Kit	Qiagen	28706
Quick CIP	New England Biolabs	M0525S
rCutSmart™ buffer	New England Biolabs	B6004S
S.O.C. Medium	Thermo Fisher Scientific	15544034
TE buffer	Biozol Diagnostics	BBA-D0123-450
Microfabrication		
ATFB-NHS	Iris Biotech	RL-2045
Epoxy resin (Resin L + Hardener L)	R&G Faserverbundwerkstoffe GmbH	1001151
HEPES	Sigma-Aldrich/Merck	83264
PAAm	Sigma-Aldrich/Merck	283215
PDMS (SYLGARD® 184)	Dow	25100445
PFOCTS	Sigma-Aldrich/Merck	448931
Potassium carbonate	Sigma-Aldrich/Merck	791776
PVP	Sigma-Aldrich/Merck	437190
Resin IP-S	Nanoscribe GmbH & Co. KG	N/A
TI Prime	MicroChemicals GmbH	100p001
Transparency film (Office Tree)	iLP GmbH	14441782

Immunocytochemistry		
Donkey serum	Sigma-Aldrich/Merck	S30-100ML
Paraformaldehyde solution, 4% in PBS	Thermo Fisher Scientific	J19943-K2
ProLong™ Diamond Antifade Mountant	Thermo Fisher Scientific	P36961
Triton X-100	Sigma-Aldrich/Merck	T9284

Table 2.2: Cell lines

Cell line	**Supplier**	**Order No.**
EMX1	Harvard Medical School	N/A
fChRimson-iNGN	Busskamp lab	N/A
HEK293T	ATCC	CRL-3216
iNGN	Harvard Medical School	N/A
Rat primary astrocytes	Thermo Fisher Scientific	51-0086

Table 2.3: Antibodies and dyes

Antibody/ dye	**Supplier**	**Order No.**
Anti-chicken IgY-Alexa Fluor 488	Thermo Fisher Scientific	A11039
Anti-GFP	Thermo Fisher Scientific	A10262
Anti-βIII-tubulin, eFluor™ 570	Thermo Fisher Scientific	41-4510-80
Hoechst stain	Thermo Fisher Scientific	H3570

Table 2.4: Plasmids

Plasmid	**Supplier**
EMX1 open reading frame	Gen9
pCAG-Cre:GFP	Addgene #13776
pCMV-Transposase	System Biosciences
pLIX_403	Addgene #41395
pMD2G	Addgene #12259
psPAX2	Addgene #12260
VI-6_pPiggyBAC-eDIO-mem-tdTomato	Busskamp lab

Table 2.5: Primers

Primer	**Sequence**
T7-Cre-for	5’-GCTAATACGACTCACTATAGGGACAGGCCACCATGGCCAATTTACTGA-3’
T7-Cre-rev	5’-TCATTACGGTCCATCGCCATCTTCCAGCAGGCGCACCATT-3’

td-for-BamHI	5’-GAATTCGGATCCGCCACCATGGTGAGCAAGGGCGAGGAG-3’
td-rev-BamHI	5’-GAATTCGGATCCTCATTACTTGTACAGCTCGTCCATGCC-3’

Table 2.6: Equipment

Device	**Manufacturer**
10x objective (Plan N 10x/0.25)	Olympus
20x objective BZ-PF20LP	Keyence
4D-Nucleofector® with X-unit	Lonza
Axon™ Digidata® 1550B	Molecular Devices
BD FACSAria™ Fusion Flow Cytometer	BD Biosciences
BZ-X810	Keyence
Countess™ II FL Automated Cell Counter	Thermo Fisher Scientific
EVOS XL Core Imaging System	Thermo Fisher Scientific
Glass pipettes VESbl-12-0-0-55	BioMedical Instruments
HD-MEA MaxOne	MaxWell Biosystems
LED light source (pE-300 ultra)	CoolLED
LED light source (pE-800)	CoolLED
MEA chips 60MEA200/30iR-Ti	Multi Channel Systems
MEA2100 system	Multi Channel Systems
MEA2100-Lite system	Multi Channel Systems
Microinjector (IM-11-2)	Narishige
Micromanipulator (MP-225)	Sutter Instruments
NanoDrop One Spectrophotometer	Thermo Fisher Scientific
Nanoscribe GT	Nanoscribe GmbH & Co. KG
Nanoscribe QuantumX	Nanoscribe GmbH & Co. KG
Plasma device Femto 1A	Diener electronic
ProFlex PCR System	Thermo Fisher Scientific
Revolve microscope	Echo
SciCam Pro CCD camera	Scientifica
Stage top incubator INU-KIW-F1	Tokai Hit
ThawSTAR CFT2 Automated Thawing System	Biolife Solutions
Transport incubator CellTrans 2018	Labotect
Transport incubator CellTrans 4016	Labotect
Upright microscope (SliceScope)	Scientifica

Table 2.7: Software

Software	**Developer**	**Version**
Autodesk Inventor Professional	Autodesk Inc.	2023
Clampex (pCLAMP™)	Molecular Devices	11.1.
Elephant python package	Denker et al., 2018	1.1.0
GraphPad Prism	GraphPad Software	10.4.1
ImageJ/Fiji	Schindelin et al., 2012	1.54f

Ironclust	Jun et al., 2020	5.9.8
MATLAB	The MathWorks, Inc.	2023b
Matplotlib	Hunter, 2007	3.6.0
MaxLab Live	MaxWell Biosystems	2021 release
MC_DataTool software	Multi Channel Systems	2.6.15
MC_Rack	Multi Channel Systems	4.6.2
NeuroExplorer 5	Nex Technologies	5.303
NumPy	Harris et al., 2020	1.22.4
OCULAR	QImaging	2.0.1.496
pandas	McKinney, 2010, The pandas development team, 2020	1.5.0
Probeinterface	Garcia et al., 2022b	0.2.24
Python	Python Software Foundation	3.9.12
SciPy	Virtanen et al., 2020	1.12.0
seaborn	Waskom, 2021	0.12.0
SpikeInterface	Buccino et al., 2020	0.101.0
TCX-Control	Multi Channel Systems	1.3.4

2.2 Methods

2.2.1 Stem cell culture

HiPSCs were utilized to create iNGN cells, as described previously by Striebel et al. (2023). Differentiation of these cells into post-mitotic, bipolar neurons was achieved by overexpressing Neurogenin-1 and Neurogenin-2 under a doxycycline (Dox)-inducible inducible promoter system (Busskamp et al., 2014). The iNGN cells were subsequently cultured and then reseeded onto MEAs in accordance with a previously described protocol (Schmieder et al., 2022). Initially, the iNGN cells were thawed and cultured on Matrigel-coated plates using mTeSR medium. The medium was prepared by adding mTeSR 5 × Supplement and 1 % penicillin-streptomycin (P/S) to mTeSR1 Basal Medium. The medium (1 ml per one well in a 6-well plate) was exchanged completely every day with triple the amount being added over the weekend. Passaging was done by aspirating the supernatant, washing once with DPBS+/+, adding TrypLE Express for 3 min, collecting cells in DPBS+/+ and centrifuging at 359 g for 4 min. Cell pellet was resuspended in mTeSR with Rho-associated, coiled-coil containing protein kinase (ROCK) inhibitor (3 µg/ml) or a cocktail of chroman 1, emricasan, polyamines, and trans-ISRIB (CEPT) (final concentrations: trans-ISRIB, 0.7 µM; chroman 1, 50 nM; emricasan, 5 µM) (Chen et al., 2021) was added. Following at least two passages, cells were seeded onto Matrigel-

coated plates. To initiate differentiation, 0.5 µg/ml of Dox was added consecutively for at least 3 days. All cell cultures were regularly tested for mycoplasma contamination.

2.2.2 Astrocyte culture

Astrocytes were cultured as described previously by Striebel et al. (2023). Production of astrocyte-conditioned media started with cultivating rat primary astrocytes in cell culture flasks (T25 or T75). Astrocytes were first expanded in astrocyte medium (DMEM, N-2 Supplement, 10 % FBS, and 1 % P/S). For passaging, supernatant was collected, cells washed once with DPBS+/+ and 1 ml Accutase added for 5 min in a T25 flask. If necessary, flask was rocked in between for complete detachment. Cells were collected in old supernatant, centrifuged at 359 g for 4 min and cell pellet resuspended in warm astrocyte media. To reduce nonspecific adhesion and associated cell loss, plasticware was pre-wetted before cell handling. The medium was switched to complete BrainPhys medium upon reaching confluency. Following a minimum of three days of cultivation, the astrocyte-conditioned BrainPhys medium was collected on a weekly basis as needed for MEA media exchanges. Usually about half the volume was taken off the astrocyte cultures and was replaced with an equivalent volume of fresh complete BrainPhys medium.

2.2.3 Altered gravity experiments

Work from this section has been published already and methods described here can also be found in Striebel et al. (2023).

2.2.3.1 Preparation of neuronal networks on microelectrode arrays for microgravity experiments

To eliminate undifferentiated cells, cytosine β-D-arabinofuranoside hydrochloride (Ara-C, 5 µM final concentration) was added at two days post-induction (dpi) to the iNGN culture. In parallel, the MEA chips were treated with plasma (ambient air, 0.3 mbar, 50 W), incubated with 0.1 mg/ml poly-D-lysine (PDL) overnight at 37 °C and 95 % relative humidity (RH), washed thrice with sterile deionized water (10 min each), and dried in the

laminar flow hood. Sufficient laminin (0.05 mg/ml) was added to cover the whole MEA area and incubated overnight at 37 °C and 95 % RH.

At 3 dpi, the induced cells were reseeded onto the MEA chips. After washing and dissociating the neuronal networks by a 5 min Accutase treatment, they were collected in their old medium and centrifuged at 359 g for 4 min. Subsequently, the neurons were resuspended in complete BrainPhys medium and 100,000 cells in 1 ml medium were added to one coated MEA. The complete BrainPhys medium was prepared by combining BrainPhys Neuronal Medium with 1 % P/S, 2 % NeuroCult SM1 Neuronal Supplement, and 1 % N-2 Supplement. The medium was supplemented with 20 ng/ml recombinant human BDNF, 20 ng/ml recombinant human GDNF, and 200 nM ascorbic acid. Given the pure neuronal identity of the iNGN culture after Ara-C treatment, astrocyte-conditioned media was added to enhance long-term neuronal cultures. This was done by exchanging half of the media weekly with a 1:1 mix of fresh complete BrainPhys medium and astrocyte-conditioned complete BrainPhys medium. Custom-made lids made from Polydimethylsiloxan (PDMS) were used to fully seal the MEA chips (Blau et al., 2009), ensuring sterility while permitting gas exchange.

2.2.3.2 Experiment hardware for centrifuge and drop tower experiments

To maintain physiological conditions for cell samples during experimentation, the MEA system was placed inside a pressure chamber as described in Striebel et al. (2023). Using the MEA system's integrated heaters, samples were kept at 37 °C. The chamber ensures stable pressure. Before each experiment the chamber was flushed with 5 % CO_2 in synthetic air to ensure adequate pH levels in the culture media. The autonomous system was operated via a computer located outside the pressure chamber, which also recorded and stored the electrophysiological data as well as the environmental sensor data. See Supplementary Figure 1 for a schematic of the hardware with all relevant parts and a graph showing the stability of environmental parameters over time. All experiment hardware was designed and assembled by Maximilian Sturm (DLR, Cologne). Conceptualization and testing were contributed by the whole MIND Gravity collaboration including myself (Striebel et al., 2023).

2.2.3.3 Hypergravity experiments on the Short-Arm Human Centrifuge

The Short-Arm Human Centrifuge (SAHC) at DLR in Cologne was used to perform hypergravity experiments as described in Striebel et al. (2023). Briefly, samples were cultured in the Busskamp lab and transported to the SAHC using transport incubators (37 °C, 5 % CO_2) five days before the experiments started. To avoid mechanical disturbances during transport and experiments through flowing media, the space between the lid and MEA was filled up completely to prevent air pockets. For experiments, samples were brought to the SAHC integration area in the transport incubator and were directly incorporated into the experiment chamber. Heating plates maintained 37 °C, and the chamber was filled with synthetic air containing 5 % CO_2. The chamber was fixed on a swing-out platform of the SAHC to ensure the resulting force remaining perpendicular to the MEA chip surface. This minimizes shear forces on the cells. Functionality checks were performed remotely before starting the recordings. Recording was performed throughout all experiment phases: 10 min of baseline (1 *g*), 30 s of acceleration to 4 *g* or 6 *g*, 5 min of exposure to 4 *g* or 6 *g*, 30 s of deceleration to 1 *g*, 5 min baseline (1 *g*). Phase-contrast microscopy images were captured before and after each centrifuge run. Three consecutive days of experiments were performed with five samples (36–38 dpi) prepared from one batch of neurons. Five 4 *g* and six 6 *g* runs were conducted in total.

2.2.3.4 Microgravity experiments in the drop tower

Experiments in the drop tower facility were supported by the European Space Agency (ESA) Education Office as part of the Drop Your Thesis! program. Experiments were carried out as described in Striebel et al. (2023). Briefly, samples were brought to the drop tower facility at ZARM (Bremen) a week before the start of the experimentation week with the same procedures and equipment as for the centrifuge experiments (see section 2.2.3.3). Integration procedure of the samples into the experiment chamber was also identical. For drop experiments, system functionality was confirmed, the drop capsule containing the experiment chamber with all support electronics lifted to the top of the tower, and the drop tube evacuated from air. This process took about 2 h. All systems were remotely activated and checked 15 min before the drop, after which data recording commenced. Following 10 min of baseline recording, the drop was executed. Recordings

continued for at least 10 min post-drop. Phase-contrast microscopy images were captured before and after each drop. Five drops were carried out on consecutive days with five different MEAs from three independent batches of neurons (46–55 dpi).

2.2.3.5 Data analysis of altered gravity experiments

After recording the data on a MEA2100 system, the MC_DataTool software was used to convert the data into the RAW binary file format. It was analyzed as described previously in Striebel et al. (2023). Spike sorting was applied to separate the activity of distinct units from the raw extracellular data, because individual electrodes can record signals from multiple neurons. Preprocessing, sorting, and automatic curation of data was done using the SpikeInterface python package (Buccino et al., 2020). The preprocessing step included a second-order Butterworth high-pass filter (cutoff 100 Hz) and common median referencing (Rolston et al., 2009). The Ironclust spike sorting algorithm was run with default parameters and a detection threshold of 4.5 (Jun et al., 2020). Auto-curation of data selected all units with a signal-to-noise ratio greater than five and an interspike interval (ISI) violation rate above 0.2 for further analysis. Mean firing and burst rates were calculated using NeuroExplorer 5. Bursting, characterized as short bursts of spikes with high internal frequency separated by longer periods of silence, was detected using an interval-based algorithm in NeuroExplorer 5. The following burst detection parameters, previously described by Yang et al., were used: a maximum inter-spike interval of 20 ms to initiate a burst, a maximum inter-spike interval of 100 ms to terminate a burst, a minimum inter-burst interval of 100 ms, a minimum burst duration of 20 ms, and at least two spikes per burst (Yang et al., 2018).

For further analysis, the experiments were divided in different phases. Hypergravity (centrifuge) experiments were examined during seven phases: Baseline (10 min), Ramp Up (~30 s), Hypergravity 1 (1 min), Hypergravity 2 (1 min), Ramp Down (~30 s), Post-Baseline 1 (1 min), and Post-Baseline 2 (1 min). To check for potential adaption processes, the first and last minute of the hypergravity phase (5 min total) and the post-baseline phase (5 min total) were analyzed separately. For drop tower experiments, data were extracted across four phases for five separate drops: Baseline (600 s), Microgravity (4.7 s), Impact (5 s), and Baseline (600 s). To ensure clean separation of experimental

phases, a safety margin was applied at the beginning and end of each phase before extracting firing and bursting rates (centrifuge experiments: 2 s, drop tower experiments: 150 ms). See Figure 3-1 and Figure 3-2 for a scheme on the experiment phases. Since firing and bursting rates typically follow a lognormal distribution, the logarithm of the values was used for statistical analysis (Buzsáki and Mizuseki, 2014). Units that exhibited no activity in any of the phases were excluded from analysis to avoid incorporating artifacts. The centrifuge experiment analysis included 144 and 44 units for firing and bursting rates, respectively, while the drop tower experiments included 63 and 19 units, respectively. Statistical analyses and visualizations were performed using GraphPad Prism. For comparison of experimental conditions, a repeated measures one-way ANOVA with the Geisser–Greenhouse correction and Tukey's multiple comparisons test was performed. A custom python script was used to prepare density plots of firing rate distributions.

To evaluate alterations in AP waveforms across experimental conditions, AP amplitude and half-width were extracted from waveform templates generated with SpikeInterface using the Ironclust sorting algorithm. Data from all curated units were then exported to Prism, outliers were detected and removed with the ROUT method (Q = 1 %). The remaining measurements were compared using a non-parametric ANOVA (Friedman test).

2.2.4 Long-term experiments on high-density microelectrode arrays

Work from this section has been published already and methods described here can also be found in Habibey et al. (2022b).

2.2.4.1 Culture of neuronal networks on high-density microelectrode arrays

The protocol was described previously by Habibey et al. (2022a) and was modified from the original seeding protocol for low-density MEAs (Habibey et al., 2022c) to the usage of HD-MEAs. First, iNGN-EGFP cells were cultured and differentiated as described in section 2.2.1. The cells were induced for four days, and Ara-C was added at 3 dpi for 24 h to select for exclusively postmitotic neurons in the culture.

To coat HD-MEA chips with PDL and laminin as suited for long-term neuronal cultures, the sterile HD-MEA chips were plasma-treated for 2 min (ambient air, 0.3 mbar, 50 W) to increase hydrophilicity. 50 µl of a 0.1 mg/ml PDL solution was applied to cover the sensor area and surrounding regions inside the chip. The solution was incubated for 24 h at 37 °C and 95 % RH, then washed three times with ultrapure water and dried under laminar flow in a cell culture bench. Subsequently, 50 µl of laminin (0.05 mg/ml) was given on the sensor area and incubated for 3 h prior to reseeding. As described in section 2.2.3.1, the differentiated iNGN-EGFP neurons were dissociated with Accutase, subjected to centrifugation (359 g, 4 min) and resuspended in complete BrainPhys medium. Approximately 30,000 cells were subsequently seeded onto the sensor area. To provide support for neurons through astrocyte-secreted factors, astrocyte-conditioned BrainPhys medium was prepared as described in section 2.2.2. Subsequently, a 1:3 mix of the astrocyte-conditioned to fresh complete BrainPhys medium was used to replace half of the medium in HD-MEAs once a week. Lids for the MEA chips were used as described previously to maintain sterility while permitting gas exchange (Blau et al., 2009).

2.2.4.2 Microscopy and electrophysiology experiments of high-density microelectrode arrays

Fluorescence imaging of each culture was performed at multiple time points using an upright fluorescence microscope. During imaging, cultures rested on a stage top incubator. The pE-300ultra system provided excitation light. To capture the entire network area on the HD-MEA, forty overlapping images were recorded for each sample with a 10× objective using the OCULAR software. These tiles were subsequently merged using the Grid/Collection stitching plugin in ImageJ (Preibisch et al., 2009) to generate a full-field view of network morphology for each imaging day. Sequential images from three independent HD-MEA cultures were collected weekly between 22 and 76 dpi to depict progressive changes in network structure. Cell and cluster migration were analyzed with the Manual Tracking plugin in ImageJ. For each MEA, neurons or, if applicable, their joined clusters were individually tracked across the 2-month period. Displacement data from 904 neurons across three MEAs were exported as CSV files to quantify weekly and cumulative movement on the sensor surface.

MaxOne HD-MEA chips were used and contain 26,400 electrodes arranged in a 120 × 220 grid with a 17.5 µm pitch, covering a 3.85 × 2.10 mm² sensing area (Ballini et al., 2014; Müller et al., 2015). Recordings were carried out in a mini-incubator maintained at 37 °C. For every session, an Activity Scan in full-scan mode was first executed to identify firing electrodes and generate an activity map. Approximately 1,000 electrodes were sampled for 30 s at a time, and the scan advanced in 29 successive steps to cover the entire array. Electrodes showing > 0.1 Hz firing rate and average spike amplitudes above 20 µV were classified as active. The software produced a color-coded activity map of the whole sensor surface. Based on these scans, up to 1,024 of the most active electrodes were chosen for a Network Assay, which recorded simultaneous activity for 5 min. Each combined scan and network recording required roughly 45 min. Because each electrode was sampled for only 30 s, electrodes that were inactive during that window were not included in further analyses. Longitudinal recordings were obtained from three cultures over 11 consecutive weeks, spanning 22-90 dpi, to evaluate long-term changes in firing and burst dynamics. Six HD-MEA cultures were initiated, but only three maintained stable networks beyond three months; the remainder detached within the first three weeks and were excluded by 35 dpi.

To assess the roles of excitatory and inhibitory transmission, receptor antagonists were applied to two cultures at 118 and 120 dpi. Excitatory N-methyl-D-aspartic acid (NMDA) and α-amino-3-hydroxy-5-methyl-4-isoxazolepropionic acid (AMPA) synapses were blocked by adding (2R)-amino-5-phosphonovaleric acid (AP5, 50 µM) and 2,3-dioxo-6-nitro-7-sulfamoyl-benzo[f]quinoxaline (NBQX, 10 µM), respectively. Before drug addition, 500 µl of culture medium was removed and stored. Baseline activity was recorded with both the Activity Scan and Network Assay, followed by a 5 min incubation with NBQX + AP5 at 37 °C and repeat recordings. Cultures were then washed twice with warm BrainPhys medium, replenished with a 1:1 mix of fresh and saved medium, incubated for 30 min, and scanned again to assess recovery. The same procedure was used to examine inhibitory signaling: Gabazine (10 µM), a GABA_A receptor antagonist, was applied to the same cultures at 120 dpi, with recordings performed before, during, and after drug washout.

2.2.4.3 Data analysis of high-density microelectrode array recordings

To isolate single-neuron activity from the extracellular recordings, all electrode traces from the 5 min Network Assay were processed through a spike-sorting pipeline. Pre- and post-processing were performed with the SpikeInterface framework (Buccino et al., 2020) using the Kilosort3 algorithm (Pachitariu et al., 2023). Signals were first high-pass filtered with a second-order Butterworth filter at 100 Hz and referenced to the common mean. Sorting used default parameters except that the batch size was reduced to NT = 16,448 to avoid memory limitations. Automated curation then removed any units showing an ISI violation rate > 0.2, a signal-to-noise ratio < 5, or an average firing rate < 0.1 Hz.

Timestamps from the sorted units were analyzed in NeuroExplorer. Firing metrics: Overall AP frequency was computed as total spikes divided by the 5 min recording duration. Instantaneous firing rate was derived from the inverse of each ISI using the built-in instant frequency algorithm (Wang et al., 2016). For each recording day the mean instantaneous firing rate, the proportion of spikes occurring at high frequency, and the percentage of neurons exceeding a “fast-firing” threshold (> 150 Hz) were calculated; the remainder were classified as slow-firing (< 150 Hz). Burst detection: From the burst-detection methods available in NeuroExplorer the Poisson surprise algorithm, which detects bursts by quantifying how improbable a cluster of spikes is under the assumption of a Poisson process with the neuron’s baseline firing rate, performed best according to visual inspection. Parameters were set to a minimum surprise of 4, a burst duration ≥ 20 ms, and at least four spikes per burst (Habibey et al., 2015b). The surprise score S is given by

$$S = -\log P,$$

$$\text{where } P = e^{-\lambda T} \sum_{n=N}^{\infty} \frac{(\lambda T)^n}{n!},$$

λ the mean firing rate, N the number of spikes, and T the burst window. NeuroExplorer identifies a burst when three consecutive APs have ISIs shorter than half the neuron’s average ISI, adds further spikes while this condition holds, and retains the burst length that maximizes surprise (Cotterill and Eglen, 2019; Legendy and Salcman, 1985). Extracted features included burst frequency, mean burst duration, and the percentage of total APs occurring within bursts (Habibey et al., 2017; Wilk et al., 2016).

Active neurons were defined as units firing > 0.1 Hz. Across all recording days, the number of sorted neurons ranged from 1,065 (22 dpi) to 3,076 (69 dpi). Group comparisons of AP frequency, instantaneous rate, burst parameters, and neuronal movement across culture ages were performed with a Kruskal–Wallis test followed by Dunn's post-hoc multiple-comparison test. The same statistical approach was used to compare baseline, drug, and washout conditions for NBQX + AP5 or gabazine treatments at 118 and 120 dpi. Results are reported as mean ± SEM, with $p < 0.05$ considered significant.

2.2.5 *In vitro* plasticity and learning experiments

A microfluidic structure (Figure 2-1) was prepared as described (see sections 2.2.6.2 and 2.2.6.3) (Striebel et al., 2025b, 2025a). The design consisted of three rows (layers) of microwells, all located in alignment with a column of electrodes. The first and the last layer had six wells, while the middle layer had eight. Between the layers there were two reservoirs, closed from the top with the same height as connecting channels, but laterally spanning the whole width of the array. All microwells are connected through microchannels along the electrode columns to the reservoirs. A narrowing in channel width when entering the reservoirs was included to reduce the chance of backwards growth of axons. Lateral barrier-like structures were included to funnel axons sidewards for increased lateral connections and mixing. This geometry is inspired by FNNs. iNGN-EGFP cells were prepared as described previously (see section 2.2.1 and 2.2.6.4) and reseeded on top of the microfluidic devices by adding cells in bulk so that about ten neurons were left in each microwell. Four MEAs were prepared and continuously stimulated and recorded using the MEA2100-Lite system on following dpi: 15, 16, 20, 21, 23, 27, 30, 31, 32, 34, 35, 37, 38, 41, 42, 48 (test stimulation only), 49, and 56. After this training period, we monitored the cultures further by recording baseline (unstimulated) activity and applied

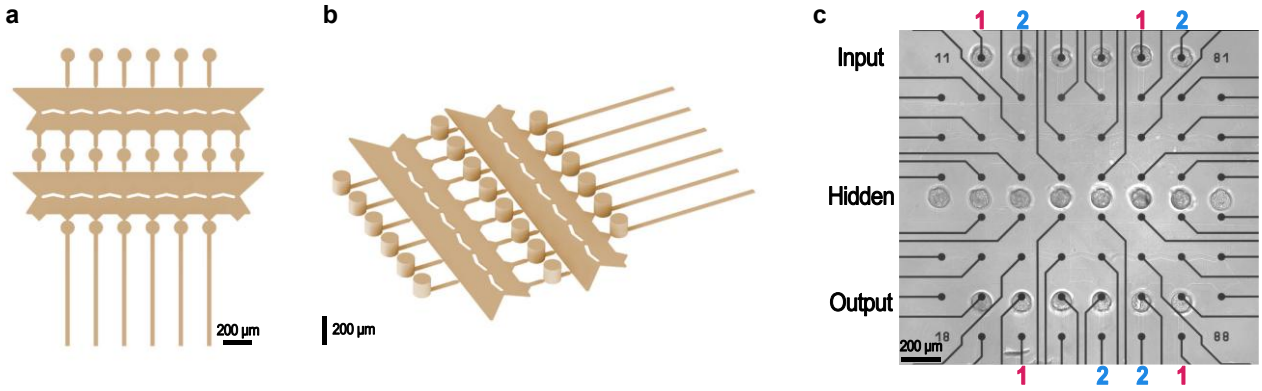

Figure 2-1: Microfluidics and network for *in vitro* learning experiments. a,b, Microfluidic scaffold for network formation on MEAs. Top (**a**) and side (**b**) view. **c**, Brightfield image of a microscaffold on a MEA with iNGN neuronal populations seeded in the round microwells. There are three layers of neuronal populations in the network (input, hidden and output layer). Two stimulation patterns were used for training and respective populations marked in the input and output layers: pattern 1 (red) and pattern 2 (blue).

test stimulation only (without training) on the following dpi: 57, 59, 62, 64, 66, 68, 71, and 74. Live cell imaging of the samples using the BZ-X810 microscope was done on dpi: 6, 14, 20, 31, 35, 43, 49, 57, 63, and 72. The aim of the experiment was to see if the samples could be trained to associate a certain combination of electrodes in the input and output layers (pattern 1 and 2) with each other by repeatedly stimulating these patterns synchronously. Thus, two electrodes of the defined input and output layers were assigned to pattern 1 and 2 each (Figure 2-1). During training phases, the stimulation of the output layer came 10 ms after the stimulation of the input layer electrodes. This was intended to induce a directionality in the association patterns and to account for transmission delays in the network from input to output layer. The pulses consisted of trains of biphasic current pulses (100 µs of -30 µA followed by 100 µs of 30 µA). A tetanic stimulus (Chiappalone et al., 2008; Jimbo et al., 1999) was applied up to 32 dpi after which theta burst stimulation (TBS) (Chen et al., 2023) was applied for the remainder of the experiment, since this was shown to better induce LTP. Tetanic stimulus trains consisted of 10 pulses with an interpulse interval of 50 ms. Pulse trains were repeated every 4.5 s for 20 min. TBS trains consisted of 4 pulses with an interpulse interval of 20 ms. Pulse trains were repeated every 200 ms for 20 min. To test the reaction of the network to the training, only electrodes in the input layer were stimulated by repeating single test pulses every second for 2 min. Usually, training and test sessions were combined and baseline activity was measured in the beginning and end of each session in the following order: 1. Baseline before, 2. Test

stimulus pattern 1 and 2, 3. Training of pattern 1 and 2, 4. Test stimulus pattern 1 and 2, 5. Baseline after. The order of the different patterns during test and training sessions were altered during the experiment to avoid the induction of possible artifacts induced through the same order.

Analysis of the data was done in collaboration with Dr. Christoph Miehl. First, all recorded data was sorted using the SpikeInterface python package together with the Ironclust algorithm as described previously (section 2.2.3.5). Further analysis was done using a custom-developed python script. The analysis was focused primarily on correlation of the activity using the Pearson correlation coefficient (CC) and PR as described previously (see section 2.2.6.7).

2.2.6 Single-Neuron Network Assembly Platform

Work from this section has been published already and methods described here can also be found in Striebel et al. (2025b, 2025a).

2.2.6.1 EMX1 cell line and genetic modification

The EMX1 cell line was prepared and kindly provided by Alex H. M. Ng, PhD, at Harvard University. Briefly, the cell line was prepared by cloning the EMX1 open reading frame into the pLIX_403 backbone using the BP/LR Clonase following manufacturer protocols. This backbone is a doxycycline-inducible and puromycin-selectable lentiviral backbone. Production of lentiviral particles was done by co-transfecting pLIX_403+EMX1, pMD2G and psPAX2 into HEK293T cells using polyethylenimine as previously described (Ng et al., 2021). The cell line was then produced by transducing iNGN cells with pLIX_403+EMX1 lentiviral particles. Puromycin selection was done for 48 h post-transduction (3 µg/ml). For live cell microcopy the EMX1 cell line was modified to constitutively express tdTomato. To create a plasmid for constitutive expression of tdTomato in the EMX1 cell line, the double-floxed inverse open reading frame under the EF1α promoter (eDIO) system from plasmid VI-6_pPiggyBAC-eDIO-mem-tdTomato had to be excluded and the direction of tdTomato flipped. Thus, the tdTomato gene was amplified via polymerase chain reaction (PCR) using the primers td-for-BamHI and td-rev-

BamHI. For PCR, 30 ng of template were mixed with 1 µl of each primer and filled up to 50 µl with ultrapure water. After adding 50 µl of KAPA HiFi HotStart Ready Mix, the solution was split into two PCR tubes to reduce the chance of point mutations being introduced. PCR was done according to manufacturer's protocol with 35 s elongation time. PCR product was pooled, 100 µl ultrapure water added and put on 10 lanes of a 2 % E-Gel EX. The PCR band was cut from the gel and gel extraction performed with the MinElute Gel Extraction Kit according to manufacturer's protocol. The backbone was then digested and treated with calf intestinal phosphatase (CIP) to avoid self-ligation to allow insertion of the tdTomato sequence. Digest was done by mixing 5 µg of DNA, 5 µl rCutSmart buffer, 4 µl BamHI and adjusting to 50 µl with ultrapure water according to manufacturer's protocol. Clean up of reaction with QIAquick Gel Extraction Kit followed by Quick CIP was done according to manufacturer's protocols. A 2 % E-Gel EX was run and the uppermost band cut to get the vector backbone. QIAquick Gel Extraction was performed. Ligation was performed by mixing 5.7 µl vector, 2.9 µl insert and 2.1 µl TE-buffer with 10 µl DNA Ligation Mix and after which the mixture was incubated at 16 °C overnight. A negative control was prepared by replacing the insert with TE-buffer. Plasmid and control were transformed into One Shot Stbl3 Chemically Competent *E. coli* via heat shock (42 °C, 45 s) and incubated on LB Agar plates with carbenicillin (100 µg/ml). Colony PCR was performed to verify correct insertion and rule out self-ligation, since the number of colonies in the negative control (no insert) was similar to the vector with insert. Sanger sequencing was used to confirm correct integration and orientation of the insert. EMX1 cells were then nucleofected with the construct using a Lonza 4D X-unit with the P3 Primary Cell 4D-Nucleofector Kit L and the pulse CB-156 following the manufacturers protocol as described previously (Kutsche et al., 2018; Sauter et al., 2019). Cells were then plated on Matrigel-coated plates in mTeSR with ROCK inhibitor overnight. The next day fresh mTeSR with blasticidin (20 µg/ml) was added. Fully selected cells were expanded and frozen. Fluorescence activated cell sorting (FACS) by the Flow Cytometry Core Facility of the Universtiy Hospital Bonn left us with a cell population expressing high levels of tdTomato that did not lose the fluorescence over time.

2.2.6.2 Microfluidics manufacturing

Designs of the microfluidic structures were created (Figure 2-2a) as a negative form in Autodesk Inventor Professional 2023 (Figure 2-2b). Identical structures were placed next to each other and aligned to the electrode layout so that several identical circuits can be cultured and measured simultaneously on one MEA. Custom designs were used except for the stomach-shaped part of the directional structure which was adapted from previous studies (Forró et al., 2018; Girardin et al., 2022) (Figure 2-2c). Dimensions of the microfluidics were as follows: cylinder-shaped microwells had a diameter and height of 100 µm; to avoid cell somata from migrating from the wells into channels (Taylor et al., 2005), microchannels were 5 µm high; and the width of the microchannels was 20 µm (Y-shape) or 30 µm (directional structures). The designs were then manufactured by our collaborators Dr. Helge Gehring and Daniel Wendland in the group of Prof. Dr. Wolfram Pernice at the Münster Nanofabrication Facility. Direct laser writing (DLW) was employed to fabricate the microfluidic scaffolds. This three-dimensional lithography technique relies on two-photon polymerization and enables printing of features down to the nanometer scale. Microfluidic patterns were written on four-inch silicon wafers for a more efficient parallelized fabrication, while individual designs were produced on 25 × 25 mm² fused-silica substrates. Prior to writing, substrates were cleaned and coated with the adhesion promoter TI Prime by spin-coating, followed by application of IP-S photoresist. Structures were written layer-by-layer using Nanoscribe GT and QuantumX align systems, with a lateral hatch spacing of 0.3 µm and a vertical slice spacing of 0.2 µm. Using a 25× objective, structures were printed in cubic sections of 250 µm edge length to maintain print quality. After exposure, the prints were developed in propylene glycol methyl ether acetate (PGMEA), rinsed with isopropanol, and dried under a nitrogen stream.

For manufacturing of microfluidics, following materials and processes were used:

- PDMS was prepared by mixing base and curing agent 10:1 by weight, stirred thoroughly, transferred to a centrifuge tube, and centrifuged for 2 min at 3234 g to degas and get rid of all bubbles. After casting PDMS it was important to degas the liquid PDMS on the mold in a vacuum chamber until most bubbles were gone or at least until none are attached to the surface of the mold. Curing can either be done

at room temperature (RT) for 24 h or at 80 °C for 2 h with higher temperatures causing the PDMS to shrink more in the process (Lee and Lee, 2008).

- Epoxy resin was prepared by mixing base and hardener 100:40 by weight, stirred thoroughly, transferred to a centrifuge tube, and centrifuged for 2 min at 3234 g to degas and get rid of all bubbles. After casting the liquid epoxy, it was cautiously degassed in a vacuum chamber without applying a strong (> -0.95 kPa) vacuum since boiling could occur and influence the material negatively. Curing at RT for 48 h or at 60 °C for 5 h is possible. When molding epoxy from a PDMS template, curing at 60 °C is avoided since the PDMS template was turning milkier with every mold prepared. After 2-3 molding procedres, the possibility that the PDMS bonds to the epoxy is very high.
- Trichloro(1H,1H,2H,2H-perfluorooctyl)silane (PFOCTS) was used to silanize molds to prevent sticking of material to the surface and to facilitate peel off. A few drops of PFOCTS were added to the bottom of a desiccator, to-be-silanized samples were placed on a tray over them. After reducing the pressure to -80 kPa with a pump, the valve of the desiccator was closed and left for 60 min. Samples were subsequently baked at 90 °C for 15 min to enhance the silane layer and evaporate excess material.

Preparation of master molds for subsequent production of microfluidic devices used in cell culture was as follows (Figure 2-2a): First, the 3D-printed structure was silanized as described above. Then PDMS was prepared and poured on the structures in a thick (~5 mm) layer. PDMS was cured at RT and subsequently silanized. Epoxy was prepared and cast on the PDMS. Epoxy was left at RT until the next day. PDMS was then peeled off the still soft epoxy and the epoxy was fully cured at 60 °C for 5 h to avoid PDMS turning milky. Epoxy was silanized and cast with PDMS. PDMS was cured at RT to avoid shrinkage and silanized. From the PDMS negative the single structures which should be fabricated into microfluidics were cut. A glass substrate (mirror tile or microscopy slide) was cleaned with ethanol. Epoxy was cast on top of the structures in the small piece of PDMS, degassed in vacuum, and put on the glass. Pressing gently on the back of the PDMS removed small air bubbles from the liquid epoxy and avoided a thick layer of epoxy being left on the glass. It was left for curing at RT overnight. After taking off the PDMS, epoxy edges and excess material was removed and cured completely at 60 °C. A small

frame with an opening of a few mm was cut from transparency film with a thickness of 100 µm and glued around the epoxy structures atop the glass. These glass substrates with epoxy structures and frame were then silanized before use in fabricating microfluidics for cell culture. Typically, microscaffolds from PDMS intended for coupling with MEAs are produced with a thickness of around 100 µm. Smaller aspect ratios decrease the risk of damage in the fabrication process, increasing reliability and thinner PDMS devices are more flexible and attach better to the MEA surface. The designs can be manufactured and faithfully replicated throughout the fabrication process, including the microscaffold level (Figure 2-2d-f).

To prepare microfluidics from the templates, PDMS was prepared and poured on the template. Degassing in the vacuum is important to avoid bubbles from destroying the microfluidics. A piece of transparency film was placed on top of the liquid PDMS. On top of the transparency film, a thin layer (~2 mm) of cured PDMS and under a piece of glass was placed. Both, transparency film and PDMS-glass sandwich, covered the whole template and rested on the frame of transparency film around the structures to avoid them from being destroyed. With a clamp, the glass was pressed onto the template, causing excess liquid PDMS to flow out of the opening in the transparency film frame. PDMS was cured at 60 °C for 30 min or until fully hardened. After taking off the clamp, PDMS-glass sandwich and top transparency film, the microfluidic device can be gently taken out of the template. The process was repeated. After manufacturing, it was checked under the microscope if microwells are open from the top or if a thin layer of PDMS is still covering them. If closed, most of the times rubbing over them with a tweezer removed the thin PDMS layer and opened them up.

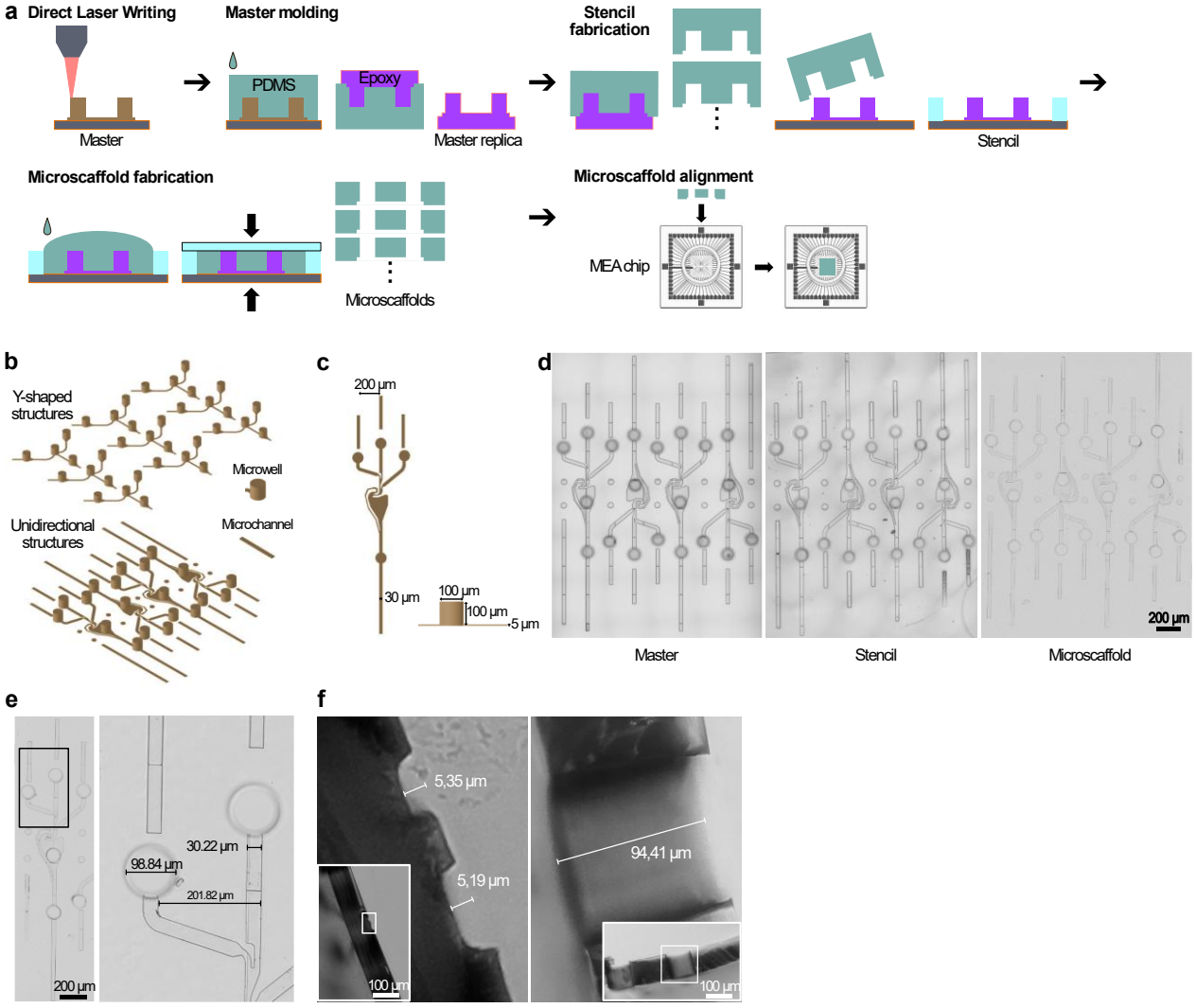

Figure 2-2: Microfluidics manufacturing and design. a, Microfluidic master molds were generated by direct laser writing (DLW), replicated in epoxy via soft lithography, and used to reproduce structures on glass substrates. After molding microfluidic devices in PDMS, they were aligned on MEA electrodes before single neuron placement. **b,** Y-shaped and linear (unidirectional) scaffold designs arranged in arrays to fit multiple structures on one MEA. **c,** Dimensions of microwells and microchannels used in the designs. **d,** Microscopy images of a representative DLW master, epoxy stencil, and PDMS scaffold. **e, f,** Size validation of a representative scaffold demonstrating accurate reproduction of the original design. Top view (**e**) and cross section (**f**). *Figure is part of a submission currently in press (publication will be covered under a CC-BY 4.0 license) (Striebel et al., 2025b). Original data and visualization generated by the author. The submission is based on a preprint (Striebel et al., 2025a) and involves the same co-authors. Partly created in BioRender. Kunze, S. (2025) https://BioRender.com/rxqdqiu*

The whole fabrication process has potential for parallelization and speeding up the manufacturing. For example, many PDMS negatives can be fabricated from the epoxy master replicas which can be used to fabricate many molds for microscaffold fabrication. Due to the quick fabrication process of the microscaffolds from the molds, this step also

offers the opportunity for parallelization. This way, large amounts of microscaffolds can be produced in a short period of time using this approach.

2.2.6.3 Anti-fouling surface coating

To prevent cells from attaching and growing outside and atop of the microfluidics, a previously described protocol for rendering the PDMS surface anti-fouling was used (Girardin et al., 2022; Weydert et al., 2019). In brief, 13 mg of poly(allylamine hydrochloride) (PAAm) and 31.8 mg of potassium carbonate were dissolved in 2.6 ml of ultrapure water. The solution was heated to boiling for improved dissolution and cooled rapidly. Then 11.2 mg of N-Succinimidyl 4-azido-2,3,5,6-tetrafluorobenzoate (ATFB-NHS) was dissolved in 4.135 ml of pure ethanol (EtOH). ATFB-NHS has to be protected from light. After brief ultrasonication (~10 s) the solution was gradually added to the PAAm solution under continuous stirring with a magnetic stirrer. Stirring for at least 3 h lead to a clear solution. In case of precipitation, solution was discarded, and the process repeated. The PAAm-ATFB solution was then diluted to 0.1 mg/ml in a 2:3 mixture of HEPES/EtOH (10 mM of N-(2-Hydroxyethyl)piperazine-N′-(2-ethanesulfonic acid) (HEPES) in ultrapure water and pure ethanol) for further use.

Functionalization of PDMS microscaffolds: PDMS structures were first plasma-treated in ambient air (18 W, 2 min) to activate the surface. Immediately afterward, a PAAm–ATFB solution was applied across the entire microfluidic area and allowed to react at RT for 30 min in the dark. The scaffolds were then rinsed with HEPES/EtOH and ultrapure water. Next, a 10 mg/ml polyvinylpyrrolidone (PVP) solution in EtOH was spread over the PDMS, excess liquid removed, and the surface gently dried with compressed air. For cross-linking, the coated devices were exposed to ultraviolet (UV) light in a sterile culture hood for 5 min. PDMS was immersed in methanol for 1 h with fresh methanol replacements every 15 min, followed by a 5 min ultrasonication step in new methanol to eliminate residual coating agents. Finally, the microfluidics were rinsed with ultrapure water and stored at 4 °C in ultrapure water until use.

2.2.6.4 Single-cell seeding in SNAP

To create defined neuronal circuits with single-cell precision (Figure 2-3a), MEA chips or cover slips were treated with plasma, incubated with PDL, and washed (see section 2.2.3.1). The microfluidic devices with anti-fouling coating were then placed onto the substrate with a drop of ultrapure water. With a tweezer the microscaffold was aligned to the microelectrodes under a cell culture microscope in a laminar flow hood and left for drying in the hood. To get rid of all water on the surface and increase attachment of the microfluidics to the surface, the MEAs were put in a vacuum to evaporate excess solution for at least 20 min. Then a 3 mm wide frame was cut from a layer of cured PDMS (about 3 mm thick) with a 1 x 1 cm^2 rectangle open in the center. This frame was placed around the microfluidics acting as a barrier separating the microfluidics from the surrounding area in the MEA. After drying, ultrapure water was added to the MEAs and a short pulse of vacuum applied, so that microchannels were evacuated of air and filled with water. Subsequently water was exchanged with laminin solution and incubated (see section 2.2.3.1).

Rat primary astrocytes were reseeded onto the microfluidics as described previously (see section 2.2.2). After detachment, centrifugation and resuspension of astrocytes, 30,000 cells in 70 µl astrocyte media were seeded on top of the microfluidics inside the PDMS border and left for attachment in the incubator for 1 h. The MEAs were then filled with astrocyte media and cultured until single-cell seeding, usually the day after.

HiPSC-derived neurons at 5-6 dpi were dissociated with Accutase, centrifuged down (359 g, 4 min), and resuspended in 1 ml of complete BrainPhys medium, as described in section 2.2.3.1. To check for the influence of Ara-C on single cell survival, it was added to the differentiating neurons 24 h prior to reseeding or left out. For seeding the final SNAPs, it was left out. To increase the survival rate of single neurons, ROCK inhibitor Y-27632 or CEPT (Chen et al., 2021) was added to the complete BrainPhys during resuspension and for culturing.

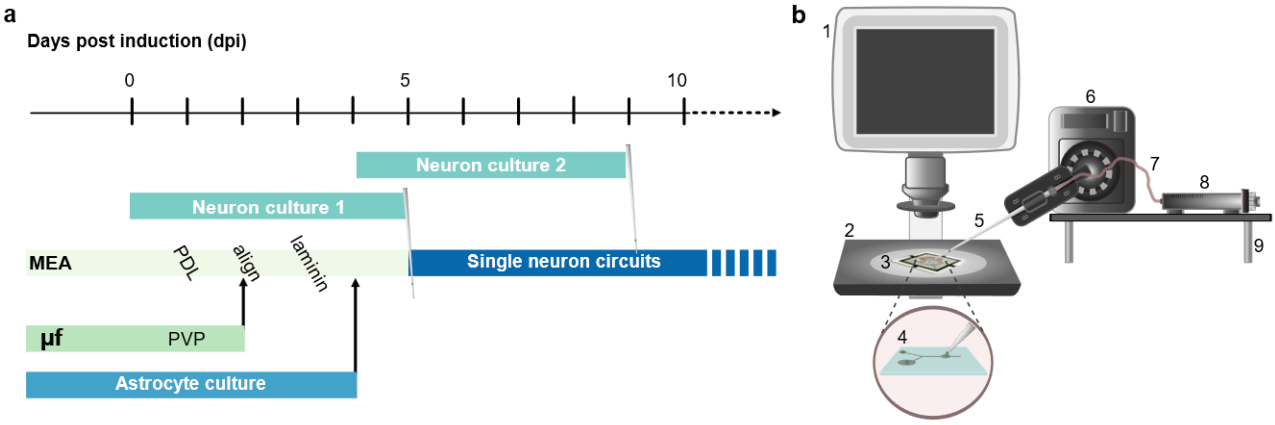

Figure 2-3: Preparation process of SNAP cultures. a, Schematic outline of the protocol for preparing isolated circuits with single-neuron resolution in the SNAP platform. Time points of individual cell placements are indicated by pipette symbols. Abbreviations: µf = microfluidics, MEA = microelectrode array, PVP = polyvinylpyrrolidone surface functionalization, PDL = poly-D-lysine coating. **b**, Experimental setup for targeted cell placement, operated within a sterile laminar flow hood. The system includes a microscope (1) and a stage (2) supporting the MEA device combined with microfluidics (3) during the cell seeding process (4). A fine glass micropipette (5) is operated via a micromanipulator (6), and connected by silicone tubing (7) to a manual microinjector (8). All components are mounted on a custom-designed adjustable platform (9). *Figure is part of a submission currently in press (publication will be covered under a CC-BY 4.0 license) (Striebel et al., 2025b). Original data and visualization generated by the author. The submission is based on a preprint (Striebel et al., 2025a) and involves the same co-authors.*

For single-cell placement, the astrocyte medium was first removed from the MEA and the surface rinsed once with DPBS+/+. BrainPhys medium was added inside the PDMS barrier and a small amount was also applied outside the barrier, ensuring the two media pools did not merge. Neurons in suspension were introduced into the outer region so the PDMS barrier prevented them from floating onto the microfluidic structures. Using a custom single-cell transfer setup (Figure 2-3b), individual neurons were picked up with a glass micropipette and deposited into individual microwells. The apparatus consisted of an EVOS XL Core imaging system and an adjustable platform equipped with a micromanipulator carrying a microinjector. Guided by the micromanipulator, the pipette tip was positioned over a neuron settled on the MEA surface. Gentle suction applied via the microinjector drew the cell into the pipette, with pressure finely adjusted to hold it in place. The pipette was then steered to a target microwell, and the neuron was released with slight positive pressure. Correct placement was confirmed by visual inspection before repeating the process until all wells contained a cell. Afterwards, medium outside the barrier was carefully aspirated, the area gently washed, and the MEA was lidded and

returned to the incubator. Once the neurons adhered, the inner chamber was filled with fresh BrainPhys supplemented as described above. Five days later, a second seeding round was performed to replace any microwells where the initial neuron had been lost, following the same procedure. Old culture medium was collected, leaving just enough to cover the inner chamber for the reseeding. After the new cells were deposited, the surrounding medium was aspirated and washed, and the MEA was again incubated to allow attachment. Finally, a 1:1 mixture of the saved medium and fresh complete BrainPhys with CEPT supplement was added. Using this method, four independent circuits on a single MEA could be seeded in about 20 min, with each individual placement taking only a few seconds.

For control experiments, neuronal populations were plated directly into the microfluidic devices on the same day of the first single-cell seeding. After removing the astrocyte medium and washing, 15,000 dissociated neurons in 70 µl of complete BrainPhys with CEPT were pipetted inside the PDMS barrier over the microfluidics. To ensure each microwell contained at least five neurons as confirmed visually, a second application of 15,000 neurons in 12 µl medium was performed. Following a brief incubation for cell attachment, the MEAs were topped up with complete BrainPhys containing CEPT.

The SNAP microstructures were seeded with three induced neuronal lines: iNGN-EGFP, EMX1-tdTomato, and iNGN-fChRimson. The first two lines constitutively express their fluorescent reporters EGFP and tdTomato, respectively. The iNGN-fChRimson line carries an eDIO construct encoding the fast ChRimson variant. In this arrangement, fChRimson expression is activated only after delivery of Cre recombinase, enabling temporal control so that optogene expression begins only after transcription factor-driven neuronal differentiation has been initiated (Klapper et al., 2017). Such delayed induction helps preserve stable transgene expression, which can otherwise diminish in stem cells, particularly for optogenetic constructs. Fast ChRimson is a rapid-kinetics version of the red-shifted channelrhodopsin ChRimson, with an excitation peak near 590 nm (Klapoetke et al., 2014; Mager et al., 2018). The fChRimson-EYFP sequence was kindly provided by Prof. Dr. Ernst Bamberg. To induce expression, Cre messenger RNA was generated using the HiScribe T7 ARCA mRNA Kit (with tailing) and purified with the Monarch Spin RNA Cleanup Kit (50 µg). Cre DNA was transcribed by PCR from the pCAG-Cre:GFP plasmid

(Matsuda and Cepko, 2007) with T7-Cre-for and T7-Cre-rev primers. At day 0 post-induction, cells were transfected with the Cre mRNA using Lipofectamine MessengerMAX according to the manufacturer's instructions, causing inversion of the eDIO cassette and initiation of fChRimson expression. All subsequent handling and seeding followed the same procedures described for the other lines.

When two different cell types were introduced into the same SNAP circuit, the procedure for the first cell type was carried out in full as described above. After all microwells designated for cell type 1 were seeded, the region around the PDMS barrier was rinsed as outlined and replenished with a small volume of medium. Single-cell seeding was then repeated for cell type 2, ensuring that all microwells assigned to this second population were filled in the same manner. This method can theoretically be expanded to include many cell types in the same SNAP circuit.

2.2.6.5 Electrophysiology experiments of SNAPs

MEA measurements were carried out on a MEA2100-Lite system, while imaging was performed on a Keyence BZ-X810 microscope with a 20× objective. Spontaneous activity was recorded for a minimum of 3 min, typically 5-10 min, at the following dpi (±1 day): Y-shaped circuits at 13, 22, 27, 33, 39, and 49 dpi; directional circuits at 14, 18, 21, 24, 27, 31, 33, 36, 49, 54, 61, 67, and 76 dpi. Cultures received weekly half-medium changes with fresh complete BrainPhys medium (without CEPT).

Electrical stimulation was controlled via MC_Rack software. After baseline activity was captured, directional circuits received trains of 30 biphasic pulses (−15 µA for 100 µs followed by +15 µA for 100 µs) delivered to the left and right microchannels at 1.8 s intervals while recordings continued. For optogenetic activation of iNGN-fChRimson neurons, the MEA headstage was placed beneath an upright microscope with a 10× objective and illuminated by an LED light source (pE-800). Stimulation protocols, created in Clampex and synchronized with MEA recordings in MC_Rack, were applied through the sterile MEA lid. Two irradiance levels, 23 µW/mm² and 46 µW/mm², were used. These low irradiances were chosen to minimize phototoxicity and avoid electrode artifacts. The 2 mm light spot was centered over the electrode array. Each protocol

consisted of trains of 50 ms light pulses delivered at 0.5, 1, 2, and 5 Hz, followed by 100 ms pulses at 0.5, 1, and 2 Hz.

2.2.6.6 Antagonist experiments to block neuronal transmission

To inhibit communication between neurons via excitatory or electrical synapses, specific antagonists were applied to the cultures. Excitatory glutamatergic signaling through NMDA and AMPA receptors was blocked with AP5 and NBQX. Gap-junction (electrical) coupling was inhibited using carbenoxolone (CBX). Initially, baseline activity was recorded for all samples, and when stimulation was part of the experiment, the same stimulation protocol was included in each recording. A portion of the medium was removed and kept aside to ensure the cells remained covered. NBQX (final concentration 10 µM) and AP5 (50 µM) were then added and the cultures incubated for 30 min before a second recording. Afterward, the medium was aspirated, and the cultures were rinsed once with DPBS+/+ and twice with fresh BrainPhys. The previously collected medium was returned to the wells and incubated for 1 h prior to the next recording. For experiments with single-neuron circuits and their controls, CBX (final concentration 100 µM) was subsequently introduced and incubated for 30 min. The medium was again removed, cultures washed as before, and the saved medium combined with fresh BrainPhys was reintroduced for a final 1 h incubation before the last recording session.

2.2.6.7 Data analysis of SNAP electrophysiological recordings

All extracellular recordings were analyzed with custom Python scripts built around the SpikeInterface framework (Buccino et al., 2020). Signals first underwent a second-order Butterworth high-pass filter at 100 Hz, followed by global common-median referencing (Rolston et al., 2009). In SNAP experiments, conventional spike-sorting algorithms could not reliably isolate single-neuron spike trains. Several spike-sorting algorithms were evaluated but consistently failed to give a realistic estimate of the number of neurons in the circuits, instead yielding pronounced overcounts (Supplementary Figure 7d). This outcome aligns with earlier findings that separating individual neuronal signals becomes especially challenging when APs are densely packed and fire synchronously (Bakkum et

al., 2013; Garcia et al., 2022a). Under these conditions, overlapping or superimposed waveforms interfere with template-matching and similar algorithms.

To address this limitation, a more straightforward, electrode-based spike detection workflow was used and no sorting was applied for any of the analyzed SNAP datasets. Spikes were identified by detecting all negative peaks in each electrode trace using a threshold of five times the median absolute deviation and an exclusion window of 0.2 ms. These detected peaks and their timestamps were treated as spike trains for subsequent network analyses.

To calculate AP propagation velocities, a custom script was used on the preprocessed raw data. Peak times or spike timestamps alone were not reliable enough for extracting AP propagation speed. Especially in bursts, it is impossible to track the same AP across electrodes with certainty because overlapping waveforms, superposition, and electrode-dependent waveform changes obscure the signal (Bakkum et al., 2013; Gold et al., 2006). To overcome this, the onset of the voltage rise of both, isolated APs or bursts, was used as the temporal reference. Following a standard thresholding method, the reference point was defined as the moment the voltage exceeded five times the baseline standard deviation. This time was extracted for every electrode using the same algorithm. Randomly chosen spikes with their approximate spike times (~1 ms before the event) were supplied to the algorithm. The routine calculated the baseline standard deviation over the preceding 10 ms and identified the point where the signal exceeded five times this value. Threshold-crossing times across electrodes, together with known inter-electrode distances from the microfluidic layout, were used to compute conduction speeds. Per condition, sample and time point at least 10 APs were extracted. Events were not used if another spike occurred within the 10 ms baseline window to avoid distorted noise estimates. This window provided a stable measure while leading to minimal exclusions given the low average firing rate. All data from different circuits, experimental conditions, were acquired and processed using the same standardized procedures.

To assess alterations in firing regularity and burstiness, which are hallmarks of functional excitatory connectivity, ISI distributions were analyzed. Because the circuits were small and contained only a few neurons and electrodes, signals from the same neuron were often recorded by several electrodes. This overlap made correlation-based methods

unsuitable for detecting firing changes across electrodes. ISI analysis, by contrast, allowed to quantify the regularity of activity patterns on each electrode directly, without requiring spike sorting to isolate individual neurons. ISI histograms were generated at 1 ms resolution from consecutive spike times. Differences between baseline and excitatory-blocker conditions were quantified using the Kullback-Leibler divergence (Kullback and Leibler, 1951),

$$KL(P, Q) = \sum_x P(x) \log\left(\frac{P(x)}{Q(x)}\right),$$

where P(x) and Q(x) are the two ISI distributions. Only electrodes with > 400 ISI measurements were included to prevent sparse-data artifacts. Electrodes in motifs of SNAP circuits and population controls were compared individually.

Circuit synchrony was evaluated with the Spike-contrast metric (Ciba et al., 2018) via the Elephant library package (Denker et al., 2018). Bursts were identified using the MaxInterval method (Cotterill et al., 2016) with these criteria: minimum inter-burst interval 200 ms, minimum burst duration 1 ms, at least three spikes per burst, and a maximum intra-burst ISI of 10 ms. Network-wide bursts were accepted only when spikes appeared on all electrodes within a 5 ms window.

To calculate the participation ratio (PR), an estimate of the dimensionality of network activity, the correlation matrix of binned spike trains (5 ms bins) was constructed and its eigenvalues λ_i used to calculate:

$$PR = \frac{1}{N} \frac{(\sum_i \lambda_i^a)^2}{\sum_i (\lambda_i^a)^2}$$

where N is the number of units (Clark et al., 2023). PR is in the range of $0 \leq PR \leq 1$. Higher PR values indicate more independent neuronal firing and higher dimensionality, whereas lower values reflect stronger coupling, collective dynamics, and lower dimensionality.

For optogenetic response analysis, spikes were counted in a 150 ms window following each light-on trigger, and only peaks exceeding an amplitude of 50 µV were accepted to eliminate potential stimulation artifacts.

Statistical evaluations were carried out in GraphPad Prism, which was also, along with custom Python scripts, used for generating plots. Specific statistical tests and

corresponding sample sizes are indicated in the respective figure captions. Neuronal survival rates were determined by counting the neurons detected in fluorescence microscopy images for each individual circuit.

2.2.6.8 Immunofluorescence

Cultures were fixed at RT for 15 min using 4 % paraformaldehyde (PFA). After rinsing with DPBS+/+, cells were permeabilized in 0.2 % Triton X-100 prepared in DPBS+/+ and blocked for 30 min at RT with 5 % donkey serum in the same buffer. Primary antibodies for anti-GFP and anti-βIII-tubulin (both 1:200) were applied overnight at 4 °C. After three washes with 0.1 % Triton X-100 in DPBS+/+, samples were incubated for 2 h at RT with the secondary antibody diluted in blocking solution (goat anti-chicken Alexa Fluor 488, 1:500). Following another three washes with 0.1 % Triton X-100 in DPBS+/+, nuclei were counterstained with Hoechst (1:2,000 in DPBS+/+) for 5 min at RT. After three final washes with DPBS+/+, coverslips were mounted in ProLong Diamond Antifade Mountant and imaged using an Echo Revolve microscope.

3. Results

Some of the results presented here were published in scientific journals or as a preprint already. My own contribution to the work is stated within each publication. A summary of my contributions is given in section 10. Also, throughout this section I point out contributions and work from others where applicable.

3.1 Neuronal activity under altered gravity

The content of the following section has been published in Striebel et al. (2023) on which I am a first author under a CC-BY 4.0 license. My own contribution to the work involved experimental planning, sample preparation, data acquisition, data analysis, preparation of the figures and writing the manuscript. This was a collaboration project with other scientists contributing to experimental planning, data acquisition, and writing.

3.1.1 Hypergravity influences hiPSC-derived neural network activity

To address the need for precise electrophysiological measurements in demanding altered gravity platforms and conditions, we employed low-footprint MEA technology. Its flexible and user-friendly design makes it suitable for deployment in complex gravity research settings. Specifically, we showed that MEA systems can be integrated into altered gravity research platforms (Supplementary Figure 1). Our setup ensured cell viability by providing stable physiological conditions for the neural cultures. It can run autonomously without the need for direct interaction. It also shields biological samples from external disturbances, such as electromagnetic interference and pressure fluctuations. This enabled investigation of how human neuronal networks respond to changes in gravity. To the best of our knowledge, the method was not applied to study neurons in altered gravity before.

We examined the electrophysiological behavior of human neural networks derived from hiPSCs under varying gravitational forces. More specifically, we used iNGN neurons that provide a homogeneous neural model (Busskamp et al., 2014; Kutsche et al., 2018; Lam et al., 2017). After 21 days, iNGN neurons possess functional synapses and AMPA receptors, as verified by immunohistochemistry and patch-clamp experiments (Lam et al., 2017). Thus, these cells provide a valuable platform for fundamental and biomedical

research by offering entire neural networks for *in vitro* studies rather than single neurons, a limitation of previous studies of neurons in altered gravity.

To study the effects of different levels of hypergravity on the activity of hiPSC-derived neural networks, we installed the experimental setup on the SAHC. For each centrifuge run, two MEA chips were placed into the MEA system within the experimental module providing physiological conditions. A run consisted of a 10 min baseline recording of spontaneous, non-evoked electrophysiological activity at normal gravity (1 *g*), a 5 min exposure to 4 *g* or 6 *g* hypergravity and another 5 min post-centrifugation baseline recording to assess potential adaptation processes (Figure 3-1a). To account for standard fluctuations in neural activity, we performed control recordings over the same time period without any gravitational stimulus. No significant differences in firing rates were observed across phases without gravity changes (Supplementary Figure 2). Phase-contrast microscopy conducted before and after the experiments confirmed the viability and structural integrity of the neural networks, with no adverse morphological effects observed (Figure 3-1b,c).

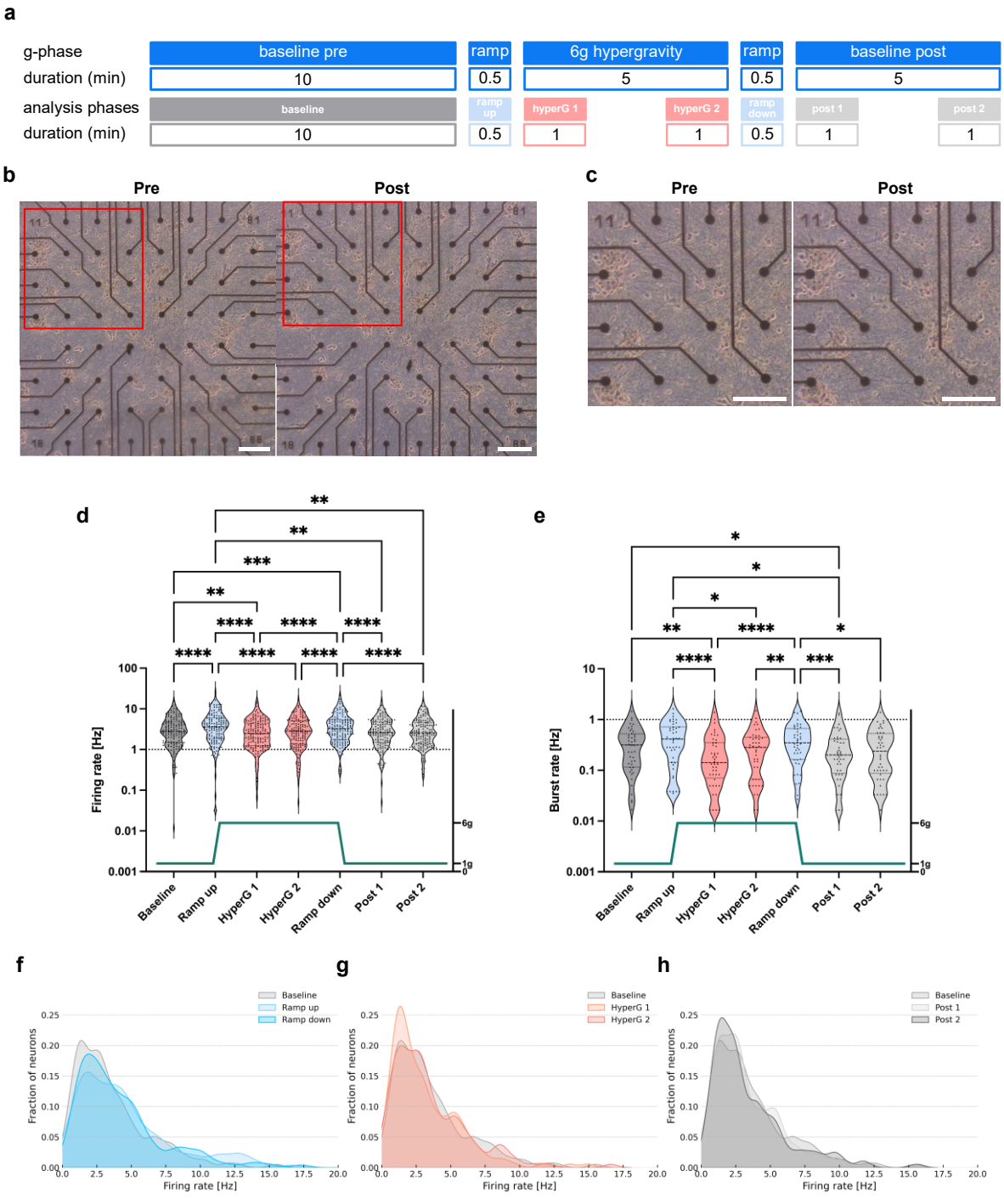

Figure 3-1: Morphological and electrophysiological analysis of human neuronal networks exposed to 6 *g* hypergravity using a centrifuge. a, Schematic overview of the experimental timeline highlighting distinct phases analyzed and their respective durations. **b**, Representative phase-contrast images of a neuronal culture on a MEA chip before and after exposure to hypergravity. **c**, Enlarged views of the regions outlined in red in panel (**b**). **d**, **e**, Quantification of firing rates (**d**) and burst rates (**e**) of neuronal networks subjected to 6 g hypergravity. Data were collected from five MEAs across six

centrifugation runs. A total of 144 and 44 individual units were included in the statistical analysis of firing and burst rates, respectively. Repeated measures one-way ANOVA followed by Tukey's multiple comparisons test was applied. *$p < 0.05$, **$p < 0.01$, ***$p < 0.001$, and ****$p < 0.0001$. Violin plots show distribution with dashed lines marking the first, second (median), and third quartiles. **f–h**, Density plots of firing rate distributions during the ramp phase (**f**), constant hypergravity phase (**g**), and post-exposure phase (**h**), each compared to the baseline condition. Scale bars, 200 µm. *Figure adapted from Striebel et al. (2023); original data, analysis and visualization generated by the author.*

The various experimental phases were analyzed separately. To capture potential adaptation processes during the hypergravity and baseline post phases, a 1 min data sample was analyzed at the beginning and at the end of each phase and compared (Figure 3-1a). Upon reaching 6 g hypergravity (hyperG 1), a reduction in firing rates was observed (Figure 3-1d). However, firing rates returned to baseline levels during the later stage of hypergravity exposure (hyperG 2), suggesting the activation of an adaptation mechanism. A rise in activity was observed during the transition back to 1 *g* (ramp down), and firing rates stabilized to baseline values within 1 min after re-establishing 1 *g* conditions. No significant differences in activity were detected between the beginning and end of the post-hypergravity phase (post 1 and post 2). Changes in activity dynamics were more apparent when looking at mean burst rates. Burst rates increased during the ramp phases, showed a transient dip at the onset of hypergravity, and returned to baseline levels after sustained 5 min exposure to 6 *g* hypergravity (Figure 3-1e). After deceleration the re-adaption to baseline could not be observed in the first minute (post 1) but after 5 min (post 2). This is indicating active processes rather than passive adaptation, which would be instantaneous. Notably, burst rate changes between baseline and ramp phases were not significantly different as opposed to changes observed in firing rates.

In a similar experiment involving hypergravity exposure at 4 *g*, no significant differences in firing rates were detected across phases. Only comparing the deceleration (ramp down) to the second post-exposure phase (post 2) showed a significant difference. Burst rates only were significant when comparing baseline to the acceleration (ramp up), deceleration (ramp down), and the 5 min re-adaptation phase (post 2) (Supplementary Figure 3).

These findings underscore the importance of mechanical stimuli in modulating neuronal activity. We observed significant changes in spontaneous activity primarily as a result of acceleration and deceleration phases while re-adaption occurred during sustained

hypergravity. Density plots illustrating the firing rate distribution of measured units across experiment phases revealed shifts toward higher frequencies during ramp phases, with local maxima between 8 and 13 Hz for both acceleration and deceleration (Figure 3-1f-h). The shift was more pronounced during acceleration than deceleration. During the hypergravity phase and especially the initial hyperG 1 phase, a greater proportion of neurons exhibited lower firing rates (around 2 Hz), although some high firing rate-units could still be observed. This could indicate that different subpopulations of neurons react differently to changes in gravity. The firing rate distribution during the late hypergravity phase (hyperG 2) resembled baseline levels, suggesting recovery. Post-exposure phase distributions showed only minor changes compared to baseline. Additionally, changes in the shape of APs were observed. Both the amplitude and half-width of spikes were significantly altered in response to hypergravity (Supplementary Figure 4).

3.1.2 Microgravity influences hiPSC-derived neural network activity

Experiments conducted under hypergravity conditions indicate that neurons respond to gravitational changes through variations in their average firing and burst rates that re-adapt on diverse timelines. Alterations in firing rates were evident during the acceleration and deceleration phases, and during sustained 6 *g* exposure. These findings suggest that gravity-sensitive mechanisms regulate neuronal dynamics, implying that microgravity could similarly provoke a response. To explore the effects of mechanical unloading in a microgravity environment on neuronal network activity, we employed the MEA experiment setup (Supplementary Figure 1) on a drop tower platform, providing a high-quality microgravity environment (approximately 10^{-5} to 10^{-6} *g*) for 4.7 s.

To assess the structural integrity and morphology of the neural cultures, we acquired microscope images before and after the drop experiment. A representative culture is shown in Figure 3-2b. All five neural networks remained securely attached to the MEA post-drop, and no noticeable morphological changes were observed.

We recorded neuronal activity, starting with a 10 min control under standard gravity (1 *g*) prior to each drop and continued during the microgravity phase induced by free fall,

followed by an impact that produced a brief hypergravity pulse of roughly 30-40 *g* (Figure 3-2a). We proceeded recording for an additional 10 min to capture activity during the re-adaptation phase. We divided the entire dataset into four segments: pre-drop baseline, microgravity, impact, and post-drop baseline (as shown in Figure 3-2a). Data from corresponding phases across all drops were pooled and analyzed to assess firing and burst rates in the neural networks. Analysis of firing rates showed a significant increase during the microgravity phase compared to baseline, indicating heightened neuronal activity in weightless conditions (Figure 3-2c). This activity increased further during the impact phase. Following the drop, firing rates decreased and returned to baseline levels within 10–20 s, showing no significant difference from the initial pre-drop readings, suggesting effective recovery from gravitational changes (Supplementary Figure 5). Burst rates showed a comparable pattern to firing rates. A significant rise in burst activity occurred during microgravity, with a further increase during the impact (Figure 3-2d). Burst rates normalized within 10 min after the drop. The consistency of baseline activity before and after the drop demonstrated both the stability and resilience of the neural networks.

A density plot illustrating the distribution of single-unit firing rates showed that the pre- and post-drop profiles were alike. However, during microgravity, the peak shifted from approximately 3 to 4 Hz, with a greater concentration of higher-frequency units (15–28 Hz, see Figure 3-2e). The impact phase produced an even more pronounced shift, with two primary peaks emerging at 8 and 20 Hz (Figure 3-2f). To further investigate how individual neuronal subpopulations responded to microgravity, we tracked the firing rate changes of units with low, medium, and high baseline activity. The 10 units with lowest firing rates during baseline showed increased activity in microgravity (Figure 3-2g), while the 10 units in the middle of the firing rate spectrum at baseline also increased, though a few decreased (Figure 3-2h). The 10 highest firing units exhibited mixed responses, with roughly half increasing and half decreasing their firing rates (Figure 3-2i). These findings indicate a complex and heterogeneous response to gravitational stimuli at the single-unit level. No uniform shift in the rate distributions is observed suggesting units reacting differently to changes in gravity.

Overall, these electrophysiological assessments demonstrate that neural networks adjust their spontaneous activity in response to gravity alterations. In addition, a significant

decrease in AP amplitude was observed during the impact phase compared to baseline (Supplementary Figure 4), while other phases showed no significant changes in AP amplitude or half-width. The most immediate and substantial effects resulted from acute gravity changes. Within less than 5 s, microgravity triggered marked increases in both firing and burst rates. Importantly, these functional responses occurred without compromising cellular integrity or morphology, as evidenced by the networks' ability to return to baseline activity and maintain structural stability throughout the experiment.

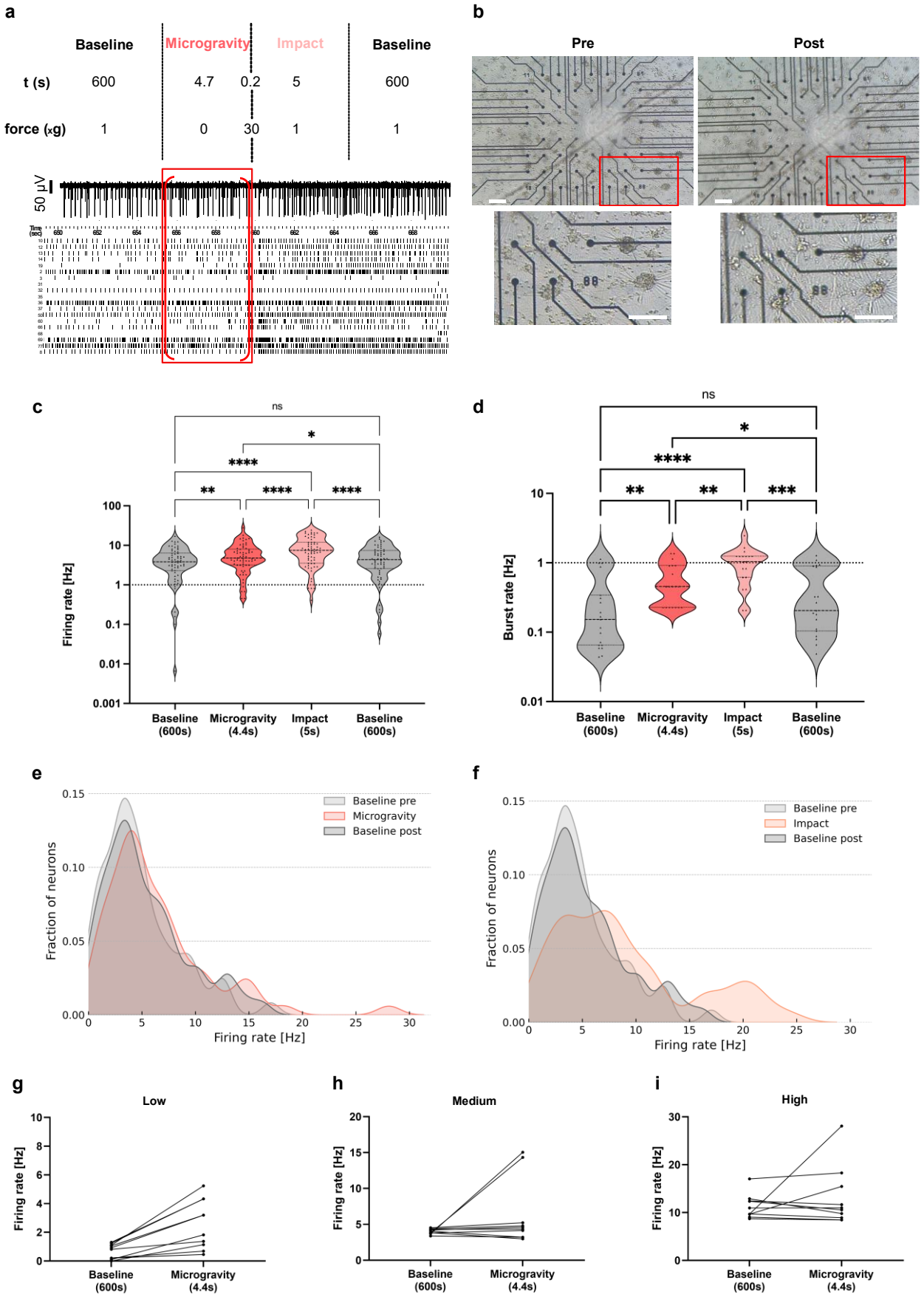
a
Baseline
Microgravity
Impact
Baseline
t (s)
600
4.7
0.2
5
600
force (xg)
1
0
30
1
1
50 µV
b
Pre
Post
c
ns
*
****
**
****
****
Firing rate [Hz]
100
10
1
0.1
0.01
0.001
Baseline (600s)
Microgravity (4.4s)
Impact (5s)
Baseline (600s)
d
ns
*
****
**
**
***
Burst rate [Hz]
10
1
0.1
0.01
Baseline (600s)
Microgravity (4.4s)
Impact (5s)
Baseline (600s)
e
Baseline pre
Microgravity
Baseline post
Fraction of neurons
0.15
0.10
0.05
0.00
0
5
10
15
20
25
30
Firing rate [Hz]
f
Baseline pre
Impact
Baseline post
Fraction of neurons
0.15
0.10
0.05
0.00
0
5
10
15
20
25
30
Firing rate [Hz]
g
Low
Firing rate [Hz]
10
8
6
4
2
0
Baseline (600s)
Microgravity (4.4s)
h
Medium
Firing rate [Hz]
20
15
10
5
0
Baseline (600s)
Microgravity (4.4s)
i
High
Firing rate [Hz]
30
20
10
0
Baseline (600s)
Microgravity (4.4s)

Figure 3-2: Microgravity-induced changes in neuronal network activity recorded during drop tower experiments. a, Schematic of the experimental timeline with corresponding gravitational conditions and durations. A raster plot displaying spiking activity from all recorded units on one exemplary MEA and representative trace from a single electrode are shown. The microgravity interval is highlighted in red. Analysis was conducted on the segment marked by red brackets, excluding safety margins before and after the microgravity phase. **b**, Representative phase-contrast images of a MEA chip before and after exposure to the drop. A magnified view of the region highlighted in red is shown below to assess morphological stability. **c**, Violin plots comparing average firing rates across four key phases: pre-drop baseline (gray), during microgravity (orange), impact period immediately following microgravity (light orange), and the post-drop baseline (gray). Data were collected from five MEAs across three independent cell preparations, with 63 units included in the firing rate analysis. Black triangles indicate values from individual neuronal units. Statistical significance was assessed using repeated measures one-way ANOVA with Tukey's post hoc test (ns, not significant; *$p < 0.05$, **$p < 0.01$, ***$p < 0.001$, and ****$p < 0.0001$). Quartiles are indicated by dashed lines. **d**, Violin plots comparing burst rates for the same four experimental phases as in (**c**), based on 19 neuronal units. **e, f**, Distribution plots of firing rates during microgravity (**e**) and impact (**f**) phases, compared with pre- and post-drop conditions. **g–i**, Analysis of neuronal subgroups reveals distinct changes in activity in response to microgravity. Units were grouped based on their baseline firing rate into low (**g**), medium (**h**), and high (**i**) activity categories. Connected dots represent changes in firing rate of the same unit between baseline and microgravity phases. Scale bars, 200 µm. *Figure adapted from Striebel et al. (2023); original data, analysis and visualization generated by the author.*

3.2 Morphological and functional long-term development of 2D neuronal networks *in vitro*

The content of the following section has been published in Habibey et al. (2022b) on which I am a first author under a CC-BY 4.0 license. My own contribution to the work involved data collection, analysis and visualization as well as writing. This was a collaboration project with other scientists contributing to all parts of the work.

3.2.1 Evolving network morphology and activity maps reflect correlated long-term dynamics

To monitor ongoing structural rearrangements in neuronal cultures and how they are paralleled by shifts in electrophysiological activity patterns over time, we employed HD-MEAs. These devices enable comprehensive scanning of the entire sensor surface to produce activity maps that reflect the firing of neurons across thousands of electrodes with

a subcellular resolution. Starting at 22 dpi, we obtained whole-sensor microscopy images (n = 3) and compared them with corresponding activity scans (Figure 3-3a).

Initial imaging revealed neurons distributed evenly across the sensor area. As cultures matured, these neurons gradually assembled into compact groups (clusters) with diameters less than 50 µm, a process observed beginning around 28 dpi. These micro-clusters became interconnected by axon bundles spanning the array, and manual tracking confirmed progressive neuronal aggregation (Figure 3-3a-d). Over time, some smaller aggregates merged to form larger clusters exceeding 100 µm in diameter. Continuous positional shifts of both individual neurons and the formed clusters on the sensor surface were highlighted through time-lapse microscopy.

By tracking 904 neurons across three HD-MEA cultures, we quantified neuronal displacement weekly and cumulatively over the experimental period (Figure 3-3e,f). Displacement was significantly greater before cluster formation, with neurons traveling an average of 28.04 ± 1.40 µm per week at 28 dpi, compared to just 19.14 ± 0.75 µm per week at 76 dpi (Figure 3-3e). Across individual chips, total neuronal movement ranged from 35.95 ± 1.96 µm to as much as 1027 ± 52.20 µm. After two months, the mean net displacement from each neuron's initial position at 22 dpi reached 224.00 ± 10.10 µm (Figure 3-3f). Notably, 76.01 % of all tracked neurons had shifted between 50 µm and 200 µm over this period.

Given the 17 µm spacing between electrodes, this level of migration translates to a shift over approximately 12 or more electrodes, on average. Since neuronal signals are typically recorded across multiple electrodes simultaneously, even small movements can significantly alter the spatial pattern of recorded activity. Consistently, we observed that the spatial distribution of active electrodes changed over time, in line with neuronal movement (Figure 3-3c). Comparing imaging and recordings confirmed that changes in activity map geometry and position were tightly linked to the physical movement of neurons and their clusters (Figure 3-3d). These findings indicate that over the course of weeks and months, different regions of the same network are captured by distinct subsets of electrodes. Similar morphological plasticity was also evident in prior recordings using standard low-density MEAs (Schmieder et al., 2022).

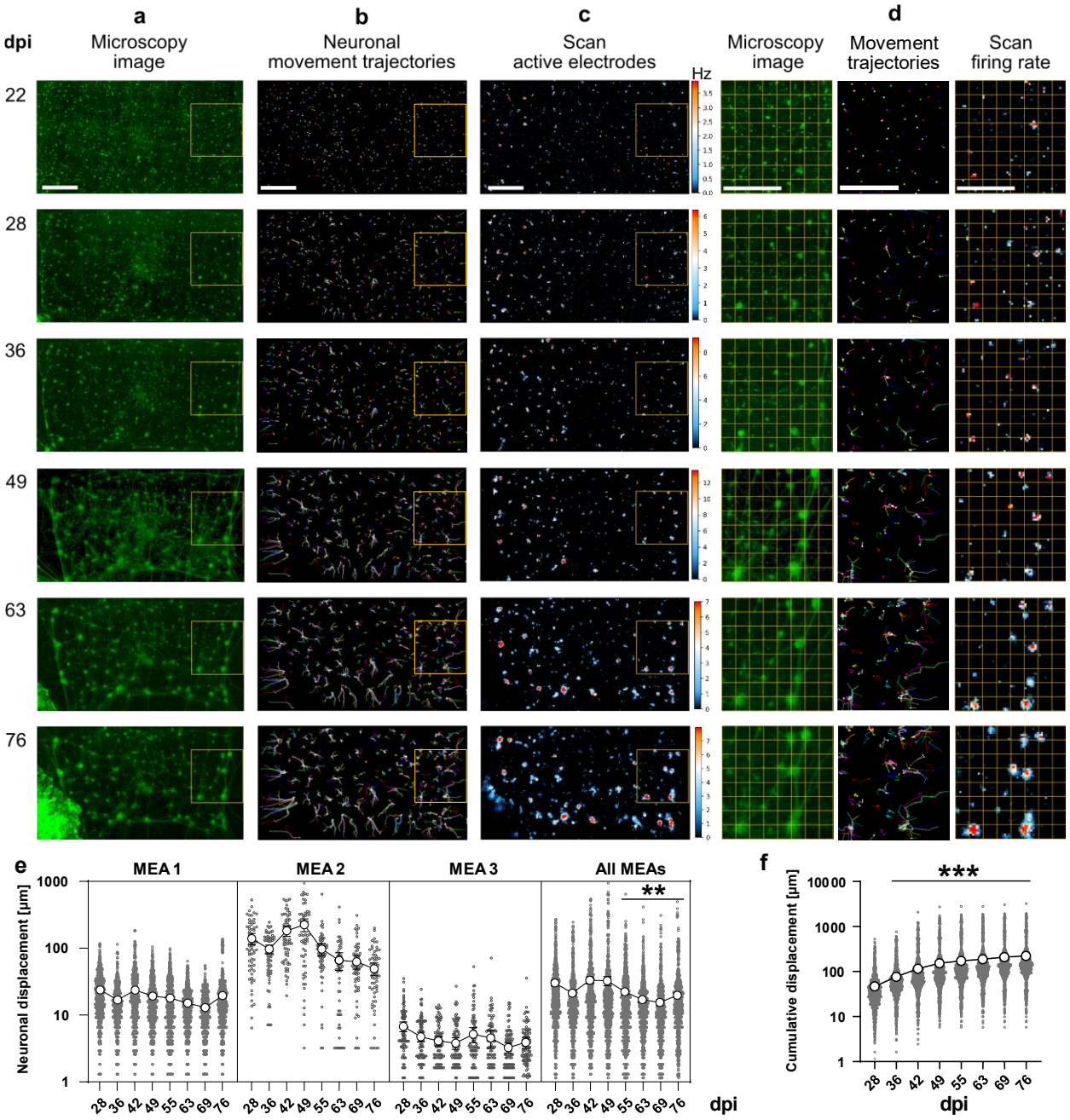

Figure 3-3: Morphological and functional evolution of iNGN-derived neuronal networks over time. a, Wide-field fluorescence images of neuronal cultures were generated at various days post induction (dpi) by stitching together 40 individual microscope fields per time point. **b**, Neuronal migration paths were reconstructed by tracking somatic positions across sequential morphological images. **c**, Functional activity maps were generated via HD-MEA-based activity scans, which involved 30 s recordings from each electrode across the full array. Electrodes exhibiting firing activity are shown in blue, with color coding representing relative firing rates: black for inactive, blue for moderate, and red for high activity. Note that firing rate scales are not normalized across days; color intensities reflect relative activity within each recording session. **d**, Detailed snapshots of a specific network region (highlighted in yellow in **a**-**c**) are shown across three columns: morphology (left), movement paths of neurons (middle), and

corresponding firing activity maps (right). Frames represent an area of approximately 56 × 56 electrodes; yellow squares indicate subregions of ~7 × 7 electrodes. **e**, Weekly displacement measurements for individual neurons are shown across three HD-MEA cultures (721, 68, and 115 neurons tracked per chip, respectively; total n = 904). Each dot represents the distance a single neuron moved compared to its previous position. Group averages are shown as larger circles with connecting lines (***p* < 0.01 vs. 28 dpi). **f**, Cumulative displacement of neuron soma positions was calculated between 22 and 76 dpi for all tracked neurons across the three cultures. A significant shift in average position was observed over time (***p* < 0.001 vs. 28 dpi). Data were analyzed using the Kruskal-Wallis followed by Dunn's multiple comparisons test. Scale bars, 500 µm. *Figure adapted from Habibey et al. (2022b).*

3.2.2 Long-term evolution of spontaneous activity and bursting in iNGN-derived neural networks

To investigate the maturation of spontaneous network activity, we analyzed recordings from three HD-MEA cultures at multiple time points (Figure 3-4a). Early electrophysiological data, recorded prior to 22 dpi, showed isolated APs across sparse electrodes (Figure 3-4b). By 28 dpi, local bursting appeared in individual neurons but lacked network-wide propagation (Figure 3-4c). From approximately 49 dpi onward, synchronized burst activity began to emerge, becoming robust and widespread by 63 dpi. The frequency of these coordinated events increased with time (Figure 3-4c).

The number of active neurons detected on each HD-MEA grew significantly with culture age, from 272.3 ± 46.51 neurons at 22 dpi, to 613.3 ± 83.32 at 49 dpi, peaking at 870.0 ± 59.73 neurons at 83 dpi (Figure 3-4d). Similarly, the subset of neurons participating in burst events expanded from only 6 neurons at 22 dpi to 92.67 ± 21.34 at 49 dpi and 213.3 ± 21.14 at 90 dpi (Figure 3-4d).

To quantify general excitability, we calculated mean AP firing rates by dividing the total number of spikes by the recording duration. Firing rates peaked around 49 dpi at 2.69 ± 0.07 Hz, significantly increasing from 22 dpi (1.55 ± 0.073 Hz), followed by a mild decline to 1.96 ± 0.05 Hz at 90 dpi (Figure 3-4e). Distribution analysis revealed that a majority (51.69 %) of neurons fired at less than 2 Hz, while only 22.08 % showed mean firing rates above 5 Hz (Figure 3-4f). Burst frequency steadily rose throughout culture development, reaching 0.07 ± 0.01 Hz at 49 dpi and 0.23 ± 0.01 Hz at 90 dpi, up from an initial 0.01 ± 0.00 Hz at 22 dpi (Figure 3-4g). Burst durations increased sharply between 42 dpi and

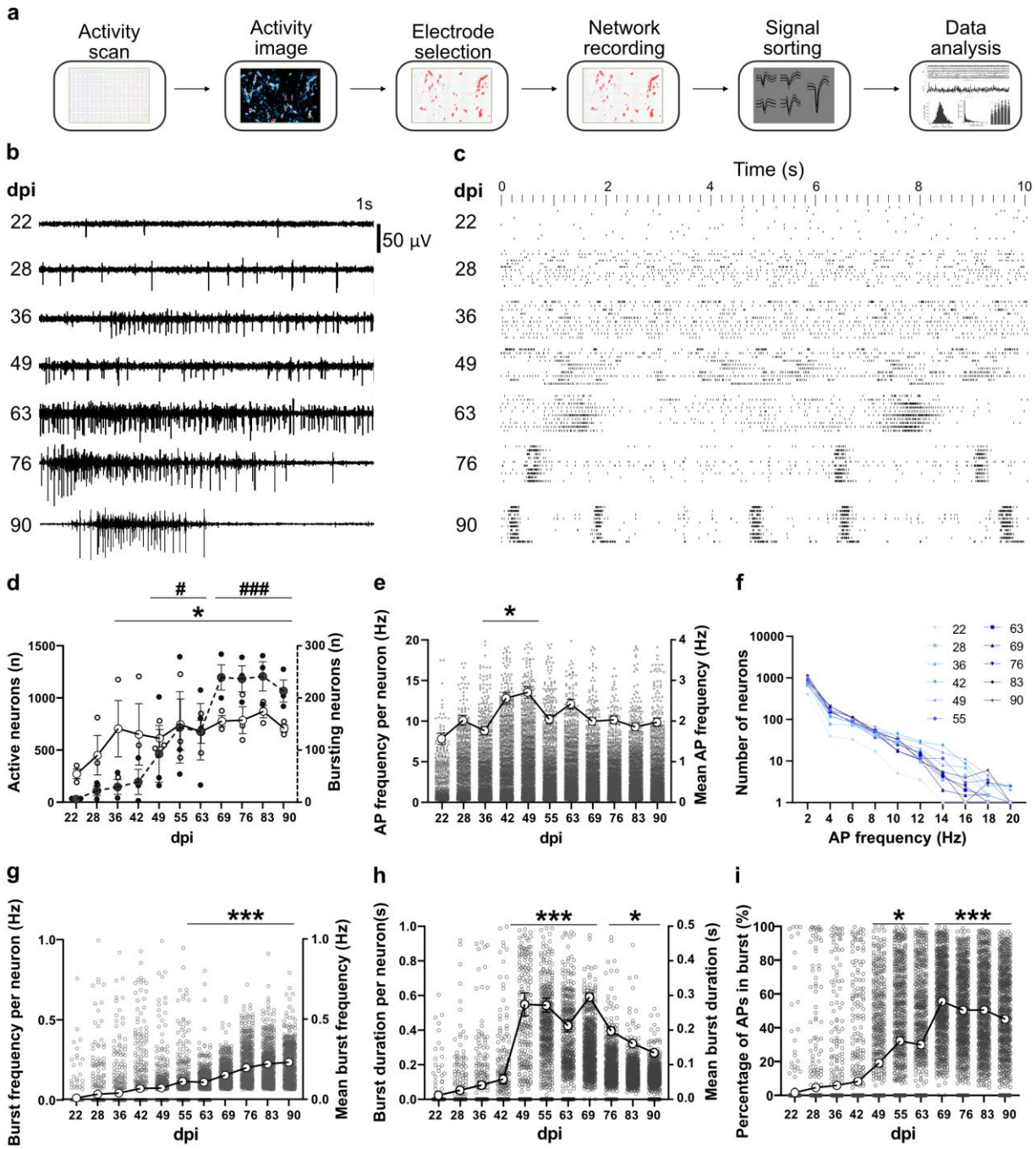

Figure 3-4: Progressive maturation of spontaneous activity and burst dynamics in hiPSC-derived neuronal networks. a, Overview of the data collection and analysis workflow. After performing a full activity scan across the HD-MEA array, electrodes with the highest spiking activity were selected for subsequent long-term recordings. The acquired data underwent spike sorting to identify individual neuronal units, followed by extraction of spike timestamps for quantitative analysis. **b**, Representative electrophysiological traces recorded from a single electrode at various days post induction (dpi), highlighting the evolution of spontaneous neuronal activity over time. **c**, Raster plots illustrating 10 s segments of spiking activity in ten neurons (one per row) at multiple dpi. The transition from sparse firing to more coordinated activity is visually evident. **d**, Quantification of the total number of active neurons (defined as > 0.1 Hz) and the

subset participating in network bursts across development. **e**, Mean firing rates of neurons at each time point, calculated by dividing total spikes by the duration of recording. **f**, Distribution of neurons across firing rate ranges at various dpi. **g-i**, Developmental trends in burst features including: (**g**) burst frequency, (**h**) burst duration, and (**i**) proportion of total spikes occurring within burst events. n > 1,065 neurons per recording session from N = 3 MEAs. Each data point in panels. **d-i** represents one neuron's value for the respective parameter. Kruskal-Wallis followed by Dunn's multiple comparisons test. **p* < 0.05, ****p* < 0.001 vs. 22 and 28 dpi; bursting neurons: #*p* < 0.05, ###*p* < 0.001 vs. 22, 28, and 36 dpi. *Figure adapted from Habibey et al. (2022b).*

49 dpi, from 0.05 ± 0.01 s to 0.27 ± 0.02 s (Figure 3-4h) and remained elevated until 69 dpi (0.29 ± 0.01 s), before declining to 0.14 ± 0.01 s by 90 dpi, which was still significantly higher than the earliest time point. The proportion of total APs occurring within bursts also increased over time. This value reached its highest point at 69 dpi, when 55.51 % of spikes were part of burst events (Figure 3-4i), and remained elevated for the remainder of the recording period. This could indicate that the network and synapses are functionally matured and developed after this time.

3.2.3 Emergence of high-frequency spiking and fast-spiking neurons

To investigate the presence of fast-spiking neurons we analyzed neuronal firing using instantaneous firing rates. For example, inhibitory neurons fire at high rates with frequencies greater 100 Hz. While the average AP frequency across an entire recording provides a broad view of neuronal excitability, it masks periods of silence or bursting. Instantaneous frequency, computed from individual ISIs, offers a more fine-grained look at neuronal responsiveness, allowing us to capture transient high-frequency events and maximum firing rates.

Over a three-month period and across three HD-MEAs, encompassing more than 1065 neurons, both the average and maximum instantaneous firing frequencies increased substantially. At 22 dpi, the average instantaneous rate was 8.44 ± 0.62 Hz, with a peak of 315 Hz. By 90 dpi, these values rose to 29.88 ± 0.93 Hz and 588.1 Hz, respectively (Figure 3-5a,b). Notably, a marked increase occurred after 63 dpi, with mean rates reaching 31.57 ± 1.12 Hz and peak rates at 567.9 Hz (Figure 3-5b).

Additionally, the proportion of spike events occurring in the 150–600 Hz range rose from 2.66 % at 22 dpi to 11.33 % by 90 dpi (Figure 3-5c). Likewise, the number of neurons

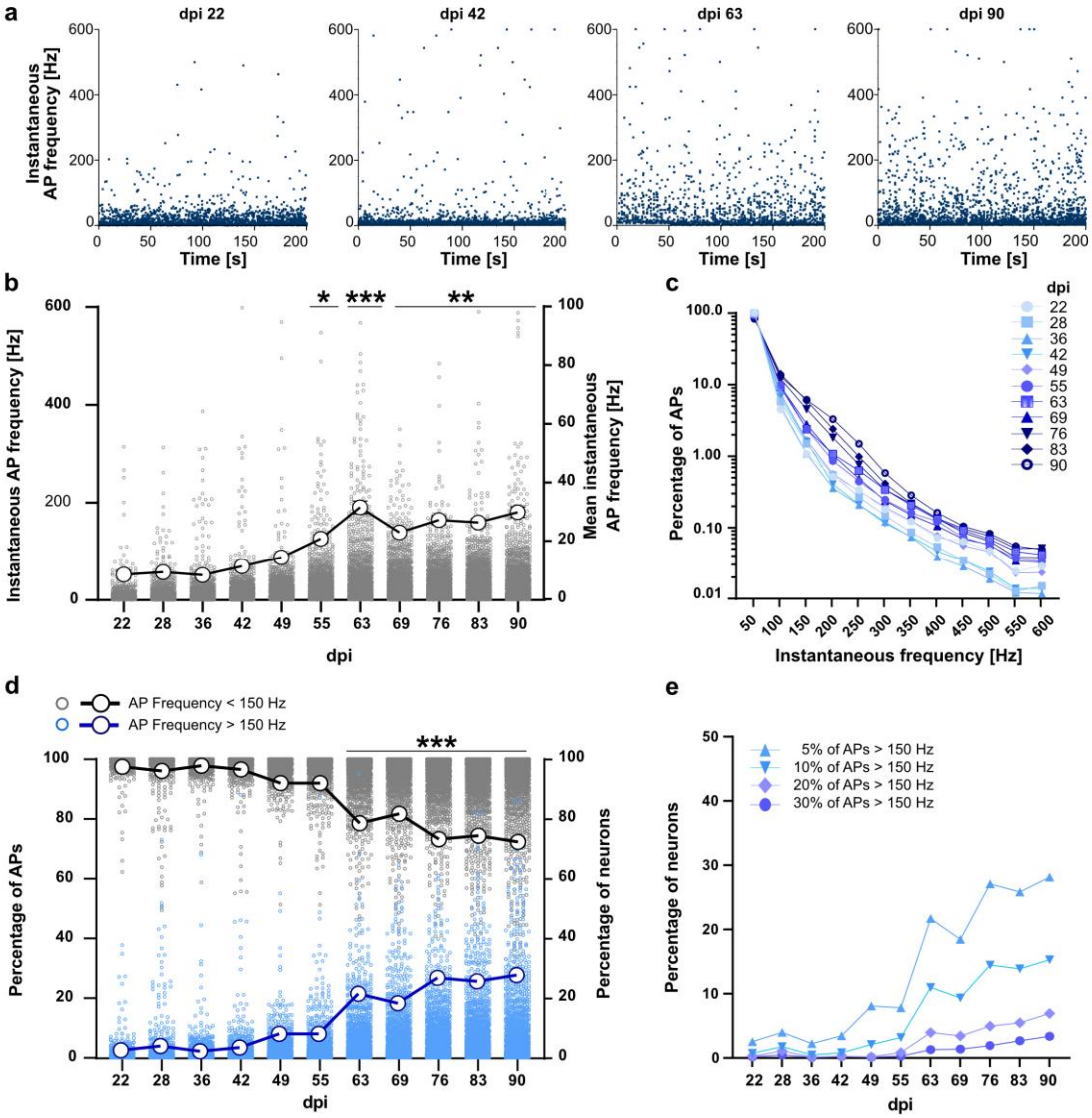

Figure 3-5: Emergence of fast-spiking neuronal activity during long-term culture. **a**, Representative instantaneous firing frequencies of a neuron recorded over 200 s. Each dot corresponds to the calculated instantaneous frequency from a pair of consecutive APs (interspike interval) in this period. **b**, Summary of average instantaneous firing rates across the neuronal population at multiple days post induction (dpi). Each small dot represents the mean instantaneous firing frequency of an individual neuron. Large circles and the connecting line indicate the mean of these neuron-level averages at each time point. **c**, Distribution of instantaneous rates across frequency ranges at each dpi, revealing how the proportion of high-frequency events evolves with network development (n > 400,000 spiking events per time point, N = 3 MEAs). **d**, Breakdown of the proportion of low (< 150 Hz, gray) and high-frequency (> 150 Hz, blue) firing events across all neurons (n > 1064 neurons). The blue (black) curve reflects the proportion of neurons exhibiting ≥ 5 % (≥ 95 %) of their spiking events in the high (low)-frequency range. **e**, Percentage of neurons with 5 %, 10 %, 20 %, or 30 % of their firing events occurring in the high-frequency range (> 150 Hz), demonstrating an age-dependent increase in fast-spiking behavior. Comparisons across time points were assessed using the Kruskal-Wallis test with Dunn's post-hoc analysis: **p* < 0.05, ***p* < 0.01, ****p* < 0.001 compared to earlier time points (22, 28, 36, and 42 dpi). *Figure adapted from Habibey et al. (2022b).*

exhibiting at least 5 % of their spikes above 150 Hz increased significantly, from 2.52 % to 27.74 % over the same period (Figure 3-5d,e), indicating the gradual emergence of fast-spiking neuronal populations during network maturation.

3.2.4 Modulation of network activity by excitatory synaptic antagonists

To determine the role of excitatory synaptic transmission in shaping network dynamics, we performed electrophysiological recordings before, during, and after pharmacological inhibition of AMPA and NMDA receptors using NBQX and AP5, respectively. The presence of mature synapses is a hallmark of mature neuronal networks and would demonstrate the developmental status of the network.

During treatment, synchronized bursting disappeared entirely. Instead, only isolated APs and small local bursts were recorded (Figure 3-6a). Raster plots reinforced this observation, revealing a complete loss of global burst synchronization under glutamatergic blockade (Figure 3-6b). After the compounds were washed out, burst features re-emerged, indicating that the loss of synchrony was reversible (Figure 3-6a,b). Under baseline conditions 595 active neurons were measured which dropped to 407 during NBQX + AP5 exposure. Firing rate of these remained statistically unchanged (1.13 ± 0.04 Hz at baseline vs. 1.39 ± 0.11 Hz during treatment, $p = 0.35$; Figure 3-6c). Upon washout, firing rates increased significantly to 2.12 ± 0.09 Hz. Only a small subset of neurons displayed any bursting behavior during treatment (Figure 3-6b-e). Under antagonist treatment, burst duration, frequency, and the proportion of APs within bursts all declined significantly (Figure 3-6d-f), which indicates that network activity is largely governed by mature excitatory synapses. These measures rebounded after washout, with burst frequency and duration rising significantly and the percentage of APs in bursts increasing as well.

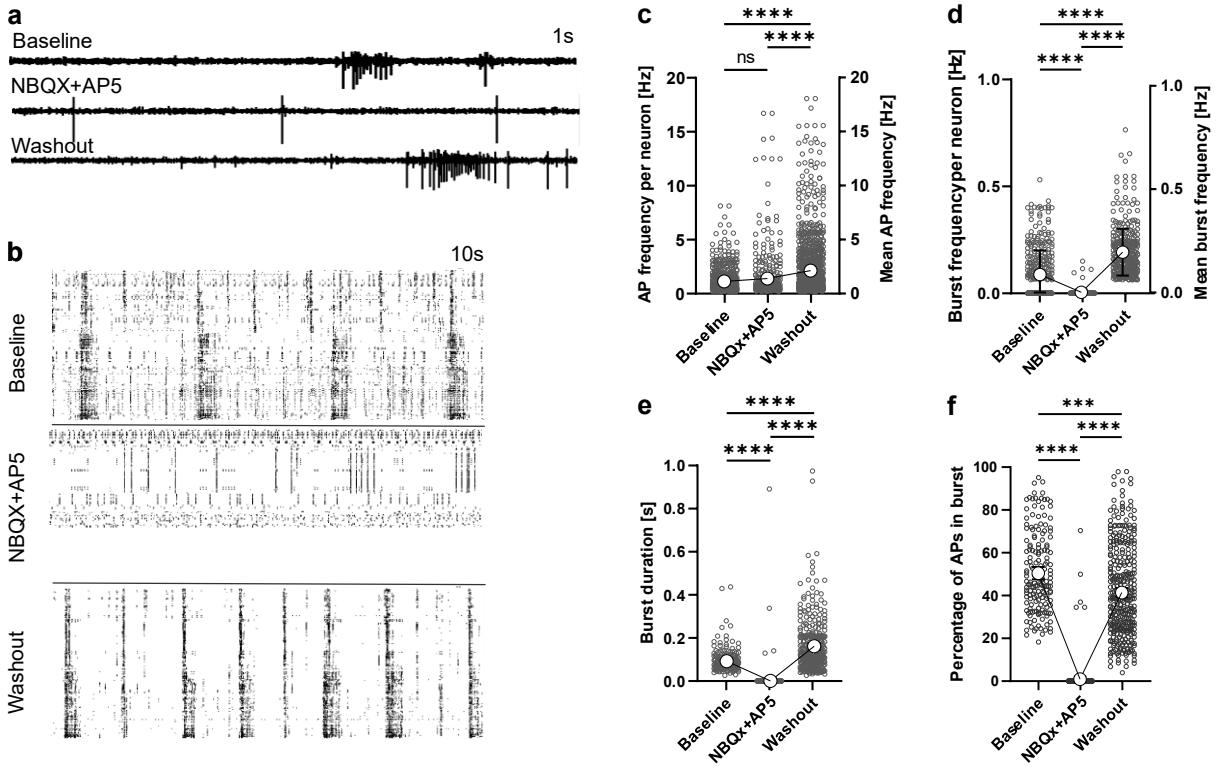

Figure 3-6: Modulation of network activity by blocking AMPA and NMDA receptors. To investigate the role of excitatory glutamatergic signaling in mature hiPSC-derived neuronal networks, AMPA and NMDA receptors were inhibited using a combination of NBQX and AP5 at 118 days post induction (dpi) in two MEAs. Network activity was recorded under three conditions: before treatment (baseline), during receptor blockade, and after washout. **a**, Representative voltage traces from two electrodes illustrate the suppression of synchronized network bursts during NBQX + AP5 treatment and partial recovery following washout. **b**, Raster plots show spike timing across all active electrodes with each row corresponding to one electrode. **c**, Quantitative comparison of network features including AP frequency, burst rate, burst duration, and the proportion of APs occurring within burst. Each data point represents a single neuron. Kruskal-Wallis test with Dunn's post hoc correction (***$p < 0.001$, ****$p < 0.0001$). *Figure adapted from Habibey et al. (2022b).*

It is important to note that medium changes themselves can modulate network activity for up to 24 h. In this experiment, the washout phase necessarily involved a medium exchange, making it difficult to fully separate the two effects and could thus represent a confounding factor. However, because no medium exchange occurred during drug application, the observed suppression of bursting can be directly attributed to glutamatergic blockade.

3.2.5 Impact of GABA-A receptor inhibition on network dynamics

To explore how inhibitory signaling shapes network activity, we applied the GABA-A receptor antagonist gabazine and recorded changes before, during, and after treatment. A representative trace from an electrode during gabazine exposure showed increased bursting (Figure 3-7a). Raster plots revealed that network burst frequency rose in the presence of the antagonist and remained elevated even after washout (Figure 3-7b). Reasons for this could be the high affinity of gabazine (Rognan et al., 1992) or a persistent perturbation of firing dynamics. Quantitative analysis showed that mean AP firing frequency increased from 2.18 ± 0.07 Hz at baseline to 3.43 ± 0.12 Hz during gabazine treatment (Figure 3-7c). After the drug was removed, firing rates remained elevated at 4.16 ± 0.17 Hz.

Burst frequency increased significantly under gabazine (0.42 ± 0.01 Hz vs. 0.27 ± 0.01 Hz at baseline) and stayed elevated after washout (0.41 ± 0.02 Hz; Figure 3-7d). Conversely, burst duration decreased under gabazine from 0.16 ± 0.01 s to 0.10 ± 0.01 s, and this reduction persisted after washout (Figure 3-7e). Similarly, the percentage of spikes occurring within bursts fell from 61.33 ± 0.99 % to 45.25 ± 1.23 % during treatment, remaining below baseline levels even after the drug was removed (Figure 3-7f). These results indicate that there are functional inhibitory synapses present in the networks and that they contribute to shaping network activity.

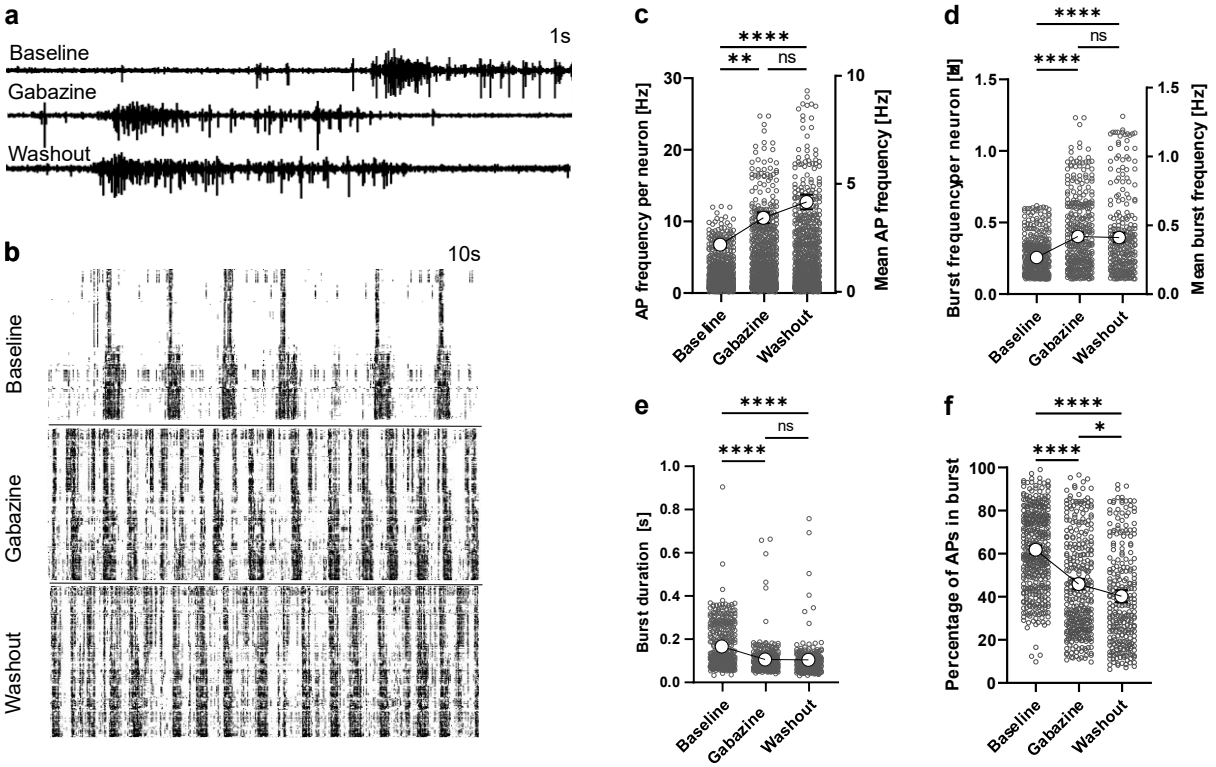

Figure 3-7: Impact of GABA-A receptor inhibition on neuronal network activity. To assess the contribution of inhibitory synaptic transmission, GABA-A receptors were pharmacologically blocked using gabazine at 120 days post induction (dpi) in two MEAs. Network activity was recorded across three conditions: baseline, during gabazine application, and following washout. **a**, Representative voltage traces from one electrode. **b**, Raster plots show spike timing across all active electrodes with each row corresponding to one electrode. **c**, Quantitative comparison of network features including AP frequency, burst rate, burst duration, and the proportion of APs occurring within burst. Each data point represents a single neuron. Kruskal-Wallis test with Dunn's post hoc correction (*$p < 0.05$, **$p < 0.01$, ***$p < 0.001$, ****$p < 0.0001$). *Figure adapted from Habibey et al. (2022b).*

3.3 *In vitro* plasticity and learning experiment

Continuous microscopy of the samples confirmed structural integrity of the networks over time. Populations of iNGN-EGFP neurons are arranged in the desired geometry and axons spread laterally through the reservoirs (Figure 3-8a). As a result of the repeated training sessions, we hypothesized that electrical activity recorded from electrodes in the input and output layers would become increasingly correlated, reflecting adaptation to the patterned stimuli. To obtain a global measure of synchronous and low-dimensional activity, I first calculated the PR for each culture. The PR was computed at multiple time points throughout the experiment for both the baseline phase (no stimulation) and the test

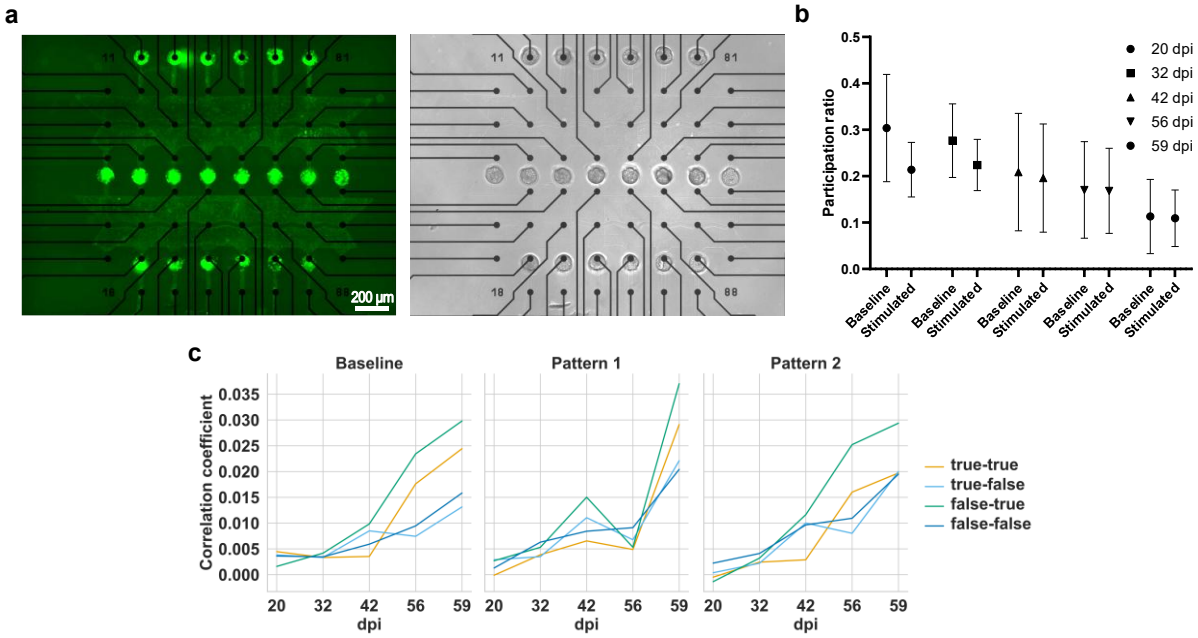

Figure 3-8: Development of correlation measures in the *in vitro* learning experiment. **a,** Fluorescence (EGFP) and brightfield image of a representative sample at 42 dpi. **b,** PR during baseline and test stimulation, averaged across all samples and stimulation patterns, shown for multiple experimental time points (mean ± SD). **b,** Average correlation coefficient between the activity of input- and output-layer electrodes at the same time points. Correlations were calculated for correct classifications (true input electrodes paired with true output electrodes) and for three control conditions (true–false, false–true, and false–false electrode pairs). Baseline and test recordings for patterns 1 and 2 were analyzed separately. N = 4 MEAs.

phases, during which only the designated input electrodes for patterns 1 and 2 were stimulated separately. Across all samples I observed a gradual decrease in PR as cultures aged and the experiment progressed, and this decline was consistent for both baseline and stimulation periods (Figure 3-8b). Of note, in earlier timepoints the PR during the test stimulation phases was lower than during baseline. However, none of these differences reached statistical significance as assessed by one-way ANOVA.

To examine correlations more specifically between the input and output layers, I next calculated the average pairwise correlation coefficient between electrodes in these two layers at the same experimental time points. For each stimulation pattern I focused on the "correct classification" pairs, i.e., correlations between the true input electrodes and their corresponding true output electrodes. As controls I also computed correlations for the three alternative pairings: true–false, false–true, and false–false electrode pairs (Figure 3-8c). All groups showed a slight upward trend in correlation over time, both during baseline and during pattern-specific stimulation. However, these increases were subtle.

Interestingly, in nearly all cases the correlation between true input and true output electrodes was lower than that observed for the false–true control pairs. Overall, I observed a very low correlation with coefficients being smaller than 0.04.

Finally, when I compared individual samples, time points, and stimulation patterns, I found no consistent or robust evidence of a progressive increase in correlated activity between the input and output layers, i.e., no evidence of LTP or *in vitro* learning was observed.

3.4 Engineered neuronal circuits with single-cell precision allow dissection of neuronal interactions

Content of the following section is currently in press (Striebel et al., 2025b) and is partly published as a preprint under a CC-BY-NC-ND 4.0 license (Striebel et al., 2025a). The research was led by me. All experiments, data collection and analysis as well as writing and figure preparation were carried out by me.

3.4.1 Increased sensitivity to synaptic perturbations

In order to create SNAPS, single neurons were first placed in a microscaffold (Figure 3-9a). A challenge in development of SNAPs was maintaining cell viability after single-cell placement. In stem cell protocols, inhibitors of the ROCK pathway are often used to prevent detachment-induced apoptosis (anoikis) (Watanabe et al., 2007). Based on ROCK inhibition, a more recent approach utilizes a combination of four compounds (known as CEPT), which further enhances post-passaging survival (Chen et al., 2021). I hypothesized that similar strategies could promote the survival of isolated neurons in the setup. Apoptosis and anoikis as a result of detachment or changes in chemical signaling and presence of factors play an important role in brain development to sculpt the CNS (Yuan and Yankner, 2000). Single and especially young and immature neurons are susceptible to these types of processes. Adding a ROCK inhibitor improved short-term survival (up to five days post-seeding; Figure 3-9b), but did not significantly benefit longer-term viability. In contrast, CEPT treatment led to markedly improved survival rates. Ara-C is commonly introduced into differentiating stem cell cultures after induction and immediately prior to reseeding to remove undifferentiated, proliferating cells. However,

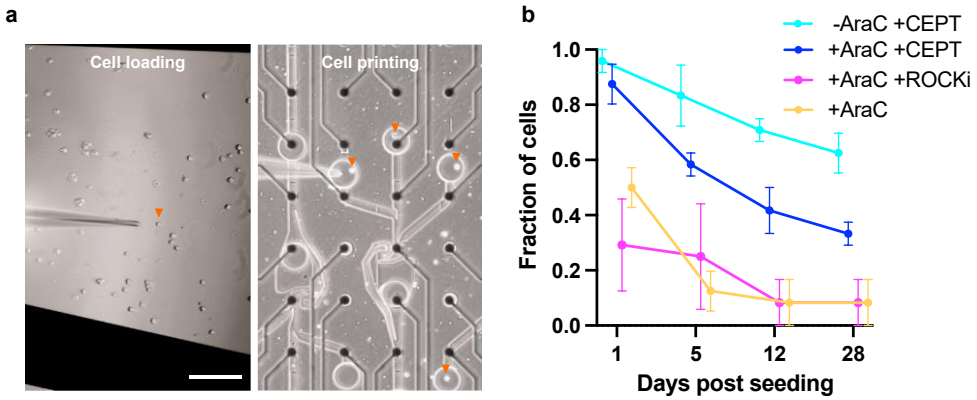

Figure 3-9: Seeding and survival of single neurons in the SNAP platform. a, Manual seeding of individual neurons into microwells using micropipette-assisted placement. Left: A single iNGN cell (orange arrow) is aspirated by a micropipette. Right: Placement of the neuron into a designated microwell. All successfully positioned cells are marked with orange arrows. The microfluidic architecture is aligned with recording electrodes of the MEA (black dots). **b**, The survival rate of iNGN neurons was assessed across different culture protocols at multiple time points following seeding. The combination of CEPT cocktail without Ara-C treatment resulted in the highest cell viability over time. Data represent fractions of surviving cells from three independent replicates per condition and time point (N = 3, mean ± SEM). *Figure is part of a submission currently in press (publication will be covered under a CC-BY 4.0 license) (Striebel et al., 2025b). Original data and visualization generated by the author. The submission is based on a preprint (Striebel et al., 2025a) and involves the same co-authors.*

because Ara-C has been associated with neurotoxicity and DNA damage (Geller et al., 2001), I evaluated the effect of leaving it out. When CEPT was applied without Ara-C, the survival rate rose to approximately 62.5 % of cells 28 dpi (Figure 3-9b). Since iNGNs typically become electrophysiologically active by 14 dpi and form functional synapses by 21 dpi (Lam et al., 2017), this approach enabled me to construct uniform, functional circuits suitable for parallel experiments. I further expanded the SNAP method and showed that it is possible to include two neuron subtypes in the same circuit: iNGN and EMX1 neurons (Supplementary Figure 6a). This shows the flexibility of the platform and adaptability to build more complex circuits that could make them closer to *in vivo* situations, and allow the inclusion of diseased or modified cells to build model systems. To the best of my knowledge, this is the first platform enabling bottom-up assembly of defined neural networks with such precision.

Initial designs featured tri-neuron circuits arranged in a Y-shaped microfluidic layout (Figure 3-10a). Immunostaining confirmed neuronal identity and desired circuit architecture. EMX1 neurons exhibited comparable viability to iNGNs (Figure 3-10b).

Among 40 assembled circuits, 13 remained intact and usable for functional assays at 22 dpi in the iNGN condition (Figure 3-10c). To assess synaptic functionality and maturity, I applied a combination of AMPA (NBQX) and NMDA (AP5) receptor blockers. Inhibiting excitatory synaptic signaling is expected to alter firing patterns, revealing the presence of functional synaptic connectivity. Indeed, this led to significant alterations in neuronal activity patterns in both iNGN and EMX1 SNAPs. As a control, I analyzed bulk-seeded cultures where multiple neurons were introduced per microwell. These controls also responded to the antagonists, but the effects were less obvious (Figure 3-10d). ISI histograms, a fundamental readout of neuronal firing behavior, shifted significantly in SNAPs after drug treatment, whereas changes in the controls were less distinct (Figure 3-10e). ISI is frequently employed to assess firing regularity, burst dynamics, and neuronal excitability which are key indicators of excitatory synaptic activity that can drive synchronized or burst-like events across a network. I quantified the differences between baseline and post-treatment histograms using KL divergence (Kullback and Leibler, 1951), which revealed a significantly larger response in SNAP circuits compared to population controls for both neuronal subtypes (Figure 3-10f,g). These findings suggest that SNAPs provide a clearer and more sensitive readout of pharmacological interventions, likely because the sparse and structured activity is less influenced by network-level noise present in denser cultures. This further suggests that SNAPs are more suitable as a model to study specific kinds of neuronal behavior as compared to populations of cells.

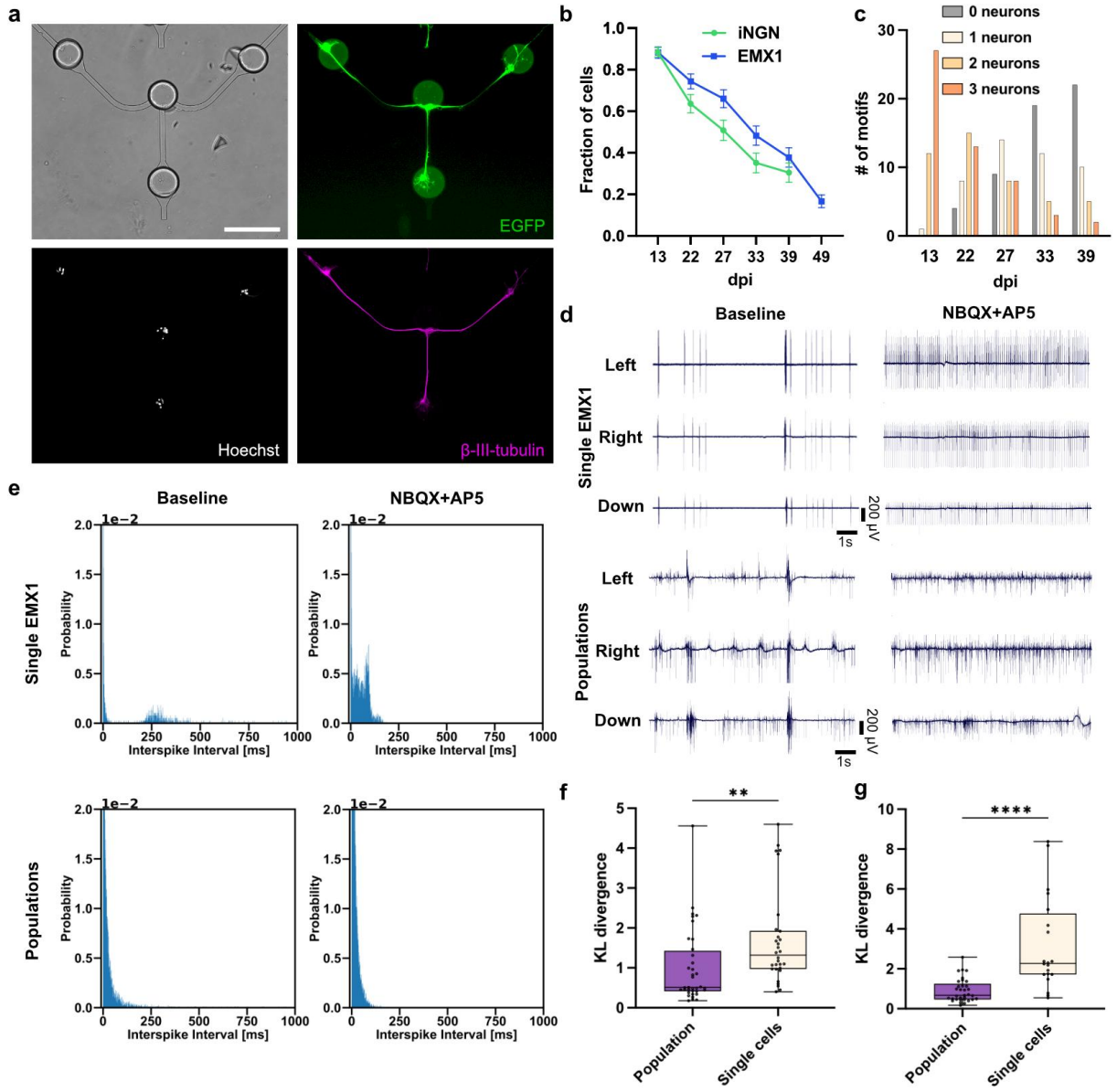

Figure 3-10: SNAP circuits display enhanced sensitivity to synaptic antagonists. **a**, A typical three-neuron circuit motif comprising iNGN neurons positioned in microwells within a microfluidic device. Brightfield imaging shows the microwell arrangement, with individual neurons seeded into the outer wells. Immunofluorescence staining includes βIII-tubulin (neurites), Hoechst (nuclei), and constitutively expressed EGFP. Scale bar, 200 µm. **b**, Longitudinal quantification of neuronal survival for iNGN and EMX1 cell types in Y-shaped three-cell SNAP motifs at multiple days post induction (dpi), expressed as fraction of surviving cells in mean ± SEM (iNGN: *n* = 64 motifs; EMX1: *n* = 60 motifs). **c**, Frequency distribution of motifs containing different numbers of iNGN neurons over time. A total of 10 samples, each with 4 circuit motifs, were assessed. **d**, Raw extracellular recordings from three electrodes positioned in a representative SNAP motif with 3 EMX1 neurons (left, right, bottom channels). Shown are recordings under baseline conditions (left) and following pharmacological inhibition with the excitatory synaptic blockers NBQX and AP5 (right). Traces are also shown for EMX1 populations cultured in the same microstructure. **e**, ISI histograms for representative electrodes from both SNAP circuits and neuron populations. Histograms are shown before (left) and after (right) NBQX + AP5 application. In the SNAP configuration, the ISI distribution is visibly altered after drug

treatment. **f, g**, KL divergence between ISI distributions under baseline conditions and after NBQX + AP5 exposure. Comparisons are made for SNAP motifs and neuronal populations derived from EMX1 (**f**) and iNGN (**g**) neurons. In both cases, SNAP circuits exhibited significantly higher KL divergence, suggesting greater responsiveness to synaptic inhibition. Box plots display the 25th–75th percentile range with median; whiskers represent the full data range. Statistical analysis via two-tailed Mann-Whitney test (EMX1: n = 36 electrodes for population, n = 30 for single-neuron motifs; iNGN: n = 33 and n = 20, respectively). $^{**}p \leq 0.01$, $^{****}p \leq 0.0001$. *Figure is part of a submission currently in press (publication will be covered under a CC-BY 4.0 license) (Striebel et al., 2025b). Original data and visualization generated by the author. The submission is based on a preprint (Striebel et al., 2025a) and involves the same co-authors.*

3.4.2 Signs of ephaptic coupling in SNAPs

To enable ephaptic interactions, it is essential to bring axons into close physical proximity. To this end, I designed specialized microfluidic architectures that direct axonal outgrowth from four neurons into a common, unidirectional path (Figure 3-11a,b) (Forró et al., 2018). Each microfluidic device, compatible with square 60 electrode MEA (8×8 arrangement), contained four such identical circuit modules (Figure 3-11b). Interestingly, neurons housed in these axon-guiding configurations exhibited improved viability compared to those in earlier Y-shaped designs (Figure 3-11c,d).

To confirm that the circuits were functionally connected and transmission other than ephaptic coupling could be blocked, I applied a combination of excitatory synaptic blockers (Figure 3-11e). I observed changes in electrophysiological output and ISI distributions in the presence of antagonists, as captured by KL divergence metrics and similar to previous observations in tri-neuron circuits. Unidirectional signal propagation in the circuits was verified by cross-correlation analysis (Supplementary Figure 7c).

I next turned to a hallmark feature of ephaptic coupling: modulation of AP conduction velocity. The structured nature of SNAPs allowed me to track AP velocity in relation to the number of interacting neurons. As more axons were brought into proximity, I detected a significant reduction in AP velocity (Figure 3-12a). To rule out contributions from chemical or electrical synapses, I repeated the measurements under treatment with glutamatergic blockers, as well as the gap junction inhibitor (CBX). These treatments did not produce notable changes in AP velocity (Figure 3-12b), indicating a non-synaptic origin for the slowing.

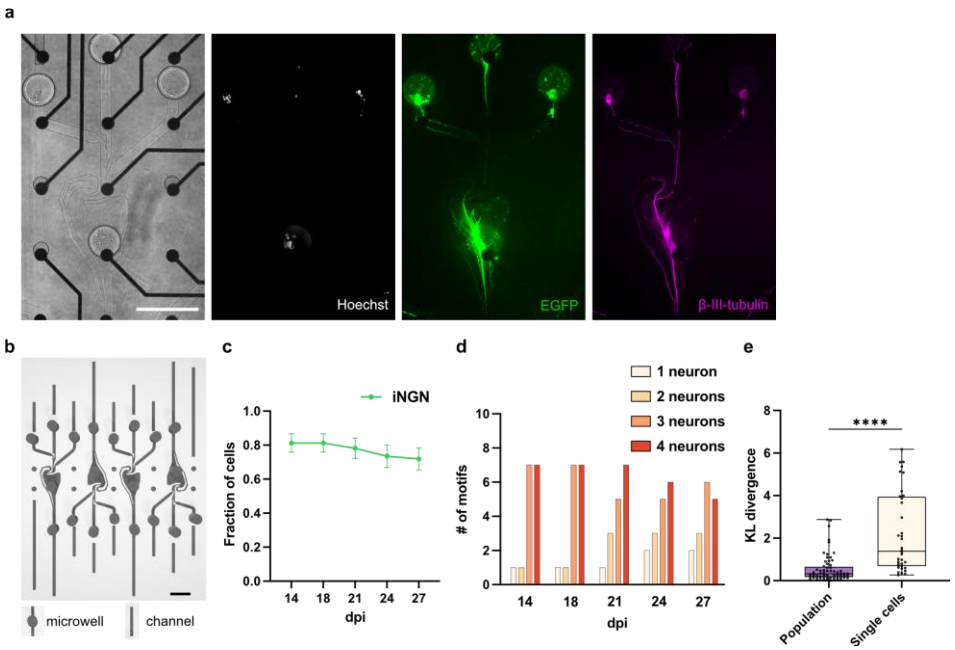

Figure 3-11: Directionally guided neuronal circuits with single-cell precision. **a**, Example of a 4-neuron directional circuit comprised of iNGN cells cultured in the microfluidic device. Brightfield image reveals microwells occupied by single neurons, with a central “stomach”-shaped guide structure directing neurite outgrowth downward as described in (Forró et al., 2018; Girardin et al., 2022). Fluorescence images show βIII-tubulin (neurites), Hoechst (nuclei), and constitutive EGFP. Scale bar, 200 µm. **b**, Schematic of four identical microstructures as arranged on a single MEA chip, enabling parallel analysis. **c**, Quantification of neuron viability across several days post-induction (dpi) within directional 4-cell SNAP motifs (mean ± SEM; *n* = 16 circuits). **d**, Distribution of motifs containing 1-4 neurons at each dpi. Four independent samples, each with four circuits, were analyzed. **e**, KL divergence comparing ISI histograms before and after application of synaptic antagonists NBQX and AP5. Directional SNAP motifs show a significantly greater divergence than population controls cultured in the same microfluidic devices, supporting the presence of functional excitatory synapses and increased pharmacological responsiveness. Box plots show interquartile range with median; whiskers span full data range. Two-tailed Mann-Whitney test: *n* = 64 (population) and *n* = 36 (single neuron circuits). ****$p \leq 0.0001$. *Figure is part of a submission currently in press (publication will be covered under a CC-BY 4.0 license) (Striebel et al., 2025b). Original data and visualization generated by the author. The submission is based on a preprint (Striebel et al., 2025a) and involves the same co-authors.*

The microfluidic design includes both isolated and converging axonal regions, which allowed a spatial comparison of conduction speed. As predicted for ephaptic interactions, APs traveled faster in isolated axons and slowed when the axons were bundled together (Figure 3-12c). The experimental platform enables detailed monitoring of the same circuits over time. For example, in the circuits shown in Figure 3-12d, I tracked AP velocity longitudinally across different dpi. As some neurons degenerated and were lost from the circuit, reducing axonal bundling, AP velocity increased. This dynamic shift supports the

conclusion that axonal number directly influence conduction speed. Interaction length of axons was predicted by theory to have an influence on AP velocity (Anastassiou et al., 2010). This prediction was confirmed and quantified by analyzing AP velocity as a function of axonal overlap (Figure 3-12e). Early after cell placement, axons remained mostly separate, corresponding to faster AP propagation. Over time, axons formed bundles, coinciding with a drop in velocity. I again observed faster AP propagation after degeneration of two neurons reducing ephaptic coupling strength.

Another characteristic of ephaptic interactions is increased synchrony in neuronal firing (Han et al., 2018; Katz and Schmitt, 1940; Schmidt and Knösche, 2019). Even raw electrophysiological traces revealed coordinated activity within directional SNAP circuits (Figure 3-12j), with bursts of spikes separated by quiet periods. This synchronization was quantified by the spike-contrast measure, which rose with increasing numbers of interacting neurons (Figure 3-12f) (Ciba et al., 2018). A similar trend was observed in the PR (Clark et al., 2023), a proxy for the dimensionality of network activity. PR decreased as more neurons contributed to the circuit, consistent with more synchronized, low-dimensional dynamics (Figure 3-12g). Classical network synchrony metrics such as burst rate and frequency of synchronous network-wide bursts also scaled with neuronal number (Figure 3-12h,i), providing converging evidence for ephaptic coupling.

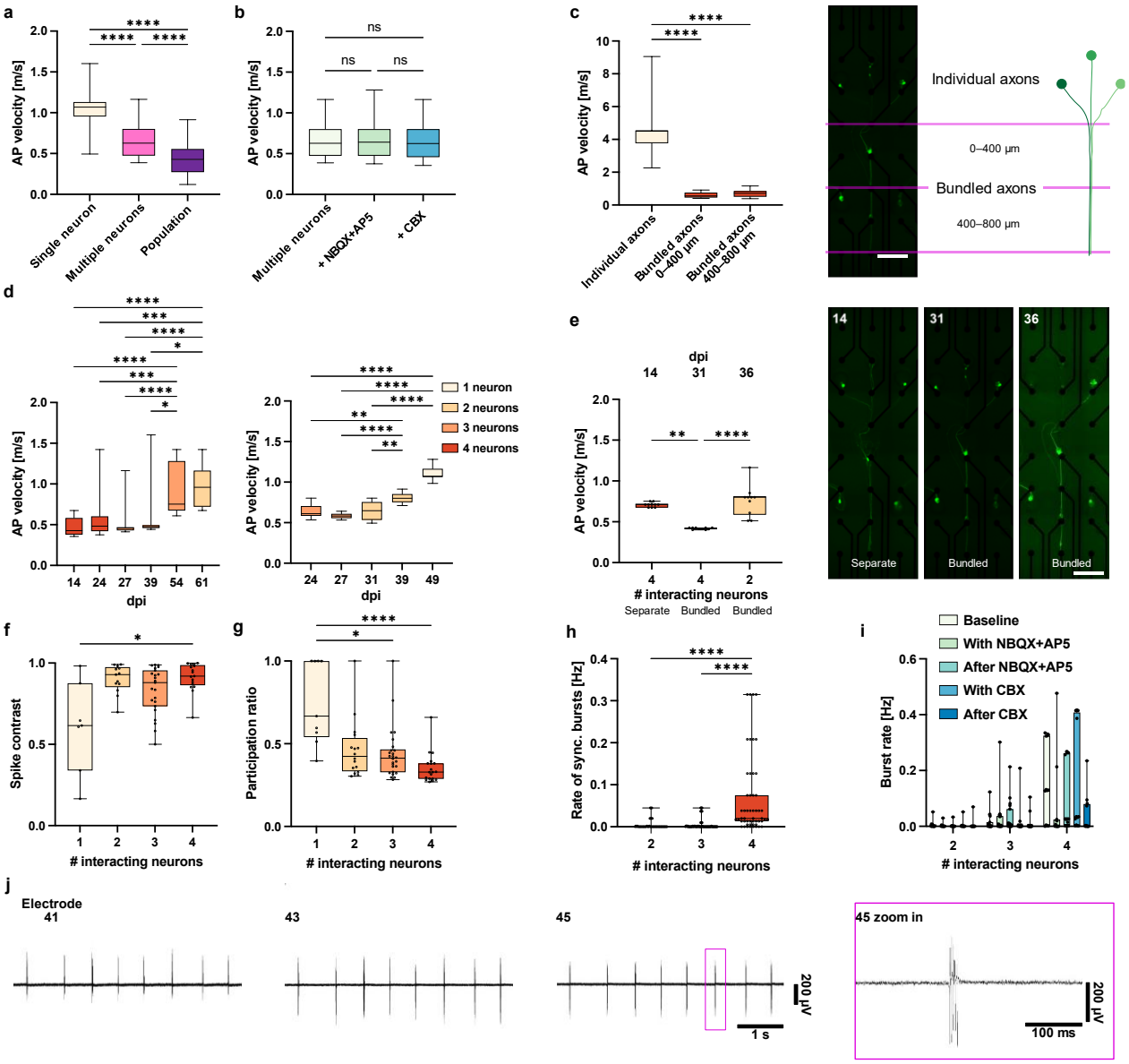

Figure 3-12: Evidence for ephaptic coupling in directional SNAPs. a, AP conduction velocity measured in directional microfluidic circuits shows a significant decrease as the number of interacting iNGN neurons increases from single to multiple neurons (2–4) and populations. Kruskal-Wallis with Dunn's post hoc analysis (Single: *n* = 60 APs; Multiple: *n* = 100 APs; Population: *n* = 79 APs). **b**, In circuits of multiple neurons, the addition of excitatory synaptic blockers (NBQX + AP5) or a gap junction inhibitor (CBX) does not significantly alter AP velocity, indicating a non-synaptic mechanism. Two-tailed Mann-Whitney test (*n* = 100 APs per condition). **c**, AP propagation speed varies based on axonal arrangement: conduction is significantly slower in bundled axon segments compared to isolated axons. Kruskal-Wallis test (Individual: *n* = 29 APs; Bundled 0–400 µm: *n* = 50 APs; Bundled 400–800 µm: *n* = 50 APs). **d**, Over time, AP velocity increases in bundled axon regions in two example motifs as neurons naturally degenerate, reducing cell number. Kruskal-Wallis with Dunn's multiple comparisons test (Left: n = 20, 20, 20, 19, 19, and 20 APs at 14–61 dpi; Right: n = 20, 20, 22, 20, and 19 APs at 24–49 dpi) **e**, A

representative motif shows that AP velocity is high at 14 dpi when axons are dispersed. At 31 dpi, axon bundling slows conduction. Following cell loss, velocity rises again. (Kruskal-Wallis with Dunn's multiple comparisons test, *n* = 10 APs per condition.) **f**, Spike-contrast captures synchronous activity in a network and significantly increases with neuron number in directional circuits. Kruskal-Wallis with Dunn's multiple comparisons test after outlier exclusion (ROUT method, Q = 1%; *n* = 7, 13, 23, 17 circuits for 1–4 neurons respectively). **g**, PR, a measure of activity dimensionality, decreases with neuron count. Lower PR suggests more coordinated network dynamics (Kruskal-Wallis with Dunn's multiple comparisons test, *n* = 9, 16, 26, 19 circuits for 1–4 neurons). **h**, The frequency of synchronized bursting events scales with the number of neurons (*n* = 48, 79, 52 circuits for 2–4 cells respectively). **i**, Burst rate increases with cell number and remains unaffected by excitatory or gap junction blockers (NBQX + AP5, CBX), further supporting a non-synaptic coupling mechanism (*n* = 11, 19, 12 circuits for 2–4 cells respectively). **j**, Representative raw traces recorded from bundled axon regions demonstrate strong synchronized activity. Box plots indicate interquartile range (25th–75th percentile) with median; whiskers span minimum to maximum. Statistical significance: ns = not significant, **p* ≤ 0.05, ***p* ≤ 0.01, ****p* ≤ 0.001, *****p* ≤ 0.0001. Scale bars, 200 µm. *Figure is part of a submission currently in press (publication will be covered under a CC-BY 4.0 license) (Striebel et al., 2025b). Original data and visualization generated by the author. The submission is based on a preprint (Striebel et al., 2025a) and involves the same co-authors.*

3.4.3 Stimulating SNAPs electrically and via optogenetics

One theoretical prediction of ephaptic coupling is a lowered threshold for neuronal activation within a circuit (Capllonch-Jcauan and Sepulveda, 2020), implying that electrical stimulation should evoke stronger responses as more neurons are engaged. Consistent with this, I observed that firing rates increased superlinearly with the number of interacting neurons under electrical stimulation (Figure 3-13a). This effect persisted even when excitatory synaptic transmission was pharmacologically blocked, suggesting a non-synaptic mechanism.

I also employed optogenetics to stimulate individual iNGN neurons expressing the light-sensitive channel fChRimson-EYFP (Mager et al., 2018), while monitoring their responses via non-invasive MEA recordings. Light pulses reliably triggered APs in single neurons. As a control of my previous observations on ephaptic coupling, I assessed AP conduction speed in neurons expressing the optogenetic tool and found it similar to that in spontaneously firing neurons, with no detectable slowing of AP propagation (Figure 3-13b).

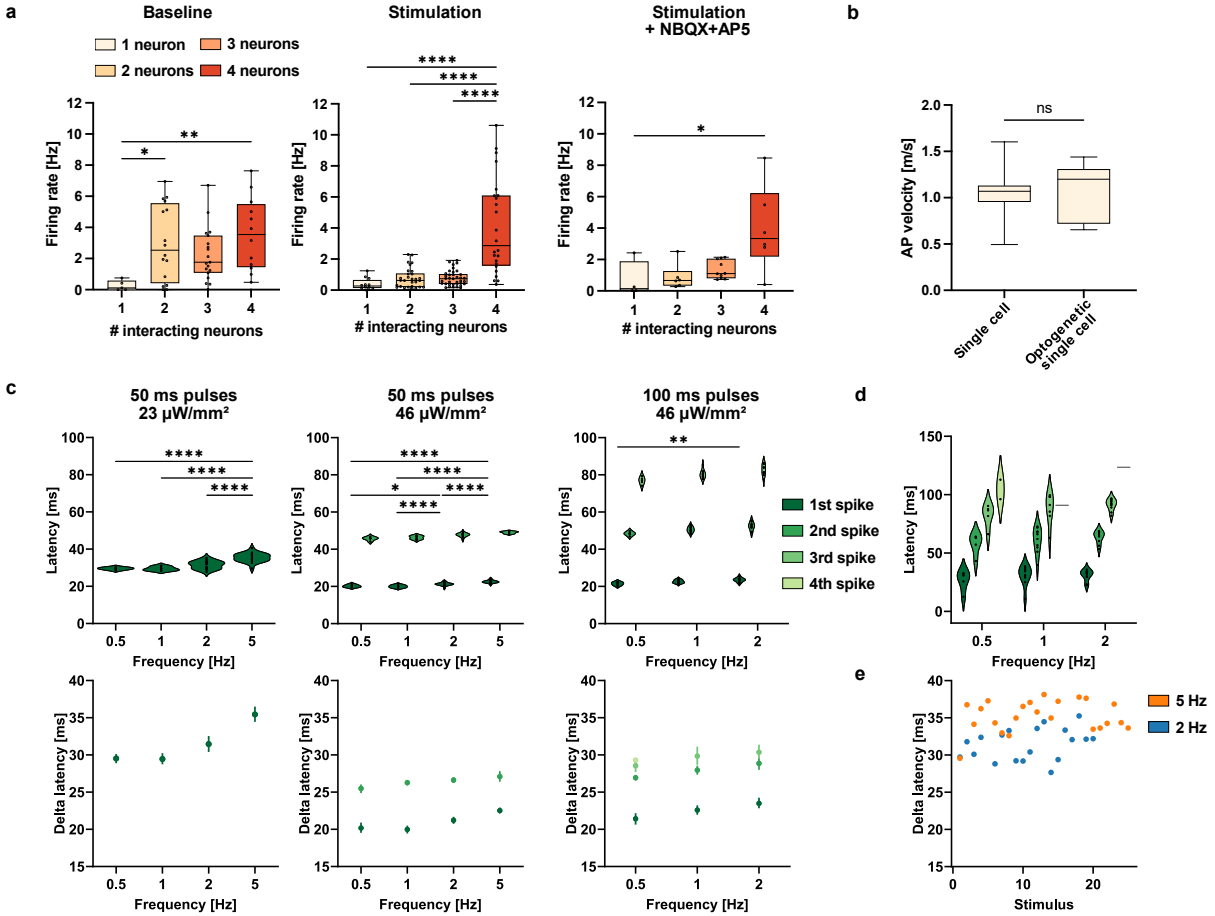

Figure 3-13: SNAP circuits respond to electrical and optogenetic stimulation. **a**, Mean firing rates in directional SNAP circuits increase superlinearly with neuron number during electrical stimulation. This effect is observed both in the presence and absence of excitatory synaptic blockers (NBQX + AP5), indicating that the response is not solely mediated by excitatory synaptic transmission. Kruskal-Wallis test with Dunn's multiple comparisons test after outlier removal (ROUT, Q = 1 %). Rates measured in electrodes of 16 circuits. Baseline: n = 5, 16, 19, 12; Stimulation: n = 12, 30, 37, 24; Stimulation + NBQX + AP5: n = 4, 6, 10, 6 for circuits with 1-4 neurons, respectively. **b**, AP conduction velocity in single iNGN neurons is comparable between spontaneous activity and optogenetically evoked responses. Two-tailed Mann-Whitney test (n = 60 spontaneous APs; n = 12 optogenetically evoked APs). **c**, A single fChRimson-expressing iNGN neuron shows increased AP generation in response to stronger or longer light pulses. Latencies, the time between light onset and AP peak, increase with stimulation frequency. Statistical tests for all 1st APs at different frequencies: normality confirmed by Shapiro-Wilk and Kolmogorov-Smirnov (alpha = 0.05); one-way ANOVA with Tukey's post hoc comparisons (Left/middle: n = 5, 10, 20, 25; Right: n = 5, 10, 10 pulses). Mean ± 95 % confidence interval in bottom plots. **d**, Similar latency behavior is observed in another iNGN-fChRimson neuron for 100 ms pulses with 46 µW/mm². Lines represent 4th APs at 1 and 2 Hz (n = 5, 10, 10 pulses). **e**, Individual iNGN-fChRimson neuron responds to 2 Hz and 5 Hz light trains (50 ms pulses, 23 µW/mm²). At 2 Hz, AP latencies remain consistent across the stimulus train. At 5 Hz, latency increases after the first light pulse. Statistical significance is denoted as follows: ns = not significant, *$p \leq 0.05$, **$p \leq 0.01$, ****$p \leq 0.0001$.

Figure is part of a submission currently in press (publication will be covered under a CC-BY 4.0 license) (Striebel et al., 2025b). Original data and visualization generated by the author. The submission is based on a preprint (Striebel et al., 2025a) and involves the same co-authors.

Next, I delivered trains of light pulses with varying parameters, including intensity, duration, and frequency to isolated fChRimson-expressing iNGN neurons (Figure 3-13c). At low light intensity (23 µW/mm²) and 50 ms pulse duration, I typically observed a single AP per pulse. Doubling the irradiance (46 µW/mm²) under the same conditions consistently evoked two APs at stimulation frequencies up to 2 Hz. Extending the pulse duration to 100 ms resulted in three APs per stimulus. I also found that the latency between stimulus onset and AP peak was approximately 10 ms longer at lower irradiance levels. To quantify this further, I calculated delta latencies, the interval between successive AP peaks, under different conditions. At higher intensities (50 and 100 ms pulses), these latencies remained relatively stable, although they increased slightly with each successive spike. These findings were corroborated in a second iNGN neuron, which occasionally fired a fourth spike under high-intensity stimulation (Figure 3-13d). An additional trend emerged when stimulation frequency was increased: AP latencies became progressively longer. Closer examination of individual light pulses in high-frequency trains revealed that while the first pulse elicited an AP with consistent latency, subsequent spikes were progressively delayed (Figure 3-13e).

4. Discussion

4.1 Neuronal activity under altered gravity

The content of the following section has been published in Striebel et al. (2023) under a CC-BY 4.0 license. I am a first author on this publication and my own contribution to the work involved experimental planning, sample preparation, data acquisition, data analysis, preparation of the figures and writing, as is stated within the publication. This was a collaboration project with other scientists contributing to experimental planning, data acquisition, and writing.

Astronauts exposed to microgravity environments often experience neurological symptoms, yet investigations into the cellular and network-level effects of altered gravity on neuronal systems remain scarce due to the difficulty to study these phenomena and the lack of appropriate models. Only a few studies have addressed this topic to date (Meissner and Hanke, 2002, Pani et al., 2013, Sieber et al., 2014, Genchi et al., 2015, Hauslage et al., 2016, Kohn et al., 2017, Cui et al., 2018, Kohn and Hauslage, 2019). A deeper understanding of how gravity influences brain function requires mechanistic studies to focus on key neuronal processes, such as electrophysiological activity. Neuronal activity changes reflect both structural changes in morphology and alterations in biochemical signaling pathways, particularly those involved in synaptic function. Of the various available techniques, MEA recordings are a well-suited method for electrophysiological investigations, and even under extreme physical conditions (see section 1.1). This makes the technology useful to research in gravitational biology, which frequently relies on large-scale, technologically complex, and resource-intensive platforms. Not only are these specialized facilities limited in availability, they also impose substantial mechanical and environmental stress on both experimental hardware and biological samples.

This study proves the feasibility of conducting electrophysiological recordings from human neural networks under altered gravity conditions using an MEA-based platform. These conditions present challenges not only to the viability of the cultured neurons, but also to the stability of the recording hardware. Our experimental setup incorporated a sealed pressure chamber, environmental sensors, and a heating system for temperature control,

as well as the MEA recording unit, in order to maintain ideal physiological conditions throughout the experiment (Supplementary Figure 1). This setup enabled us to sustain neuronal viability and consistent activity for extended recording sessions of at least 3 h. All support electronics, including temperature regulation systems, data acquisition computers, and redundant data storage, were located outside the pressure chamber to enable remote and autonomous operation. Importantly, the system is designed to be modular and adaptable, allowing it to be deployed in other altered gravity environments such as sounding rockets or parabolic flight missions. Beyond neuronal networks, the platform is also compatible with other excitable cell types including cardiomyocytes, acute brain slices, and brain organoids. Future integration of HD-MEA technology would further enhance the system’s capability to resolve fine-scale network dynamics in complex biological preparations.

Throughout both the centrifuge and drop tower campaigns, our experimental setup successfully maintained the stable environmental conditions required for long-term neuronal viability, including temperature, pressure, and CO_2 concentration (Supplementary Figure 1). No morphological alterations were observed in the networks, confirming the stability of neuronal networks and indicating viability of cells exposed to altered gravity in such experimental conditions. The MEA module and associated hardware withstood the mechanical stresses encountered during these campaigns, including high *g*-forces. This demonstrates the robustness and suitability of the system for gravity research, which pose many technological constraints to the experiment.

Implementing the experimental module on the SAHC validated the system's capability for real-time electrophysiological recording under hypergravity conditions (Figure 3-1). Notably, the neuronal networks responded rapidly to changes in gravity, as reflected in significant alterations in firing and burst rates. These responses were reversible, with no observable differences between pre- and post-exposure baseline recordings, indicating that the networks fully recovered after each gravity manipulation. This might point to a reversibility of phenotypes after short-term exposure. This is in line with observations in astronauts, where recovery of several parameters was found after a period back on Earth (Seidler et al., 2024). Nevertheless, longer exposure times might lead to more lasting effects and potentially neurodegeneration. Importantly, the neurons exhibited different

responses depending on the type of the gravitational loading. Acceleration and deceleration during the ramp phases consistently led to increased neuronal activity. In contrast, sustained hypergravity at 6 *g* produced a pronounced decrease in firing and burst rates (Figure 3-1). The heightened activity during the ramp phases is likely due to the mechanical forces acting on the system. This finding is consistent with prior research indicating that neurons are mechanosensitive, which further supports our claims and suitability of our experimental approach. Mechanosensitive ion channels can be activated by mechanical strain and are known to induce APs in neurons (Nikolaev et al., 2015). Their role in modulating neuronal excitability is well established (Kamkim and Kiseleva, 2008). Previous calcium imaging studies using SH-SY5Y cells in parabolic flight have supported this idea by demonstrating increased intracellular calcium levels under hypergravity and slight decreases during microgravity (Kohn, 2013). These results are consistent with the mechanosensitivity of calcium channels. Mechanically gated ion channels have also been proposed as key elements in the cellular detection of gravitational forces (Häder et al., 2017).

The sustained suppression of neuronal activity observed during the constant 6 *g* hypergravity phase likely reflects an additional cellular mechanism beyond the initial mechanosensory activation. One plausible explanation is that neurons compensate for the earlier increase in excitability during ramp acceleration. Prolonged hyperactivity may lead to neurotransmitter receptor desensitization or homeostatic downregulation, resulting in decreased activity during sustained load. A mechanism potentially underlying this observation is receptor internalization as occurring during LTD (Fang et al., 2015; de León-López et al., 2025). This adaptive response could account for the return to baseline activity levels observed during the late hypergravity phase and after the experiment ended. These findings suggest dynamic gravitational transitions, rather than static gravitational levels, have the most immediate and pronounced effects on neuronal network activity. While acceleration and deceleration phases stimulate neural activity acutely, a suppressive effect of continuous high *g*-load becomes evident only after reaching steady exposure. Interestingly, this inhibitory effect was reversible; within five minutes of sustained hypergravity, firing and burst rates returned to baseline. After deceleration, firing rates readapted within one minute, while burst rates required approximately five minutes to normalize. Changes in firing frequencies under altered

gravity conditions appeared to occur in a subgroup-specific manner within the neuronal network. The most prominent increase in activity occurred in low-firing neurons (~2 Hz), though neurons with intermediate baseline frequencies (6-9 Hz) exhibited enhanced firing as well. These findings suggest that gravity-related modulation may selectively affect distinct neuronal subtypes that remain to be fully characterized.

One hypothesis that could explain the observed decrease in firing under constant hypergravity is that increased gravitational forces alter membrane fluidity, thereby affecting ion channel function (Kohn et al., 2017). Nevertheless, our data indicate that neurons can adapt to these changes within a short timeframe of typically a few minutes, supporting the idea of dynamic compensation. Notably, experiments conducted at 4 *g* did not produce statistically significant changes in firing or burst rates, though the overall trend was consistent with that observed at 6 *g* (Supplementary Figure 3). These results imply that there is a gravitational threshold above which significant effects on neuronal excitability emerge. Alternatively, 4 *g* may be insufficient to induce measurable responses, at least in the timeframes applied in this study.

We also observed significant alterations in AP amplitude and half-width during hypergravity exposure, both compared to baseline levels before and after altered gravity (Supplementary Figure 4). These changes likely reflect shifts in ion channel kinetics due to modifications in membrane properties (Kohn and Ritzmann, 2018). However, it is questionable if a change in the mean AP amplitude from 30.52 µV to 30.76 µV has any relevance for the overall system, despite being statistically significant. Additionally, significant differences between baseline recordings taken before and after hypergravity exposure imply that readaptation processes may extend beyond the observation window. Future studies should extend the recording duration to more accurately capture these delayed effects.

Additional evidence of gravity sensing by neuronal networks came from our drop tower experiment. During the 4.7 s microgravity phase, we observed a significant increase in firing rates compared to baseline (Figure 3-2). This finding contrasts with the opposite trend of initially suppressed activity as observed during sustained hypergravity. This further indicates that neurons respond dynamically to changes in gravity. Both firing and burst rates were elevated during microgravity, supporting this conclusion. It has to be

pointed out though that the observation period in the initial hypergravity case was much longer (60 s). Extended microgravity exposure will be necessary to check for long-term adaptation processes. These conditions are difficult to create on Earth and would need to be investigated on sounding rockets, parabolic flights or on space stations.

Consistent with our findings from hypergravity exposure on the centrifuge, the impact of the drop capsule, which generated a brief peak of ~30 *g*, produced a sharp, transient increase in activity. This finding reinforces the idea that acute acceleration triggers mechanosensitive responses in neurons. Since such forces resemble those experienced during traumatic brain injury, our data suggest that high-*g* stimuli could serve as a model for studying mechanical trauma in neural systems. Post-impact recovery was rapid, with firing rates returning to baseline within 10 min (Supplementary Figure 5). These findings could suggest that networks possess a degree of resilience in these conditions. The gentle release mechanism in the drop tower enabled a smooth transition to microgravity, allowing for an instant shift from 1 *g* to microgravity with minimal mechanical interference. However, we did not observe an overshoot in firing rates that would support our earlier hypothesis of post-acceleration overcompensation. This suggests that the observed increase in firing rates during microgravity may be due to mechanical cues from the transition to force-free conditions or to intrinsic cellular mechanisms that respond to the absence of gravity directly. We have to point out again the difference in exposure length that could be a factor in eliciting compensation mechanisms.

Further analysis showed that different neuronal subpopulations responded differently to mechanical loading, indicating complex adaptations within the neural network. Closer inspection of single unit responses revealed that low-activity units firing at frequencies under 5 Hz in baseline increased their firing frequency in microgravity conditions. Meanwhile, high-activity neurons exhibited heterogeneous responses: roughly half increased and half decreased their firing rates, spanning frequencies from 15 to 28 Hz. Following capsule impact, neuronal activity increased again, particularly at 8 and 20 Hz, which is consistent with centrifuge-derived acceleration responses (Figure 3-1). These differential responses among subpopulations, which was also observed under hypergravity, support the hypothesis that individual neurons either directly sense gravitational changes or respond indirectly through altered network dynamics. Future

experiments are needed to determine whether gravity acts primarily at the level of individual neurons or modulates global network behavior.

Taken together, these data reveal that human neural networks are highly responsive to gravitational fluctuations, with distinct temporal dynamics governing excitation and adaptation. Our findings underscore the importance of considering both acute and sustained mechanical forces when evaluating neuronal function under altered gravity conditions. A more detailed investigation of the effects of acute mechanical stimulation during acceleration phases is essential. For microgravity research in particular, extended exposure times are likely required to reveal long-term adaptive processes. Differences in the temporal dynamics of re-adaptation for firing versus burst rates following hypergravity and acceleration suggest the involvement of distinct regulatory pathways.

To fully understand the mechanisms underlying gravity-induced modulation of neuronal activity, future studies must focus on identifying the specific neuronal subpopulations responsible for the observed changes. Further investigation is required to elucidate the mechanisms underlying gravity-dependent modulation of neuronal transmission, particularly among distinct neuronal subtypes within the network. More detailed analysis of specific neuronal subgroups is necessary, since our results suggest a non-uniform response of neuronal populations. Prolonged exposure to both hypergravity and microgravity could help test the hypothesis that neurons undergo adaptive responses following acute mechanical stress. Sounding rockets would be a suitable platform for such experiments. Similarly, repeated ramp-phase exposures, such as those experienced during parabolic flights, could reveal whether the enhanced activity observed during acceleration is cumulative or if neurons become habituated. Specifically, these experiments could reveal whether neural responses diminish or amplify with repeated exposure due to additive mechanosensory stimulation.

To address all these questions, further experiments should utilize a variety of gravity research platforms, such as the GraviTower Bremen Pro for repeated and tunable accelerations, parabolic flights that alternate between hyper- and microgravity (~22 s per phase), and sounding rocket missions providing intermediate-duration (5–6 min) microgravity exposure. Examining how various neuronal cell types respond to gravitational stimuli will also be important, as intrinsic biophysical differences may lead to divergent

response profiles. Electrophysiological parameters such as AP amplitude and half-width, should continue to be monitored for gravity-dependent alterations. Additionally, neuronal maturation may influence responses to altered gravity. Therefore, networks of varying culture ages should be included in future analyses. To uncover the molecular basis of the observed effects, studies involving ion channel knockout models or targeted pharmacological inhibition of candidate pathways are necessary. Transcriptomic profiling could provide further insight into gene regulatory changes associated with gravity-induced neuronal plasticity. Transitioning from *in vitro* models to *ex vivo* systems, such as brain slice cultures, may also enhance the physiological relevance of the research.

Although long-term adaptation studies are restricted to space-based platforms such as satellites or the ISS, ground-based simulations are still crucial and have the advantage easier accessibility and lower costs. Hypergravity can be reliably generated via centrifugation using a device like the MuSIC incubator-centrifuge at the German Aerospace Center (Frett et al., 2016; Lichterfeld et al., 2022), and microgravity can be simulated using a fast-rotating 2D clinostat that counteracts the Earth's gravity vector (Hemmersbach et al., 2006). Further research is needed to determine whether changes in membrane fluidity contribute to the observed alterations in neural activity (Kohn et al., 2017; Sieber et al., 2014). Dissecting the contributions of specific receptor potentials and neuronal subtypes will require pharmacological interventions, such as the use of receptor-specific antagonists. Most experiments to date have focused on spontaneous activity. Future studies should investigate evoked potentials and neuronal responses to acute stimuli under altered gravity conditions. Understanding these mechanisms may reveal targets for countermeasures to mitigate the negative effects of space environments on brain function. Such interventions would be valuable for both long-term human spaceflight and treating neurological disorders on Earth involving altered neuronal dynamics with similar causes.

In summary, we demonstrate that our human neural network model is sensitive to short-term alterations in gravitational forces. The immediate electrophysiological responses to these changes, as observed through MEA recordings, validate the usefulness of this *in vitro* platform in the study of gravitational biology. MEA technology is a robust and reliable method for monitoring neuronal function under extreme environmental conditions. Our

findings highlight the importance of further investigating how gravitational forces influence brain physiology and neural circuit function. We generated an extensive dataset of electrophysiological recordings from hiPSC-derived neuronal networks exposed to altered gravity conditions. To enable these investigations, we developed a dedicated experimental module that can sustain neuronal cultures and record their activity with millisecond resolution in various environments. Successful validation of the system in the drop tower and on the SAHC demonstrates its robustness and adaptability. These capabilities lay the groundwork for more advanced future studies under extreme environmental conditions and on space-relevant platforms. Our findings demonstrate that changes in gravity immediately affect the electrical activity of human neurons. Specifically, microgravity led to increased neuronal activity, whereas hypergravity resulted in reduced firing and bursting. These observations align with limited prior reports in other cellular models. However, the differential responses suggest that distinct neuronal subpopulations may react uniquely to gravitational shifts or that complex, network-level adaptations are involved.

4.2 Morphological and functional long-term development of 2D neuronal networks *in vitro*

The content of the following section has been published in Habibey et al. (2022b) on which I am a first author under a CC-BY 4.0 license. My own contribution to the work involved data collection, analysis and visualization as well as writing. This was a collaboration project with other scientists contributing to all parts of the work.

As shown in the previous chapter, MEA technology provides a versatile research platform. Reliable *in vitro* models of brain development derived from hiPSCs require the formation of functional neuronal networks that are maturing reliably (McCready et al., 2022). Further, the ability to observe network dynamics and morphology with high spatial and temporal resolution, ideally at the single-cell level, is necessary (Diggelmann et al., 2018; Dragas et al., 2017; Ronchi et al., 2021; Yuan et al., 2020). Long-term culture viability is important for capturing the progressive structural and functional maturation of these networks over extended periods (Saalfrank et al., 2015). Since previous works have been limited by short observation periods (< 1 month) (Akarca et al., 2022; Ronchi et al., 2021) or low-density

MEAs with limited spatial resolution (Hyvärinen et al., 2019; Lu et al., 2019; Odawara et al., 2014, 2016b; Schmieder et al., 2022) we wanted to overcome these limitations.

In this study, we used HD-MEAs and a refined long-term culturing protocol (Klapper et al., 2017; Sauter et al., 2019; Schmieder et al., 2022) to monitor the morphological and functional development of hiPSC-derived neuronal networks over three months. To enhance synaptic maturation, network performance, and survival, the cultures were supplemented continuously with astrocyte-conditioned medium (Klapper et al., 2017; Taga et al., 2019). HD-MEA-based long-term recordings in hiPSC-derived networks have rarely been explored to date. One such study reported AP frequency changes mainly in the context of electrical stimulation (Amin et al., 2016). In a previous study by our lab, we used conventional MEAs with 60 electrodes to investigate long-term network formation (Schmieder et al., 2022). Microscopy revealed significant alterations in network organization over time. Cellular movement on low-density electrode arrays limits the ability to maintain high-quality recordings as neurons shift away from electrode sites. We addressed this limitation by employing HD-MEAs, which provide much finer spatial resolution and broader coverage of the culture surface. The results presented here (section 3.2) confirmed that HD-MEAs enable tracking of shifts in neuronal positions and network architecture over time (Figure 3-3). To ensure accurate longitudinal data, we conducted full-chip activity scans prior to each recording session. This strategy enabled us to map active regions and revisit the same neurons and clusters at different time points. Although HD-MEAs greatly improve resolution with their 26,400 electrodes available here, the used system has one limitation: only 1,024 electrodes can be recorded simultaneously, which necessitates long scanning times to capture whole-network dynamics.

As the brain develops, its structural complexity increases to accommodate efficient local and long-range neuronal communication (Casanova and Casanova, 2019; Wang and Clandinin, 2016). The demand for wiring efficiency often results in modular, clustered network architectures where functionally linked neurons are physically proximate to reduce connection costs (Bassett and Bullmore, 2006; Casanova and Casanova, 2019; Wang and Clandinin, 2016). Classic examples include cortical folding and gyri formation, which bring distant brain regions into close proximity (Chavoshnejad et al., 2021; Wang

and Clandinin, 2016), and the segregation of gray and white matter to enable efficient signal relay via long-range axons (Martinez and Sprecher, 2020; Richards and Van Hooser, 2018).

In our long-term cultures, we observed neurons gradually self-organizing into small aggregates beginning in the second month, which then coalesced into larger clusters in the third month (Figure 3-3). Axonal bundles linked these structures, resembling the early topological organization of the human brain. Similar findings have been reported in studies where cortical neurons cultured in clustered arrangements exhibited increased bursting activity and stronger functional connectivity than neurons distributed homogeneously (Tibau et al., 2020). Similarly, artificially patterned modular circuits in microfluidic systems have demonstrated enhanced activity and more robust signaling properties (Habibey et al., 2024; Levy et al., 2012; Marconi et al., 2012; Nam et al., 2004; Park et al., 2021; Yamamoto et al., 2018). Our observations suggest that the shift from dispersed to clustered morphologies is an intrinsic developmental behavior of neurons. This behavior is driven by their tendency to self-organize into functionally coherent modules and form long-range projections through axon bundling. This clustering occurred despite the surface treatment of the MEAs, which was intended to promote stable adherence, thereby highlighting active neuronal migration as a driving force. This phenomenon might be driven by chemotaxis and mechanical forces as well as neuronal developmental programs. Similar phenomena have been documented in other *in vitro* neuronal cultures (Antonello et al., 2022; Segev et al., 2003; Tibau et al., 2020).

Electrophysiological data were continuously collected from long-term cultures to monitor the development of network function. Upon doxycycline induction, iNGN cells consistently differentiate into neurons with high efficiency, as evidenced by FOXG1 and MAP2 immunostaining and RT-qPCR analyses (Lu et al., 2019). We regularly assessed the health and progression of cultures through microscopy. We used spike sorting to isolate the activity of individual neurons during each recording session. Over time, the iNGN-EGFP-derived networks exhibited clear developmental transitions in activity patterns. During the first month, firing was sparse and isolated. By the second month, localized bursts had emerged. By the third month, coordinated, synchronized, network-wide bursts became prominent (Figure 3-4). Burst dynamics evolved in distinct ways across this

developmental trajectory. On the one hand the frequency of bursts steadily increased, but their duration reached its maximum in the second month and declined thereafter. The proportion of spikes occurring within bursts remained elevated, reaching a maximum around 69 dpi. This progression aligns with prior studies identifying spontaneous and synchronized network bursting as hallmark features of developing neocortical circuits *in vivo* (prenatal and postnatal) and *in vitro* (Khazipov and Luhmann, 2006; Kilb et al., 2011; Luhmann et al., 2016). Burst events are believed to play a vital role in circuit refinement by promoting synaptic maturation and enhancing neuron-to-neuron communication. This is because bursts can reliably activate postsynaptic partners, even across weak synapses (Zeldenrust et al., 2018). Together this highlights the potential of these systems to capture key aspects of neural circuit maturation *in vitro*.

To investigate the contribution of excitatory synaptic activity to burst formation further, we pharmacologically inhibited glutamatergic transmission. Following treatment with NBQX and AP5, synchronized bursting ceased, and fewer neurons remained active. However, baseline-like tonic firing persisted, indicating that individual neuronal activity continued despite disrupted synaptic transmission. These results suggest that excitatory synapses primarily mediate coordinated bursting in iNGN cultures (Figure 3-6).

Although glutamatergic signaling emerges early in brain development, GABAergic connections typically mature more slowly (Bagasrawala et al., 2017; Warm et al., 2022). The deferred development of GABAergic synapses coincides with the onset of strong burst activity in the mammalian brain, particularly during the postnatal period (Khazipov and Luhmann, 2006; Luhmann et al., 2016; Luhmann and Khazipov, 2018). It has been reported that iNGN cultures develop GABAergic neurons over time with 2.3 % present by 30 dpi (Lu et al., 2019). Firing and bursting activity was shown to increase after blocking GABA receptors with picrotoxin. These results suggest that GABAergic signaling acts to regulate both the intensity and structure of burst activity in maturing iNGN-derived networks. Blocking inhibitory input increases firing and bursting frequency while simultaneously shortening bursts and reducing their spike content, confirming the modulatory role of GABA-A receptors in network homeostasis. This is consistent with a shift from excitatory to inhibitory GABAergic signaling in early brain development. The GABA switch, has also been observed in hiPSC-derived organoids around day 40

(Zafeiriou et al., 2020). In our study, inhibition of GABA-A receptors at advanced culturing times (120 dpi) led to a pronounced increase in spike and burst frequency, suggesting that, by this time, GABAergic transmission had adopted its mature inhibitory role (Figure 3-7).

A significant component of inhibitory modulation in the cortex is attributed to fast-spiking GABAergic interneurons, which play a key role in regulating excitatory output (Galarreta and Hestrin, 2002). These neurons are identified by their ability to generate rapid spike trains in response to depolarization (Damodaran et al., 2014). Across multiple species, including humans, monkeys, and rodents, these cells can achieve firing rates exceeding 150 Hz (Wang et al., 2016). In our experiments, we identified a subset of neurons capable of this high-frequency firing. The proportion of fast-spiking units increased significantly after 63 dpi coinciding with an increase in synchronized bursting (Figure 3-5). These results support the conclusion that the maturation of inhibitory GABAergic circuits plays a regulatory role in shaping network-level burst dynamics. This finding is consistent with previous studies on postnatal brain development showing that GABAergic activity modulates spontaneous and sensory-driven bursts (Bonifazi et al., 2009; Butt et al., 2017; Warm et al., 2022). Further, this timepoint coincides with the observed development and specification of interneurons in human embryonic development (Yu et al., 2021; Zecevic et al., 2011). This indicates that similar developmental genomic programs might be at play in our model system. For a better understanding of this process future studies should look at gene expression changes that might help to correlate these findings.

In line with our results, modifying the ratio of inhibitory to excitatory neurons has been shown to influence the temporal structure and regularity of network bursting (Chen and Dzakpasu, 2010). The interplay between NMDA receptor-mediated excitation and GABAergic inhibition is particularly crucial for establishing distinct patterns of synchronized activity (Teppola et al., 2019). Our data reflect this balance, underscoring the role of inhibitory transmission in organizing spontaneous network bursts. Given the sensitivity of network activity to GABAergic modulation, changes in cell composition and identity likely occur over time. Whether these cellular dynamics are related to the observed structural clustering remains to be investigated.

Our long-term recording findings underscore the necessity of continuous monitoring to fully capture hiPSC-derived network maturation. HD-MEA data clearly illustrate ongoing shifts in the spatial arrangement of neurons and clusters over three months, including migration and axon bundling. These features echo morphological changes observed in the developing cortex. Evolving structural characteristics must be considered when designing experiments, especially those focused on functional connectivity. Changes in spatial topology directly influence connectivity measures and should not be assumed to remain constant. Our findings suggest that evolving network architecture can substantially influence the interpretation of functional readouts. They further reveal that spontaneous, synchronized network activity progressively mirrors *in vivo* developmental processes during pre- and postnatal stages. The high variability in burst metrics during network development highlights the limitations of short-term studies and the risks of inferring functional phenotypes from isolated time points. This issue is even more critical when comparing healthy and diseased models, as developmental trajectories may differ. Further research is necessary to determine how closely *in vitro* maturation mimics *in vivo* processes, especially regarding the co-evolution of morphology and cell identity.

Finally, our study shows that iNGN-derived networks reach functionally mature activity profiles in about three months. These profiles are characterized by stable, spontaneous activity. Despite continued morphological reorganization, HD-MEAs offer the spatial and temporal resolution necessary to track individual neurons and maintain consistent, longitudinal recordings. This high resolution improves data quality, thereby increasing the efficiency of experiments using human stem cell-derived neural systems.

4.3 *In vitro* plasticity and learning experiment

Based on the previously described observation of pronounced morphological changes of *in vitro* networks over time (see sections 3.2.1 and 4.2), my goal in this experiment was to test whether a microfluidic MEA platform, that constrains neuronal growth into a feedforward-like architecture, could elicit measurable plasticity and task-related learning. By designing a multilayer circuit and delivering patterned, temporally ordered stimulation, I sought to construct a simple spatial classification task. I then asked whether correlations between defined input and output layers would strengthen with training.

Despite clear experimental control over network geometry and stimulation patterns (Figure 3-8a), I found only subtle, non-significant changes in global and pairwise activity measures. The PR, a metric of dimensionality of the activity, declined slightly with culture age but did not show significant differences. The observed trend is in line with previous observations of an increased synchronous activity with culture age (see 3.2.2 and 4.2). Interestingly, I observed the PR during stimulation sessions to be slightly lower in the earlier days. A possible explanation for this is that younger and less matured networks in which the synaptic connections are not yet fully tuned to the usually observed synchronized bursting activity (Maeda et al., 1995), are more susceptible to stimuli and thus easier to drive, leading to a more uniform and thus lower-dimensional activity under stimulation.

Likewise, average correlation coefficients between input and output electrodes showed only weak upward trends over time. The overall strength of the correlation remained low. Looking at the intended generation of a more correlated activity between input and output populations of the respective stimulation patterns (the “true input–true output” condition) remained lower than several control pairings, which were not stimulated synchronously. Together, these observations indicate that the cultures did not develop robust, stimulus-specific coupling between the trained input–output pairs under the conditions tested. Thus, likely no LTP was induced. Interestingly, after the switch from tetanic stimulation to theta burst stimulation beginning at 34 dpi, I saw an upward trend in all conditions. This could either be caused by TBS or could coincide with a developmental maturation step and subsequent increase in correlated activity, which we also observed to occur around 42 dpi in our previous long-term culture experiment (see section 3.2.2).

These results contrast with earlier reports of induced plasticity and closed-loop control in dissociated cultures (e.g., Chiappalone et al., 2008; DeMarse et al., 2001). Several factors may explain the difference. First, the system imposed a fixed feedforward geometry, which limits the recurrent connectivity thought to support associative learning. Second, iNGN-EGFP cultures may require different neuromodulatory cues to express forms of Hebbian plasticity such as LTP and LTD. Third, the stimulation protocol, although timed to mimic spike timing-dependent plasticity, may not have provided sufficient intensity, duration, or reinforcement signals to drive lasting synaptic changes. Moreover, the electrical

stimulation has the drawback of spreading through the culture media as opposed to more targeted optogenetic stimulation, potentially leading to off-target effects. Fourth, I did observe synchronized bursting in the cultures, which is thought to counteract learning in *in vitro* systems, since it could erase or override the effect of the external stimuli (Wagenaar et al., 2006).

One motivation for using microfluidics was to stabilize network morphology and reduce the confounds of spontaneous changes in morphology reported in self-organized cultures (Habibey et al., 2022b). The data suggest that, while physical constraints can maintain gross topology, they do not guarantee the emergence of functional learning. Structural stability may even limit the flexible rewiring that enables natural networks to form new associations. Future designs might balance structural guidance with opportunities for recurrent connections and spontaneous reorganization.

Limitations of the present study that could be addressed in future experiments are a more precise stimulation through optogenetic methods, that limits potential off-target activations. Additionally, the possibility to optogenetically activate the cultures might offer a route for easier and truly continuous stimulation of the cultures, a feature that could mimic sensory input to the circuits and potentially decrease synchronous bursting. Incorporating chemical modulators (e.g., dopamine or acetylcholine), longer training periods, or richer sensory feedback could also enhance plasticity. Finally, integrating the experiment on HD-MEAs or adding calcium imaging may provide more detailed insight into structure-functional relationships during learning.

This study demonstrates the feasibility of constructing stable, feedforward-like microcircuits on MEAs and applying a structured training paradigm. However, under the present conditions, these engineered networks did not exhibit robust, task-specific increases in correlated activity as a sign of LTP. Rather than a definitive failure of *in vitro* learning, this outcome underscores the complexity of replicating biological learning rules in simplified systems. Continued exploration of network architecture, maturation state, and stimulation strategies will be essential for realizing the potential of microphysiological cultures as platforms for studying plasticity and as living substrates for computation.

4.4 Engineered neuronal circuits with single-cell precision allow dissection of neuronal interactions

Content of the following section is currently in press (Striebel et al., 2025b) and is partly published as a preprint under a CC-BY-NC-ND 4.0 license (Striebel et al., 2025a). The research was led by me. All experiments, data collection and analysis as well as writing and figure preparation were carried out by me.

As described previously, bottom-up construction of circuits with single-cell precision might be a useful tool for precise investigation of subtle neuronal interactions, like under ephaptic coupling. To construct SNAPs, I employed microfluidic devices as structural templates that guide the growth and connectivity of human neurons in a defined pattern. This strategy is widely recognized in the field of neural circuit engineering (Habibey et al., 2022a) and offers several benefits. Firstly, microfluidic platforms are highly compatible with MEAs, allowing stable and long-term electrophysiological monitoring. Secondly, cultured neural networks typically undergo notable morphological changes over time (Habibey et al., 2022b), but the microfluidic design helps preserve the original circuit architecture and keeps neuronal processes close to the recording sites. Thirdly, the confined microenvironment provided by microfluidic channels protects the cells from physical disturbances, such as those introduced during media exchange or recordings, thus improving circuit stability. In contrast, other patterning techniques such as microcontact printing often result in less predictable growth patterns and reduced structural integrity over time (Habibey et al., 2024).

I used hiPSC-derived neurons to construct circuits (Busskamp et al., 2014). Human cells are particularly suited for biomedical research because of their clinical relevance. They provide a scalable alternative to some traditional animal models, helping to bridge the translational gap between laboratory findings and human applications. Most approaches that reported the fabrication of *in vitro* neuronal circuits in microscaffolds so far used an unguided random seeding. Cell suspension is added to the substrates and cells settle down in the open microwells. This method does not guarantee the placement of a single cell in each microwell. While this approach has the potential for rapid parallel fabrication of multiple circuits (Amos et al., 2025), it becomes limited when precise placement of different cell types or neuronal subtypes is required. Generating complex and reproducible

circuits composed of a larger number of neurons using this method is challenging. Fluidic force microscopy has previously been employed to achieve high-precision cell placement (Connolly et al., 2024; Dörig et al., 2010). However, a major challenge has remained the post-placement survival of individual neurons, which is critical for forming fully functional circuits (Girardin et al., 2022).

To achieve precise control over cell positioning, critical for constructing defined circuits and reproducibly mixing different cell types, I adapted a technique inspired by blastocyst injection (Figure 2-3; Figure 3-9; Supplementary Figure 6). This method, commonly used in establishment of transgenic mouse models, involves manually injecting individual stem cells with a micropipette. I developed a custom setup consisting of a microscope-mounted micromanipulator, a glass micropipette, and a pressure-controlled microinjector (Figure 2-3b). It was key to match the pipette opening to the size of the cells for an efficient transfer. This setup further has the potential to be fully motorized which would make automated seeding of cells possible, potentially leading to faster and parallelized manufacture of SNAP circuits for high-throughput production.

In order to be able to assemble many circuits in parallel on MEAs, two features were critical. First, I tried to design the structures and assemblies thereof to fit as many circuits as possible on a single MEA. Second, I developed a rapid and scalable method for fabricating microscaffolds in PDMS. A decreased turnover time for circuit manufacturing and testing also aids in the development and optimization of *in vitro* neuronal systems. Direct laser writing was employed to make master structures. DLW is a method that allows rapid prototyping, ideal for small numbers of custom designs, by offering high design flexibility and avoiding the use of photomasks. Classical photolithography manufacturing processes rely on these masks, making the process more cost and time intensive. To parallelize the microscaffold fabrication, I subjected the direct laser written masters to a soft lithography process for fabrication of many identical stencils. Preparation of functional microscaffolds in PDMS from these stencils takes about 30 min.

In this study, I used two different circuit designs, a Y-shaped structure with three neurons and a unidirectional structure with four neurons. The unidirectional microfluidic layout was adapted from a previously reported stomach-shaped design that promotes unidirectional axon growth (Forró et al., 2018). The reservoir’s geometry encourages axons to extend in

the intended direction, while the size and arrangement of the microchannels impede reverse outgrowth. A small lateral channel further diverts any axons attempting to grow backward, steering them back onto the forward trajectory. To limit cross-well invasion, I added narrow sections and sharp turns at the point where three channels meet the stomach-like chamber. Cross-correlation of the electrophysiological recordings verified that activity propagated directionally through the device, confirming that the structure effectively guides axons (Supplementary Figure 7). Of note, when comparing the survival rates of the two structures, the circuits in the unidirectional structures show improved viability (Figure 3-10b,c; Figure 3-11c,d). This could be due to an improved microenvironment in these circuits as a result of the different geometry, providing more favorable conditions for neuronal survival. Another possibility is that the higher number of cells leads to improved conditions because a higher concentration of secreted biochemical factors. Finally, the confinement could facilitate the establishment of synapses in the circuits.

SNAP circuits of both designs responded to the addition of excitatory synaptic blockers, confirming functional synaptic connections (Figure 3-10; Figure 3-11). When comparing the effect of such excitatory synaptic antagonists on electrophysiological dynamics of SNAP circuits vs. populations of neurons, a significantly more pronounced response was observed. More specifically, the distribution of ISIs measured differed significantly. A reason why the activity profile shows a stronger response to synaptic intervention might be the smaller and more simple architecture of the SNAP circuits composed of a few neurons. Smaller networks have less degrees of freedom and thus network effects are less likely to have a strong influence in the measured dynamics. Background noise that could be generated by the activity of many neurons firing is less likely to occur and is thus less likely to mask changes in activity due to perturbations of the system. Similar conclusions were drawn by a recent preprint (Amos et al., 2025). There it was possible to extract fundamental biophysical parameters from the electrophysiological activity of neuronal pairs on MEAs, like axonal diameters or the average synaptic weight of AMPA/NMDA receptors. In small scale networks of a few neurons there are less variables in mathematical models that need to be fit. Thus, it is easier to fit them computationally to the data (Bellman, 1957). This enables a detailed comparison of computational modeling predictions with experimental results. Moreover, this can help in designing and validating

hypothesis-led experiments in which the circuits can be reproducibly created with a specific architecture and the activity can be compared to model predictions.

For example, using the SNAP system, I was able to design circuits in a way that effects of ephaptic coupling can be measured. Central to these results was the ability to construct precisely defined neural circuits in which individual neurons could be placed, monitored, and maintained over extended periods. This level of control allowed to bring axons of several single neurons in close contact so that ephaptic coupling can occur. I was able to isolate and study ephaptic effects in a purely endogenous setting, free from confounding chemical synaptic input, network effects or the need to use external electrical fields. I provide evidence that endogenous electric fields generated by small groups of neurons are sufficient to induce ephaptic coupling (Figure 3-12; Figure 3-13).

Ephaptic coupling is a phenomenon in neuronal networks, that cannot be blocked and is thus difficult to study *in vitro* and *in vivo*. Especially the functional implications of the phenomenon have been difficult to measure experimentally. Using this approach, I was able to experimentally verify theoretical predictions such as reduced AP conduction velocity, enhanced synchrony of firing, and a lowered threshold for activation (Capllonch-Juan and Sepulveda, 2020; Han et al., 2018; Katz and Schmitt, 1940; Schmidt and Knösche, 2019).

There have been a limited number of experimental studies, involving advanced techniques and external electric fields (Anastassiou et al., 2011; Blot and Barbour, 2014; Han et al., 2018, 2020; Katz and Schmitt, 1940). Many papers approached the effect by computational and theoretical modeling and made predictions for functional characteristics (Anastassiou et al., 2010; Capllonch-Juan and Sepulveda, 2020; Lin and Keener, 2013; Pinotsis and Miller, 2023; Rabinovitch et al., 2024; Schmidt et al., 2021; Schmidt and Knösche, 2019; Stacey et al., 2015; Wei and Tolkacheva, 2022). It is thought to play a role in the brain (Anastassiou et al., 2011; Pinotsis and Miller, 2023; Weiss and Faber, 2010), the olfactory system (Bokil et al., 2001), the retina (Kamermans et al., 2001; Vroman et al., 2013), and in cardiac conduction (Ivanovic and Kucera, 2021; Veeraraghavan et al., 2014), and being associated with diseases like epilepsy (Dudek et al., 1998; Shivacharan et al., 2021) and arrhythmia (Veeraraghavan et al., 2018, Hoagland

et al., 2019). and is thus a relevant effect that needs more experimental validation and investigation.

The precise adjustment of the neuron number in a circuit, as well as a reproducible design that enables axons to interact in specific regions, are ideal for modulating ephaptic coupling. The interaction of axons inside microfluidic channels might enhance or even amplify the effect, since diffusion of ions and thus equilibration of electric potentials is restricted. I observed direct functional signatures of ephaptic coupling. Most prominent was altered AP conduction velocity (Figure 3-12). This effect was reported previously and also predicted by computational studies. To the best of my knowledge, this is the first time a direct relation between the strength of ephaptic coupling and measured AP velocity is shown. The smaller decrease in AP velocity with an increasing number of neurons suggests a logarithmic or otherwise asymptotic relationship, leading to a decreased sensitivity to changes in ephaptic coupling at higher strengths and a more stable velocity. This view is supported by longitudinal observations of neuronal circuits over time, in which changes in the range from four to one participating neurons led to large increases in AP velocity (Figure 3-12d,e). Of note, adding excitatory synaptic antagonists NBQX + AP5 or gap junction blocker CBX to the cultures did not change the AP propagation velocity, suggesting that the measured effect is not connected to these forms of transmission. An increased synchronicity of firing patterns is another fingerprint of ephaptic coupling. By monitoring measures of synchronicity in SNAP circuits like spike-contrast, PR and bursting, I could observe a relationship between the neuron number and synchronicity features in the circuit (Figure 3-12f-j).

Variations in AP conduction speed within microchannels could, in principle, also stem from other factors like local shifts in ion concentrations that accumulate in the microchannels. In the present study, however, this explanation is improbable. Each channel contained only a few axons (< 4) with overall low firing frequencies (Figure 3-13a). If axons are approximated as 1 µm in diameter, they occupy roughly 2 % of the channel volume, leaving the remainder filled with culture medium that enables efficient diffusion. Consequently, the ionic changes generated by individual APs are negligible compared with the bulk ion content of the medium. Supporting this view, prior work demonstrated rapid ionic diffusion and fast dissipation of gradients in similar microfluidic systems

(Miyamoto et al., 2013). Additional evidence shows that even markedly higher activity from a greater number of axons and increased bursting does not appreciably slow conduction (Habibey et al., 2017). Future refinements of microfluidic designs could help isolate ephaptic effects more clearly from potential ionic influences while maintaining neuronal viability.

I also found indications for a lower activation threshold of neurons that are ephaptically coupled in a circuit, as predicted theoretically by Capllonch-Jcauan and Sepulveda (2020). I found that indeed with more neurons participating and thus stronger ephaptic interactions, the same electrical stimulus elicited significantly stronger responses, which could be the result of a lowered activation threshold. More specifically, I observed a superlinear increase in firing rates with the number of interacting neurons during electrical stimulation (Figure 3-13a). Notably, this effect remained even after pharmacological inhibition of excitatory synaptic transmission, pointing to a non-synaptic mechanism.

These findings provide experimental validation for long-standing theoretical and computational predictions about ephaptic interactions, and reinforce the idea that such coupling mechanisms may play a fundamental role in neural communication. The SNAP method provides an option to monitor these effects over time with high spatial and temporal resolution. The results presented here also highlight the critical influence of axonal spatial arrangement on the electrical behavior of neuronal networks. While the results demonstrate ephaptic coupling *in vitro*, its significance *in vivo* remains to be established. For example, in the retina ephaptic mechanisms in synaptic communication of specific cells are established (Kamermans et al., 2001; Vroman et al., 2013). Of note, retinal ganglion cells, which relay signals from the retina to the brain, are only myelinated when they start to form the optic nerve, but are unmyelinated in the retinal nerve fiber layer (Fitzgibbon and Nestorovski, 1997). This means that in the retinal fiber layer ephaptic coupling could also be at play. A recent paper looked at mechanisms of timing and synchronization in the retina (Bucci et al., 2025). Stimuli received at different locations of the retina have to be synchronized for further processing in the brain. Bucci et al. showed that differences in axonal length in the retina are compensated by adjusting axon diameter leading to changes in AP propagation speed and ultimately synchronized signaling. Median AP speed in the retina was reported to be around 0.5 m/s, close to the median

values of 0.63 m/s and 0.43 m/s measured in this study in the cases of multiple neurons and populations of neurons, respectively. This suggests that next to the synchronization due to anatomical adjustments in axons, ephaptic coupling could potentially also contribute to the synchronization of signals in the retina.

Furthermore, I could show that the SNAP method can be used to culture and measure single neurons and that these neurons can be stimulated when expressing optogenetic tools. Modulating light parameters enabled precise control over the number of evoked APs in the neurons. This likely reflects the proximity of the applied light intensity to the activation threshold of the opsin, causing a controlled increase of currents. Progressive ionic depletion may cause the observed increase in latency and reduction in spike number with higher stimulation frequencies and intensities.

Together, these results highlight the utility of SNAP-based circuits for high-precision stimulation, both electrically and optically, and recording. The combination of optogenetics and MEA recordings offers a non-invasive, physiologically relevant platform for probing optogenetic responses in a natural setting. Unlike patch clamp methods, this approach preserves native ionic dynamics and experiments can be observed over long time periods, which makes it possible to check developmental features. Since in SNAPs it is still possible to record from one cell only, typical parameters of optogenetic tools could potentially be extracted from or fitted to the measured data. Moreover, SNAPs would be well-suited for evaluating neuronal function, the performance of optogenetic tools, and the investigation of signal processing in engineered circuits with high precision.

The results shown here demonstrate that the spatial arrangement of axons and neurons plays a critical role in shaping network-level electrophysiological dynamics. This platform thus provides a powerful tool to systematically study ephaptic mechanisms and their contribution to circuit behavior. Moreover, printed neuronal networks offer a new path for *in vitro* disease modeling, particularly in contexts where ephaptic signaling, synaptic function, or myelination are disrupted. Additionally, I show, that SNAP can be used to construct more complex circuits and enable inclusion of several different cell types. Stimulation via electrical or optogenetic approaches is possible and may serve as a pathway to investigate neuronal circuit dynamics and optogenetic responses in SNAPs.

The modularity and adaptability of the SNAP platform open up a broad range of future research directions in both fundamental and translational neuroscience. This experimental setup enables investigation and experimental validation of ephaptic coupling. A particularly promising avenue lies in incorporating additional cell types, such as oligodendrocytes, to study the impact of myelination on ephaptic signaling. Given the insulating properties of myelin, such experiments could, for the first time, enable direct comparisons between high and low ephaptic coupling within the same engineered neural circuit architecture. The integration of simultaneous patch-clamp recordings into the SNAP platform would further enhance its capabilities, providing direct access to intracellular activity alongside the extracellular dynamics captured by MEAs. This dual readout could yield deeper insights into the mechanisms underlying spontaneous and evoked activity patterns. The platform's compatibility with optogenetics, which was already demonstrated in the current work adds another layer of precision, allowing the activation or silencing of individual neurons or even single spikes in a temporally controlled manner.

Beyond basic research, SNAP holds potential for disease modeling and drug discovery. Patient-derived hiPSC neurons could be incorporated to create disease models, allowing the study of pathophysiological circuit dynamics in a controlled setting. The pronounced sensitivity of SNAP circuits to synaptic antagonists makes the system suitable for neuropharmacological testing and high-throughput drug screening that could be applied to a range of different indications from Alzheimer's over epilepsy to depression. Future experiments will also benefit from the controlled inclusion of specific neuronal subtypes, such as excitatory and inhibitory neurons, as well as supporting glial cells. This will enable the construction of more complex, yet reproducible, *in vitro* circuits that better reflect *in vivo* conditions. Optogenetically modified neuronal populations could further serve as programmable input channels, laying the groundwork for learning paradigms and studies of information processing. Importantly, the small scale of SNAP circuits offers a testbed for validating computational models. Reduced network complexity lowers the degrees of freedom, making it easier to extract key parameters and compare empirical results with theoretical predictions. Coupled with optogenetic tools, SNAP enables precise stimulation and recording at the single-cell level, which is essential for dissecting circuit function and plasticity. In summary, the SNAP platform is a versatile tool for the long-term, non-invasive investigation of human neural circuits. Its combination of modularity, precision, and

compatibility with diverse cell types and readouts positions it as a foundational technology for advancing our understanding of neural function in health and disease.

4.5 Conclusions, limitations and outlook

The work presented in this thesis highlights the potential and versatility of *in vitro* neuronal networks as tools for studying neuronal physiology, development, and circuit dynamics. Engineered neural cultures offer advantages, including large-scale and long-term readouts, high experimental accessibility, and flexible design. Their modularity allows researchers to tailor circuits to specific experimental needs, enabling targeted investigations of fundamental processes, disease mechanisms, and pharmacological responses.

Through the development and application of *in vitro* neuronal networks and advanced platforms such as SNAP, this thesis has demonstrated how such systems can be utilized to explore the neuronal dynamics in various settings and with different questions. We could show that such systems are suited for use in various demanding settings, making them suitable for studies in altered gravity environments. We could continue this line of study and show that the same method and setup can also be used in sounding rocket and parabolic flight experiments, which I also was a part of. Currently, the data is being analyzed targeting key scientific questions of how extended and repeated phases of altered gravity influences neuronal dynamics.

The accessibility offered by *in vitro* systems makes it possible to study development of function and morphology in unprecedented detail. Defined and reproducible circuits at the single-neuron level allow to investigate the role of ephaptic coupling in shaping circuit dynamics. Despite these advantages, several limitations persist. *In vitro* networks still fall short of fully recapitulating the complexity of *in vivo* neural systems. Differences in architecture, connectivity, environmental cues, and physiological as well as systems level conditions result in circuit dynamics that, while informative, remain simplified. One persistent challenge is the prevalence of non-physiological bursting behavior, which can obscure meaningful activity patterns and hinder the interpretation of experimental results.

Moreover, the absence of structured sensory inputs and the limited diversity of cell types constrain the physiological relevance of current *in vitro* models.

To bridge the gap between *in vitro* and *in vivo* systems, future work should focus on improving the physiological fidelity of engineered networks. This includes extending the longevity and stability of cultures, refining cell-type composition through the inclusion of glial cells or myelinating cells, and integrating controlled sensory-like inputs. Advances in microfluidics and bioengineering may enable more reproducible and automated network formation, including precise single-cell placement and standardized circuit architectures, thereby increasing throughput and experimental robustness. The incorporation of tools such as optogenetics further enhances the precision with which these systems can be interrogated, making them well-suited for both mechanistic studies and translational applications. Furthermore, *in vitro* platforms have the potential to link higher-level phenomena to underlying physiological mechanisms. Incorporating defined network motifs, such as canonical microcircuit structures or retinal architectures, could provide insight into circuit-specific processing rules. Studying how such networks adapt to stimuli, encode information, or implement learning rules would not only advance basic neuroscience but also inform emerging fields such as biological computing.

In conclusion, while current *in vitro* systems are still far from the complexity of *in vivo* systems and the brain, they offer an increasingly powerful experimental framework. With continued refinement and integration of new technologies, platforms like SNAP might contribute to unraveling the principles of neural computation, disease progression, and therapeutic intervention in human-relevant models.

5. Abstract

Biological neuronal networks (NNs) can be studied *in vivo* or *in vitro*. Although *in vivo* studies allow for the observation of processes in a natural setting, such as a freely behaving animal, readout and interaction with the neuronal system are typically limited due to experimental constraints. *In vitro* approaches on the other hand offer large-scale readout and interaction capabilities as well as better accessibility. These networks can be engineered to meet experimental needs; however, achieving precise, reproducible control of their architecture at the single-cell level has so far been out of reach.

In this work, I show for the first time how this limitation can be overcome and how *in vitro* networks, recorded with multielectrode arrays (MEAs), can serve as versatile models to study neuronal function, physiology, and development under varied conditions. First, I studied NN activity under altered gravity. While experimental platforms for altered gravity conditions inherently pose challenges for biological experiments, we were able to integrate and maintain our networks. We demonstrated that altered gravity influences human NN activity, resulting in altered firing and bursting in response to gravitational stimuli, as well as adaptation processes. Second, I used high-density recording technology to study the longitudinal morphological and physiological development of NNs. We observed the formation of neuronal clusters, morphological changes, and the increase of GABAergic neurons over time. These observations have also been reported *in vivo*. Third, I used *in vitro* networks and tried to teach them a classification task through continued electrical stimulation. Although I observed more coherent activity, I did not observe signs of learning or plasticity. Finally, I developed a method to construct NNs with single-cell precision in a reproducible and controlled manner, enabling the measurement and validation of ephaptic coupling effects, as predicted by computational modeling, which was previously difficult to achieve. I could confirm significant changes in action potential velocity, synchronicity and other measures as a result of ephaptic coupling.

Overall, I demonstrated that *in vitro* neuronal systems are well-suited to answering specific questions about human NN function and development. Our novel method of engineering NNs from the bottom up with single-cell precision has the potential to be applied to disease modeling, drug development, the study of optogenetic tools, and the validation of computational model predictions, as well as fundamental neuroscience research and the study of neuronal computation.

6. List of figures

7. List of tables

8. References

Adrian ED. The Basis of Sensation. London: W.W. Norton & Co., 1928

Aebersold MJ, Dermutz H, Forró C, Weydert S, Thompson-Steckel G, Vörös J, Demkó L. “Brains on a chip”: Towards engineered neural networks. TrAC Trends in Analytical Chemistry 2016; 78: 60–69

Akarca D, Dunn AWE, Hornauer PJ, Ronchi S, Fiscella M, Wang C, Terrigno M, Jagasia R, Vértes PE, Mierau SB, Paulsen O, Eglen SJ, Hierlemann A, Astle DE, Schröter M. Homophilic wiring principles underpin neuronal network topology in vitro. bioRxiv 2022; 10.1101/2022.03.09.483605

Amin H, Maccione A, Marinaro F, Zordan S, Nieus T, Berdondini L. Electrical responses and spontaneous activity of human iPS-derived neuronal networks characterized for 3-month culture with 4096-electrode arrays. Front Neurosci 2016; 10: 121

Amos G, Vasiliauskaitė V, Duru J, Saramago MLA, Schmid T, Suter A, Torren FC, Küchler J, Ruff T, Vörös J, Vulić K. An Integrated In Vitro Platform and Biophysical Modeling Approach for Studying Synaptic Transmission in Isolated Neuronal Pairs. bioRxiv 2025; 10.1101/2025.06.04.657933

Anastassiou CA, Koch C. Ephaptic coupling to endogenous electric field activity: why bother? This review comes from a themed issue on Brain rhythms and dynamic coordination. Curr Opin Neurobiol 2015; 31: 95–103

Anastassiou CA, Montgomery SM, Barahona M, Buzsáki G, Koch C. The Effect of Spatially Inhomogeneous Extracellular Electric Fields on Neurons. Journal of Neuroscience 2010; 30: 1925–1936

Anastassiou CA, Perin R, Markram H, Koch C. Ephaptic coupling of cortical neurons. Nat Neurosci 2011; 14: 217–223

Antonello PC, Varley TF, Beggs J, Porcionatto M, Sporns O, Faber J. Self-organization of in vitro neuronal assemblies drives to complex network topology. Elife 2022; 11

Ardhanareeswaran K, Mariani J, Coppola G, Abyzov A, Vaccarino FM. Human induced pluripotent stem cells for modelling neurodevelopmental disorders. Nat Rev Neurol 2017; 13: 265–278

Ashley CC, Ridgway EB. Simultaneous Recording of Membrane Potential, Calcium Transient and Tension in Single Muscle Fibres. Nature 1968; 219: 1168–1169

van Atteveldt N, Vandermosten M, Weeda W, Bonte M. How to capture developmental brain dynamics: gaps and solutions. NPJ Sci Learn 2021; 6: 1–7

Babiloni C, Blinowska K, Bonanni L, Cichocki A, De Haan W, Del Percio C, Dubois B, Escudero J, Fernández A, Frisoni G, Guntekin B, Hajos M, Hampel H, Ifeachor E, Kilborn K, Kumar S, Johnsen K, Johannsson M, Jeong J, LeBeau F, Lizio R, Lopes da Silva F, Maestú F, McGeown WJ, McKeith I, Moretti DV, Nobili F, Olichney J, Onofrj M, Palop JJ, Rowan M, Stocchi F, Struzik ZM, Tanila H, Teipel S, Taylor JP, Weiergräber M, Yener G, Young-Pearse T, Drinkenburg WH, Randall F. What electrophysiology tells us about Alzheimer's disease: a window into the synchronization and connectivity of brain neurons. Neurobiol Aging 2020; 85: 58–73

Baden T, Euler T, Berens P. Understanding the retinal basis of vision across species. Nat Rev Neurosci 2019; 21: 5–20

Bagasrawala I, Memi F, Radonjić N V., Zecevic N. N-Methyl d-Aspartate Receptor Expression Patterns in the Human Fetal Cerebral Cortex. Cerebral Cortex 2017; 27: 5041–5053

Bakkum DJ, Frey U, Radivojevic M, Russell TL, Müller J, Fiscella M, Takahashi H, Hierlemann A. Tracking axonal action potential propagation on a high-density microelectrode array across hundreds of sites. Nat Commun 2013; 4: 1–12

Balci F, Ben Hamed S, Boraud T, Bouret S, Brochier T, Brun C, Cohen JY, Coutureau E, Deffains M, Doyère V, Gregoriou GG, Heimel JA, Kilavik BE, Lee D, Leuthardt EC, Mainen ZF, Mathis M, Monosov IE, Naudé J, Orsborn AL, Padoa-Schioppa C, Procyk E, Sabatini B, Sallet J, Sandi C, Schall JD, Soltani A, Svoboda K,

Wilson CRE, Zimmermann J. A response to claims of emergent intelligence and sentience in a dish. Neuron 2023; 111: 604–605

Ballini M, Muller J, Livi P, Chen Y, Frey U, Stettler A, Shadmani A, Viswam V, Jones IL, Jackel D, Radivojevic M, Lewandowska MK, Gong W, Fiscella M, Bakkum DJ, Heer F, Hierlemann A. A 1024-channel CMOS microelectrode array with 26,400 electrodes for recording and stimulation of electrogenic cells in vitro. IEEE J Solid-State Circuits 2014; 49: 2705–2719

Bassett DS, Bullmore E. Small-world brain networks. Neuroscientist 2006; 12: 512–523

Bassett DS, Gazzaniga MS. Understanding complexity in the human brain. Trends Cogn Sci 2011; 15: 200–209

Bassett DS, Sporns O. Network neuroscience. Nat Neurosci 2017; 20: 353–364

Bellman R. Dynamic Programming. Princeton: Princeton University Press, 1957

Berger H. Über das Elektrenkephalogramm des Menschen. Arch Psychiatr Nervenkr 1929; 87: 527–570

Blau A, Neumann T, Ziegler C, Benfenati F. Replica-moulded polydimethylsiloxane culture vessel lids attenuate osmotic drift in long-term cell cultures. J Biosci 2009; 34: 59–69

Blot A, Barbour B. Ultra-rapid axon-axon ephaptic inhibition of cerebellar Purkinje cells by the pinceau. Nat Neurosci 2014; 17: 289–295

Bokil H, Laaris N, Blinder K, Ennis M, Keller A. Ephaptic Interactions in the Mammalian Olfactory System. Journal of Neuroscience 2001; 21: RC173

Bonifazi P, Goldin M, Picardo MA, Jorquera I, Cattani A, Bianconi G, Represa A, Ben-Ari Y, Cossart R. GABAergic hub neurons orchestrate synchrony in developing hippocampal networks. Science 2009; 326: 1419–1424

Boyden ES, Zhang F, Bamberg E, Nagel G, Deisseroth K. Millisecond-timescale, genetically targeted optical control of neural activity. Nature Neuroscience 2005 8:9 2005; 8: 1263–1268

Bucci A, Büttner M, Domdei N, Rosselli FB, Znidaric M, Bartram J, Gänswein T, Diggelmann R, De Gennaro M, Cowan CS, Harmening W, Hierlemann A, Roska B, Franke F. Synchronization of visual perception within the human fovea. Nat Neurosci 2025; 21: 1959–1967

Buccino AP, Hurwitz CL, Garcia S, Magland J, Siegle JH, Hurwitz R, Hennig MH. Spikeinterface, a unified framework for spike sorting. Elife 2020; 9: 1–24

Budday S, Steinmann P, Kuhl E. Physical biology of human brain development. Front Cell Neurosci 2015; 9: 257

Busskamp V, Lewis NE, Guye P, Ng AH, Shipman SL, Byrne SM, Sanjana NE, Murn J, Li Y, Li S, Stadler M, Weiss R, Church GM. Rapid neurogenesis through transcriptional activation in human stem cells. Mol Syst Biol 2014; 10: 760

Butt SJ, Stacey JA, Teramoto Y, Vagnoni C. A role for GABAergic interneuron diversity in circuit development and plasticity of the neonatal cerebral cortex. Curr Opin Neurobiol 2017; 43: 149–155

Cai H, Ao Z, Tian C, Wu Z, Liu H, Tchieu J, Gu M, Mackie K, Guo F. Brain organoid reservoir computing for artificial intelligence. Nat Electron 2023; 6: 1032–1039

Canals I, Ginisty A, Quist E, Timmerman R, Fritze J, Miskinyte G, Monni E, Hansen MG, Hidalgo I, Bryder D, Bengzon J, Ahlenius H. Rapid and efficient induction of functional astrocytes from human pluripotent stem cells. Nat Methods 2018; 15: 693–696

Capllonch-Juan M, Sepulveda F. Modelling the effects of ephaptic coupling on selectivity and response patterns during artificial stimulation of peripheral nerves. PLoS Comput Biol 2020; 16: e1007826

Casanova MF, Casanova EL. The modular organization of the cerebral cortex: Evolutionary significance and possible links to neurodevelopmental conditions. Journal of Comparative Neurology 2019; 527: 1720–1730

Chavoshnejad P, Li X, Zhang S, Dai W, Vasung L, Liu T, Zhang T, Wang X, Razavi MJ. Role of axonal fibers in the cortical folding patterns: A tale of variability and regularity. Brain Multiphys 2021; 2: 100029

Chen R, Vakilna YS, Lassers SB, Tang WC, Brewer G. Hippocampal network axons respond to patterned theta burst stimulation with lower activity of initially higher spike train similarity from EC to DG and later similarity of axons from CA1 to EC. J Neural Eng 2023; 20: 056004

Chen X, Dzakpasu R. Observed network dynamics from altering the balance between excitatory and inhibitory neurons in cultured networks. Phys Rev E Stat Nonlin Soft Matter Phys 2010; 82: 031907

Chen Y, Tristan CA, Chen L, Jovanovic VM, Malley C, Chu PH, Ryu S, Deng T, Ormanoglu P, Tao D, Fang Y, Slamecka J, Hong H, LeClair CA, Michael S, Austin CP, Simeonov A, Singeç I. A versatile polypharmacology platform promotes cytoprotection and viability of human pluripotent and differentiated cells. Nat Methods 2021; 18: 528–541

Chiappalone M, Massobrio P, Martinoia S. Network plasticity in cortical assemblies. European Journal of Neuroscience 2008; 28: 221–237

Chiaradia I, Lancaster MA. Brain organoids for the study of human neurobiology at the interface of in vitro and in vivo. Nat Neurosci 2020; 23: 1496–1508

Chong SA, Benilova I, Shaban H, De Strooper B, Devijver H, Moechars D, Eberle W, Bartic C, Van Leuven F, Callewaert G. Synaptic dysfunction in hippocampus of transgenic mouse models of Alzheimer's disease: A multi-electrode array study. Neurobiol Dis 2011; 44: 284–291

Ciba M, Isomura T, Jimbo Y, Bahmer A, Thielemann C. Spike-contrast: A novel time scale independent and multivariate measure of spike train synchrony. J Neurosci Methods 2018; 293: 136–143

Clark DG, Abbott LF, Litwin-Kumar A. Dimension of Activity in Random Neural Networks. Phys Rev Lett 2023; 131: 118401

Clément G. The Musculo-Skeletal System in Space. In: Fundamentals of Space Medicine 2011: 181–216

Connolly S, Vulić K, Zare-Eelanjegh E, Simonett M, Duru J, Ruff T, Clément BF, Vörös J. Constructing well-defined neural networks of multiple cell types by

picking and placing of neuronal spheroids using FluidFM. bioRxiv 2024; 10.1101/2024.09.03.610979

Corlew R, Bosma MM, Moody WJ. Spontaneous, synchronous electrical activity in neonatal mouse cortical neurones. J Physiol 2004; 560: 377–390

Cotterill E, Charlesworth P, Thomas CW, Paulsen O, Eglen SJ. A comparison of computational methods for detecting bursts in neuronal spike trains and their application to human stem cell-derived neuronal networks. J Neurophysiol 2016; 116: 306–321

Cotterill E, Eglen SJ. Burst Detection Methods. Adv Neurobiol 2019; 22: 185–206

Craig AM, Graf ER, Linhoff MW. How to build a central synapse: Clues from cell culture. Trends Neurosci 2006; 29: 8–20

Craik FIM, Bialystok E. Cognition through the lifespan: Mechanisms of change. Trends Cogn Sci 2006; 10: 131–138

Crucian BE, Cubbage ML, Sams CF. Altered cytokine production by specific human peripheral blood cell subsets immediately following space flight. Journal of Interferon and Cytokine Research 2000; 20: 547–556

Cui Y, Han J, Xiao Z, Qi Y, Zhao Y, Chen B, Fang Y, Liu S, Wu X, Dai J. Systematic analysis of mrna and mirna expression of 3D-cultured neural stem cells (NSCS) in spaceflight. Front Cell Neurosci 2018; 11: 434

Damodaran S, Evans RC, Blackwell KT. Synchronized firing of fast-spiking interneurons is critical to maintain balanced firing between direct and indirect pathway neurons of the striatum. J Neurophysiol 2014; 111: 836–848

Demarse TB, Wagenaar DA, Blau AW, Potter SM. The Neurally Controlled Animat: Biological Brains Acting with Simulated Bodies. Auton Robots 2001; 11: 305–310

Demertzi A, Van Ombergen A, Tomilovskaya E, Jeurissen B, Pechenkova E, Di Perri C, Litvinova L, Amico E, Rumshiskaya A, Rukavishnikov I, Sijbers J, Sinitsyn V, Kozlovskaya IB, Sunaert S, Parizel PM, Van de Heyning PH, Laureys S, Wuyts

FL. Cortical reorganization in an astronaut's brain after long-duration spaceflight. Brain Struct Funct 2016; 221: 2873–2876

Denker M, Yegenoglu A, Grün S. Collaborative HPC-enabled workflows on the HBP Collaboratory using the Elephant framework. In: Neuroinformatics, 2018: 19

Diggelmann R, Fiscella M, Hierlemann A, Franke F. Automatic spike sorting for high-density microelectrode arrays. J Neurophysiol 2018; 120: 3155–3171

Dörig P, Stiefel P, Behr P, Sarajlic E, Bijl D, Gabi M, Vörös J, Vorholt JA, Zambelli T. Force-controlled spatial manipulation of viable mammalian cells and micro-organisms by means of FluidFM technology. Appl Phys Lett 2010; 97: 23701

Dragas J, Viswam V, Shadmani A, Chen Y, Bounik R, Stettler A, Radivojevic M, Geissler S, Obien MEJ, Müller J, Hierlemann A. In Vitro Multi-Functional Microelectrode Array Featuring 59 760 Electrodes, 2048 Electrophysiology Channels, Stimulation, Impedance Measurement, and Neurotransmitter Detection Channels. IEEE J Solid-State Circuits 2017; 52: 1576–1590

Dudek FE, Yasumura T, Rash JE. 'Non-synaptic' mechanisms in seizures and epileptogenesis. Cell Biol Int 1998; 22: 793–805

Duru J, Küchler J, Ihle SJ, Forró C, Bernardi A, Girardin S, Hengsteler J, Wheeler S, Vörös J, Ruff T. Engineered Biological Neural Networks on High Density CMOS Microelectrode Arrays. Front Neurosci 2022; 16: 829884

Emiliani V, Entcheva E, Hedrich R, Hegemann P, Konrad KR, Lüscher C, Mahn M, Pan ZH, Sims RR, Vierock J, Yizhar O. Optogenetics for light control of biological systems. Nature Reviews Methods Primers 2022; 2: 55

Fang XQ, Qiao H, Groveman BR, Feng S, Pflueger M, Xin WK, Ali MK, Lin SX, Xu J, Duclot F, Kabbaj M, Wang W, Ding XS, Santiago-Sim T, Jiang XH, Salter MW, Yu XM. Regulated internalization of NMDA receptors drives PKD1-mediated suppression of the activity of residual cell-surface NMDA receptors. Mol Brain 2015; 8: 75

Fitzgibbon T, Nestorovski Z. Morphological Consequences of Myelination in the Human Retina. Exp Eye Res 1997; 65: 809–819

Forró C, Thompson-Steckel G, Weaver S, Weydert S, Ihle S, Dermutz H, Aebersold MJ, Pilz R, Demkó L, Vörös J. Modular microstructure design to build neuronal networks of defined functional connectivity. Biosens Bioelectron 2018; 122: 75–87

Frett T, Petrat G, Jack JJ, Hemmersbach R, Anken R. Hypergravity Facilities in the ESA Ground-Based Facility Program – Current Research Activities and Future Tasks. Microgravity Sci Technol 2016; 28: 205–214

Galarreta M, Hestrin S. Electrical and chemical synapses among parvalbumin fast-spiking GABAergic interneurons in adult mouse neocortex. Proceedings of the National Academy of Sciences 2002; 99: 12438–12443

Galimberti M, Tolić-Nørrelykke IM, Favillini R, Mercatelli R, Annunziato F, Cosmi L, Liotta F, Santarlasci V, Maggi E, Pavone FS. Hypergravity speeds up the development of T-lymphocyte motility. European Biophysics Journal 2006; 35: 393–400

Ganguly K, Schinder AF, Wong ST, Poo M ming. GABA itself promotes the developmental switch of neuronal GABAergic responses from excitation to inhibition. Cell 2001; 105: 521–532

Garcia S, Buccino AP, Yger P. How Do Spike Collisions Affect Spike Sorting Performance? eNeuro 2022a; 9: 5

Garcia S, Sprenger J, Holtzman T, Buccino AP. ProbeInterface: A Unified Framework for Probe Handling in Extracellular Electrophysiology. Front Neuroinform 2022b; 16: 823056

Garrett-Bakelman FE, Darshi M, Green SJ, Gur RC, Lin L, Macias BR, McKenna MJ, Meydan C, Mishra T, Nasrini J, Piening BD, Rizzardi LF, Sharma K, Siamwala JH, Taylor L, Vitaterna MH, Afkarian M, Afshinnekoo E, Ahadi S, Ambati A, Arya M, Bezdan D, Callahan CM, Chen S, Choi AMK, Chlipala GE, Contrepois K, Covington M, Crucian BE, De Vivo I, Dinges DF, Ebert DJ, Feinberg JI, Gandara JA, George KA, Goutsias J, Grills GS, Hargens AR, Heer M, Hillary RP, Hoofnagle AN, Hook VYH, Jenkinson G, Jiang P, Keshavarzian A, Laurie SS,

Lee-McMullen B, Lumpkins SB, MacKay M, Maienschein-Cline MG, Melnick AM, Moore TM, Nakahira K, Patel HH, Pietrzyk R, Rao V, Saito R, Salins DN, Schilling JM, Sears DD, Sheridan CK, Stenger MB, Tryggvadottir R, Urban AE, Vaisar T, Van Espen B, Zhang J, Ziegler MG, Zwart SR, Charles JB, Kundrot CE, Scott GBI, Bailey SM, Basner M, Feinberg AP, Lee SMC, Mason CE, Mignot E, Rana BK, Smith SM, Snyder MP, Turek FW. The NASA twins study: A multidimensional analysis of a year-long human spaceflight. Science 2019; 364

Geller HM, Cheng KY, Goldsmith NK, Romero AA, Zhang AL, Morris EJ, Grandison L. Oxidative stress mediates neuronal DNA damage and apoptosis in response to cytosine arabinoside. J Neurochem 2001; 78: 265–275

Genchi GG, Cialdai F, Monici M, Mazzolai B, Mattoli V, Ciofani G. Hypergravity stimulation enhances PC12 neuron-like cell differentiation. Biomed Res Int 2015; 2015

Girardin S, Clément B, Ihle SJ, Weaver S, Petr JB, Mateus JC, Duru J, Krubner M, Forró C, Ruff T, Fruh I, Müller M, Vörös J. Topologically controlled circuits of human iPSC-derived neurons for electrophysiology recordings. Lab Chip 2022; 22: 1386–1403

Gold C, Henze DA, Koch C, Buzsáki G. On the origin of the extracellular action potential waveform: A modeling study. J Neurophysiol 2006; 95: 3113–3128

Gozdas E, Holland SK, Altaye M. Developmental changes in functional brain networks from birth through adolescence. Hum Brain Mapp 2019; 40: 1434–1444

Habibey R, Golabchi A, Blau A. Microchannel Scaffolds for Neural Signal Acquisition and Analysis. In: Londral AR, Encarnação P, Rovira JLP, eds. Neurotechnology, Electronics, and Informatics. Cham: Springer International Publishing, 2015a: 47–64

Habibey R, Golabchi A, Latifi S, Difato F, Blau A. A microchannel device tailored to laser axotomy and long-term microelectrode array electrophysiology of functional regeneration. Lab Chip 2015b; 15: 4578–4590

Habibey R, Jesús J, Arias ER, Striebel J, Busskamp V. Microfluidics for Neuronal Cell and Circuit Engineering. Chem Rev 2022a; 122: 14842-14880

Habibey R, Latifi S, Mousavi H, Pesce M, Arab-Tehrany E, Blau A. A multielectrode array microchannel platform reveals both transient and slow changes in axonal conduction velocity. Sci Rep 2017; 7: 8558

Habibey R, Sharma K, Swiersy A, Busskamp V. Optogenetics for neural transplant manipulation and functional analysis. Biochem Biophys Res Commun 2020; 527: 343–349

Habibey R, Striebel J, Meinert M, Latiftikhereshki R, Schmieder F, Nasiri R, Latifi S. Engineered modular neuronal networks-on-chip represent structure-function relationship. Biosens Bioelectron 2024; 261: 116518

Habibey R, Striebel J, Schmieder F, Czarske J, Busskamp V. Long-term morphological and functional dynamics of human stem cell-derived neuronal networks on high-density micro-electrode arrays. Front Neurosci 2022b; 16: 951964

Habibey R, Striebel J, Sharma K, Busskamp V. Optogenetic Control of Human Stem Cell-Derived Neurons. In: Gordeliy V, eds. Rhodopsin. Methods in Molecular Biology. New York: Humana, 2022c: 2501: 339–360

Häder DP, Braun M, Grimm D, Hemmersbach R. Gravireceptors in eukaryotes - a comparison of case studies on the cellular level. NPJ Microgravity 2017; 3: 13

Hamill OP, Marty A, Neher E, Sakmann B, Sigworth FJ. Improved patch-clamp techniques for high-resolution current recording from cells and cell-free membrane patches. Pflugers Arch 1981; 391: 85–100

Han KS, Chen CH, Khan MM, Guo C, Regehr WG. Climbing fiber synapses rapidly and transiently inhibit neighboring Purkinje cells via ephaptic coupling. Nat Neurosci 2020; 23: 1399–1409

Han KS, Guo C, Chen CH, Witter L, Osorno T, Regehr WG. Ephaptic Coupling Promotes Synchronous Firing of Cerebellar Purkinje Cells. Neuron 2018; 100: 564-578.e3

Harris CR, Millman KJ, van der Walt SJ, Gommers R, Virtanen P, Cournapeau D, Wieser E, Taylor J, Berg S, Smith NJ, Kern R, Picus M, Hoyer S, van Kerkwijk MH, Brett M, Haldane A, del Río JF, Wiebe M, Peterson P, Gérard-Marchant P, Sheppard K, Reddy T, Weckesser W, Abbasi H, Gohlke C, Oliphant TE. Array programming with NumPy. Nature 2020; 585: 357–362

Hassabis D, Kumaran D, Summerfield C, Botvinick M. Neuroscience-Inspired Artificial Intelligence. Neuron 2017; 95: 245–258

Hattori N. Cerebral organoids model human brain development and microcephaly. Mov Disord 2013; 29: 185–185

Hauslage J, Abbrecht M, Hanke L, Hemmersbach R, Koch C, Hanke W, Kohn FPM. Cytosolic Calcium Concentration Changes in Neuronal Cells Under Clinorotation and in Parabolic Flight Missions. Microgravity Sci Technol 2016; 28: 633–638

Hemmersbach R, Von Der Wiesche M, Seibt D. Ground-based experimental platforms in gravitational biology and human physiology. Signal Transduct 2006; 6: 381–387

Hoagland DT, Santos W, Poelzing S, Gourdie RG. The role of the gap junction perinexus in cardiac conduction: Potential as a novel anti-arrhythmic drug target. Prog Biophys Mol Biol 2019; 144: 41–50

Hockemeyer D, Jaenisch R. Induced pluripotent stem cells meet genome editing. Cell Stem Cell 2016; 18: 573–586

Huber L, Finn ES, Chai Y, Goebel R, Stirnberg R, Stöcker T, Marrett S, Uludag K, Kim SG, Han SH, Bandettini PA, Poser BA. Layer-dependent functional connectivity methods. Prog Neurobiol 2021; 207: 101835

Hunter JD. Matplotlib: A 2D graphics environment. Comput Sci Eng 2007; 9: 90–95

Hyvärinen T, Hyysalo A, Kapucu FE, Aarnos L, Vinogradov A, Eglen SJ, Ylä-Outinen L, Narkilahti S. Functional characterization of human pluripotent stem cell-derived cortical networks differentiated on laminin-521 substrate: comparison to rat cortical cultures. Sci Rep 2019; 9: 1–15

Ihle SJ, Girardin S, Felder T, Ruff T, Hengsteler J, Duru J, Weaver S, Forró C, Vörös J. An experimental paradigm to investigate stimulation dependent activity in topologically constrained neuronal networks. Biosens Bioelectron 2022; 201: 113896

Ilic D, Ogilvie C. Concise Review: Human Embryonic Stem Cells—What Have We Done? What Are We Doing? Where Are We Going? Stem Cells 2017; 35: 17–25

Ivanovic E, Kucera JP. Localization of Na+ channel clusters in narrowed perinexi of gap junctions enhances cardiac impulse transmission via ephaptic coupling: a model study. J Physiol 2021; 599: 4779

Jiang X, Nardelli J. Cellular and molecular introduction to brain development. Neurobiol Dis 2016; 92: 3–17

Jimbo Y, Tateno T, Robinson HPC. Simultaneous Induction of Pathway-Specific Potentiation and Depression in Networks of Cortical Neurons. Biophys J 1999; 76: 670–678

Jun JJ, Magland JF, Mitelut C, Barnett AH. Ironclust: Scalable and drift-resistant spike sorting for long-duration, high-channel count recordings. 2020.

Jun JJ, Steinmetz NA, Siegle JH, Denman DJ, Bauza M, Barbarits B, Lee AK, Anastassiou CA, Andrei A, Aydin Ç, Barbic M, Blanche TJ, Bonin V, Couto J, Dutta B, Gratiy SL, Gutnisky DA, Häusser M, Karsh B, Ledochowitsch P, Lopez CM, Mitelut C, Musa S, Okun M, Pachitariu M, Putzeys J, Rich PD, Rossant C, Sun WL, Svoboda K, Carandini M, Harris KD, Koch C, O'Keefe J, Harris TD. Fully integrated silicon probes for high-density recording of neural activity. Nature 2017; 551: 232–236

Kagan BJ, Kitchen AC, Tran NT, Habibollahi F, Khajehnejad M, Parker BJ, Bhat A, Rollo B, Razi A, Friston KJ. In vitro neurons learn and exhibit sentience when embodied in a simulated game-world. Neuron 2022; 110: 3952-3969.e8

Kagan BJ, Razi A, Bhat A, Kitchen AC, Tran NT, Habibollahi F, Khajehnejad M, Parker BJ, Rollo B, Friston KJ. Scientific communication and the semantics of sentience. Neuron 2023; 111: 606–607

Kamermans M, Fahrenfort I, Schultz K, Janssen-Bienhold U, Sjoerdsma T, Weiler R. Hemichannel-mediated inhibition in the outer retina. Science 2001; 292: 1178–1180

Kamkim A, Kiseleva I. Mechanosensitivity of the Nervous System. Kamkim A, Kiseleva I, editors. Springer Dordrecht; 2008.

Kanas N, Manzey D. Space Psychology and Psychiatry. Dordrecht: Springer Netherlands, 2008

Katz B, Schmitt OH. Electric interaction between two adjacent nerve fibres. J Physiol 1940; 97: 471–488

Khazipov R, Luhmann HJ. Early patterns of electrical activity in the developing cerebral cortex of humans and rodents. Trends Neurosci 2006; 29: 414–418

Kilb W, Kirischuk S, Luhmann HJ. Electrical activity patterns and the functional maturation of the neocortex. European Journal of Neuroscience 2011; 34: 1677–1686

Kim JY, Paredes MF. Implications of Extended Inhibitory Neuron Development. Int J Mol Sci 2021; 22: 5113

Kirwan P, Turner-Bridger B, Peter M, Momoh A, Arambepola D, Robinson HPC, Livesey FJ. Development and function of human cerebral cortex neural networks from pluripotent stem cells in vitro. Development 2015; 142: 3178–3187

Klapoetke NC, Murata Y, Kim SS, Pulver SR, Birdsey-Benson A, Cho YK, Morimoto TK, Chuong AS, Carpenter EJ, Tian Z, Wang J, Xie Y, Yan Z, Zhang Y, Chow BY, Surek B, Melkonian M, Jayaraman V, Constantine-Paton M, Wong GKS, Boyden ES. Independent optical excitation of distinct neural populations. Nat Methods 2014; 11: 338–346

Klapper SD, Sauter EJ, Swiersy A, Hyman MAE, Bamann C, Bamberg E, Busskamp V. On-demand optogenetic activation of human stem-cell-derived neurons. Sci Rep 2017; 7: 14450

Kohn F, Hauslage J, Hanke W. Membrane Fluidity Changes, A Basic Mechanism of Interaction of Gravity with Cells? Microgravity Sci Technol 2017; 29: 337–342

Kohn FPM. High throughput fluorescent screening of membrane potential and intracellular calcium concentration under variable gravity conditions. Microgravity Sci Technol 2013; 25: 113–120

Kohn FPM, Hauslage J. The gravity dependence of pharmacodynamics: the integration of lidocaine into membranes in microgravity. npj Microgravity 2019 5:1 2019; 5: 5

Kohn FPM, Ritzmann R. Gravity and neuronal adaptation, in vitro and in vivo - from neuronal cells up to neuromuscular responses: a first model. European Biophysics Journal 2018; 47: 97–107

Kramer TS, Flavell SW. Building and integrating brain-wide maps of nervous system function in invertebrates. Curr Opin Neurobiol 2024; 86: 102868

Kriegeskorte N, Douglas PK. Cognitive computational neuroscience. Nat Neurosci 2018; 21: 1148–1160

Kullback S, Leibler RA. On Information and Sufficiency. The Annals of Mathematical Statistics 1951; 22: 79–86

Kutsche LK, Gysi DM, Fallmann J, Lenk K, Petri R, Swiersy A, Klapper SD, Pircs K, Khattak S, Stadler PF, Jakobsson J, Nowick K, Busskamp V. Combined Experimental and System-Level Analyses Reveal the Complex Regulatory Network of miR-124 during Human Neurogenesis. Cell Syst 2018; 7: 438-452.e8

Lam RS, Töpfer FM, Wood PG, Busskamp V, Bamberg E. Functional Maturation of Human Stem Cell-Derived Neurons in Long-Term Cultures. PLoS One 2017; 12: e0169506

Lancaster MA, Renner M, Martin CA, Wenzel D, Bicknell LS, Hurles ME, Homfray T, Penninger JM, Jackson AP, Knoblich JA. Cerebral organoids model human brain development and microcephaly. Nature 2013; 501: 373–379

Latifi S, Mitchell S, Habibey R, Hosseini F, Donzis E, Estrada-Sanchez AM, Rezaei Nejad H, Levine M, Golshani P, Thomas Carmichael S. Neuronal Network Topology Indicates Distinct Recovery Processes after Stroke. Cerebral Cortex 2020; 30: 6363–6375

Latifi S, Tamayol A, Habibey R, Sabzevari R, Kahn C, Geny D, Eftekharpour E, Annabi N, Blau A, Linder M, Arab-Tehrany E. Natural lecithin promotes neural network complexity and activity. Sci Rep 2016; 6: 25777

LeBlanc A, Lin C, Shackelford L, Sinitsyn V, Evans H, Belichenko O, Schenkman B, Kozlovskaya I, Oganov V, Bakulin A, Hedrick T, Feeback D. Muscle volume, MRI relaxation times (T2), and body composition after spaceflight. J Appl Physiol 2000; 89: 2158–2164

Lee SW, Lee SS. Shrinkage ratio of PDMS and its alignment method for the wafer level process. Microsystem Technologies 2008; 14: 205–208

Legendy CR, Salcman M. Bursts and recurrences of bursts in the spike trains of spontaneously active striate cortex neurons. J Neurophysiol 1985; 53: 926–939

de León-López CAM, Carretero-Rey M, Khan ZU. AMPA Receptors in Synaptic Plasticity, Memory Function, and Brain Diseases. Cell Mol Neurobiol 2025; 45: 14

Levakov G, Faskowitz J, Avidan G, Sporns O. Mapping individual differences across brain network structure to function and behavior with connectome embedding. Neuroimage 2021; 242: 118469

Levy O, Ziv NE, Marom S. Enhancement of neural representation capacity by modular architecture in networks of cortical neurons. European Journal of Neuroscience 2012; 35: 1753–1760

Li J, Curley WH, Guerin B, Dougherty DD, Dalca A V., Fischl B, Horn A, Edlow BL. Mapping the subcortical connectivity of the human default mode network. Neuroimage 2021; 245: 118758

Li S, Liu Y, Hua S, Wang Y, Sun S, Jiang L, Lu C, Liu J, Shi H, Wu P, Cai X, Luo J, Li S, Liu Y, Hua S, Wang Y, Sun S, Jiang L, Lu C, Liu J, Cai X, Luo J, Shi H, Wu

P. Advanced Brain-on-a-Chip for Wetware Computing: A Review. Advanced Science 2025; 12: e08120

Lichterfeld Y, Kalinski L, Schunk S, Schmakeit T, Feles S, Frett T, Herrmann H, Hemmersbach R, Liemersdorf C. Hypergravity Attenuates Reactivity in Primary Murine Astrocytes. Biomedicines 2022; 10: 1966

Lillicrap TP, Santoro A, Marris L, Akerman CJ, Hinton G. Backpropagation and the brain. Nat Rev Neurosci 2020; 21: 335–346

Lin J, Abraham A, George SA, Greer-Short A, Blair GA, Moreno A, Alber BR, Kay MW, Poelzing S. Ephaptic Coupling Is a Mechanism of Conduction Reserve During Reduced Gap Junction Coupling. Front Physiol 2022; 13: 848019

Lin J, Keener JP. Ephaptic coupling in cardiac myocytes. IEEE Trans Biomed Eng 2013; 60: 576–582

Litke AM, Bezayiff N, Chichilnisky EJ, Cunningham W, Dabrowski W, Grillo AA, Grivich M, Grybos P, Hottowy P, Kachiguine S, Kalmar RS, Mathieson K, Petrusca D, Rahman M, Sher A. What does the eye tell the brain?: Development of a system for the large-scale recording of retinal output activity. IEEE Trans Nucl Sci 2004; 51: 1434–1440

Lo B, Parham L. Ethical Issues in Stem Cell Research. Endocr Rev 2009; 30: 204–213

Lu C, Shi X, Allen A, Baez-Nieto D, Nikish A, Sanjana NE, Pan JQ. Overexpression of NEUROG2 and NEUROG1 in human embryonic stem cells produces a network of excitatory and inhibitory neurons. The FASEB Journal 2019; 33: 5287

Luhmann HJ, Khazipov R. Neuronal Activity Patterns in the Developing Barrel Cortex. Neuroscience 2018; 368: 256–267

Luhmann HJ, Sinning A, Yang JW, Reyes-Puerta V, Stüttgen MC, Kirischuk S, Kilb W. Spontaneous neuronal activity in developing neocortical networks: From single cells to large-scale interactions. Front Neural Circuits 2016; 10: 197897

Luo L. Architectures of neuronal circuits. Science 2021; 373: eabg7285

Maeda E, Robinson HPC, Kawana A. The mechanisms of generation and propagation of synchronized bursting in developing networks of cortical neurons. Journal of Neuroscience 1995; 15: 6834–6845

Mager T, Morena DLD La, Senn V, Schlotte J, Derrico A, Feldbauer K, Wrobel C, Jung S, Bodensiek K, Rankovic V, Browne L, Huet A, Jüttner J, Wood PG, Letzkus JJ, Moser T, Bamberg E. High frequency neural spiking and auditory signaling by ultrafast red-shifted optogenetics. Nat Commun 2018; 9: 1750

Maier JAM, Cialdai F, Monici M, Morbidelli L. The impact of microgravity and hypergravity on endothelial cells. Biomed Res Int 2015; 1: 434803

Mannal N, Kleiner K, Fauler M, Dougalis A, Poetschke C, Liss B. Multi-Electrode Array Analysis Identifies Complex Dopamine Responses and Glucose Sensing Properties of Substantia Nigra Neurons in Mouse Brain Slices. Front Synaptic Neurosci 2021; 13: 635050

Manzini A, Jones EJH, Charman T, Elsabbagh M, Johnson MH, Singh I. Ethical dimensions of translational developmental neuroscience research in autism. J Child Psychol Psychiatry 2021; 62: 1363–1373

Marconi E, Nieus T, Maccione A, Valente P, Simi A, Messa M, Dante S, Baldelli P, Berdondini L, Benfenati F. Emergent Functional Properties of Neuronal Networks with Controlled Topology. PLoS One 2012; 7: e34648

Martinez P, Sprecher SG. Of Circuits and Brains: The Origin and Diversification of Neural Architectures. Front Ecol Evol 2020; 8: 525220

Masi E, Ciszak M, Comparini D, Monetti E, Pandolfi C, Azzarello E, Mugnai S, Baluška F, Mancuso S. The electrical network of maize root apex is gravity dependent. Sci Rep 2015; 5: 7730

Matsuda T, Cepko CL. Controlled expression of transgenes introduced by in vivo electroporation. Proc Natl Acad Sci U S A 2007; 104: 1027–1032

McCready FP, Gordillo-Sampedro S, Pradeepan K, Martinez-Trujillo J, Ellis J. Multielectrode Arrays for Functional Phenotyping of Neurons from Induced

Pluripotent Stem Cell Models of Neurodevelopmental Disorders. Biology 2022; 11: 316

McKinney W. Data Structures for Statistical Computing in Python. In: van der Walt S, Millman J, eds. Proceedings of the 9th Python in Science Conference, 2010: 56–61

Meissner K, Hanke W. Patch-clamp experiments under micro-gravity. J Gravit Physiol 2002; 9: 377–378

Meissner K, Hanke W. Action potential properties are gravity dependent. Microgravity Sci Technol 2005; 17: 38–43

Mezinska S, Gallagher L, Verbrugge M, Bunnik EM. Ethical issues in genomics research on neurodevelopmental disorders: a critical interpretive review. Hum Genomics 2021; 15: 16

Miyamoto KI, Ichimura H, Wagner T, Schöning MJ, Yoshinobu T. Chemical imaging of the concentration profile of ion diffusion in a microfluidic channel. Sens Actuators B Chem 2013; 189: 240–245

Mossink B, Verboven AHA, van Hugte EJH, Klein Gunnewiek TM, Parodi G, Linda K, Schoenmaker C, Kleefstra T, Kozicz T, van Bokhoven H, Schubert D, Nadif Kasri N, Frega M. Human neuronal networks on micro-electrode arrays are a highly robust tool to study disease-specific genotype-phenotype correlations in vitro. Stem Cell Reports 2021; 16: 2182–2196

Müller J, Ballini M, Livi P, Chen Y, Radivojevic M, Shadmani A, Viswam V, Jones IL, Fiscella M, Diggelmann R, Stettler A, Frey U, Bakkum DJ, Hierlemann A. High-resolution CMOS MEA platform to study neurons at subcellular, cellular, and network levels. Lab Chip 2015; 15: 2767–2780

Nagel G, Ollig D, Fuhrmann M, Kateriya S, Musti AM, Bamberg E, Hegemann P. Channelrhodopsin-1: A light-gated proton channel in green algae. Science 2002; 296: 2395–2398

Nagel G, Szellas T, Huhn W, Kateriya S, Adeishvili N, Berthold P, Ollig D, Hegemann P, Bamberg E. Channelrhodopsin-2, a directly light-gated cation-selective membrane channel. Proc Natl Acad Sci U S A 2003; 100: 13940–13945

Nam Y, Chang J, Khatami D, Brewer GJ, Wheeler BC. Patterning to enhance activity of cultured neuronal networks. IEE Proc Nanobiotechnol 2004; 151: 109–115

Ndyabawe K, Kisaalita WS. Engineering microsystems to recapitulate brain physiology on a chip. Drug Discov Today 2019; 24: 1725–1730

Neher E, Sakmann B. Single-channel currents recorded from membrane of denervated frog muscle fibres. Nature 1976; 260: 799–802

Ng AHM, Khoshakhlagh P, Rojo Arias JE, Pasquini G, Wang K, Swiersy A, Shipman SL, Appleton E, Kiaee K, Kohman RE, Vernet A, Dysart M, Leeper K, Saylor W, Huang JY, Graveline A, Taipale J, Hill DE, Vidal M, Melero-Martin JM, Busskamp V, Church GM. A comprehensive library of human transcription factors for cell fate engineering. Nat Biotechnol 2021; 39: 510–519

Nikolaev YA, Dosen PJ, Laver DR, Van Helden DF, Hamill OP. Single mechanically-gated cation channel currents can trigger action potentials in neocortical and hippocampal pyramidal neurons. Brain Res 2015; 1608: 1–13

Nikolakopoulou P, Rauti R, Voulgaris D, Shlomy I, Maoz BM, Herland A. Recent progress in translational engineered in vitro models of the central nervous system. Brain 2020; 143: 3181–3213

Novellino A, D'Angelo P, Cozzi L, Chiappalone M, Sanguineti V, Martinoia S. Connecting Neurons to a Mobile Robot: An In Vitro Bidirectional Neural Interface. Comput Intell Neurosci 2007; 2007: 12725

Odawara A, Katoh H, Matsuda N, Suzuki I. Induction of long-term potentiation and depression phenomena in human induced pluripotent stem cell-derived cortical neurons. Biochem Biophys Res Commun 2016a; 469: 856–862

Odawara A, Katoh H, Matsuda N, Suzuki I. Physiological maturation and drug responses of human induced pluripotent stem cell-derived cortical neuronal networks in long-term culture. Sci Rep 2016b; 6: 26181

Odawara A, Saitoh Y, Alhebshi AH, Gotoh M, Suzuki I. Long-term electrophysiological activity and pharmacological response of a human induced pluripotent stem cell-derived neuron and astrocyte co-culture. Biochem Biophys Res Commun 2014; 443: 1176–1181

Van Ombergen A, Demertzi A, Tomilovskaya E, Jeurissen B, Sijbers J, Kozlovskaya IB, Parizel PM, Van de Heyning PH, Sunaert S, Laureys S, Wuyts FL. The effect of spaceflight and microgravity on the human brain. J Neurol 2017; 264: 18–22

Van Ombergen A, Jillings S, Jeurissen B, Tomilovskaya E, Rühl RM, Rumshiskaya A, Nosikova I, Litvinova L, Annen J, Pechenkova E V., Kozlovskaya IB, Sunaert S, Parizel PM, Sinitsyn V, Laureys S, Sijbers J, zu Eulenburg P, Wuyts FL. Brain Tissue-Volume Changes in Cosmonauts. N Engl J Med 2018; 379: 1678–1680

Pachitariu M, Sridhar S, Stringer C. Solving the spike sorting problem with Kilosort. bioRxiv 2023; 10.1101/2023.01.07.523036

Pang ZP, Yang N, Vierbuchen T, Ostermeier A, Fuentes DR, Yang TQ, Citri A, Sebastiano V, Marro S, Südhof TC, Wernig M. Induction of human neuronal cells by defined transcription factors. Nature 2011; 476: 220–223

Pani G, Samari N, Quintens R, de Saint-Georges L, Meloni MA, Baatout S, Van Oostveldt P, Benotmane MA. Morphological and Physiological Changes in Mature In Vitro Neuronal Networks towards Exposure to Short-, Middle- or Long-Term Simulated Microgravity. Paul F, editor. PLoS One 2013; 8: e73857

Park MU, Bae Y, Lee KS, Song JH, Lee SM, Yoo KH. Collective dynamics of neuronal activities in various modular networks. Lab Chip 2021; 21: 951–961

Pașca SP. The rise of three-dimensional human brain cultures. Nature 2018; 553: 437–445

Pastrana E. Focus on mapping the brain. Nat Methods 2013; 10: 481

Paulsen K, Thiel C, Timm J, Schmidt PM, Huber K, Tauber S, Hemmersbach R, Seibt D, Kroll H, Grote KH, Zipp F, Schneider-Stock R, Cogoli A, Hilliger A, Engelmann F, Ullrich O. Microgravity-induced alterations in signal transduction in cells of the immune system. Acta Astronaut 2010; 67: 1116–1125

Piccolino M. Luigi Galvani and animal electricity: Two centuries after the foundation of electrophysiology. Trends Neurosci 1997; 20: 443–448

Pine J. Recording action potentials from cultured neurons with extracellular microcircuit electrodes. J Neurosci Methods 1980; 2: 19–31

Pinotsis DA, Miller EK. In vivo ephaptic coupling allows memory network formation. Cerebral Cortex 2023; 33: 9877–9895

Popova NK, Kulikov A V., Naumenko VS. Spaceflight and brain plasticity: Spaceflight effects on regional expression of neurotransmitter systems and neurotrophic factors encoding genes. Neurosci Biobehav Rev 2020; 119: 396–405

Preibisch S, Saalfeld S, Tomancak P. Globally optimal stitching of tiled 3D microscopic image acquisitions. Bioinformatics 2009; 25: 1463–1465

Qian X, Song H, Ming GL. Brain organoids: Advances, applications and challenges. Development 2019; 146: dev166074

Rabinovitch A, Rabinovitch R, Smolik E, Biton Y, Braunstein D. Ephaptic conduction in tonic–clonic seizures. Front Neurol 2024; 15: 1477174

Ramón y Cajal S. Estructura de los centros nerviosos de las aves. Rev Trim Histol Norm Pat 1888; 1: 1–10

Raybaud C, Ahmad T, Rastegar N, Shroff M, Al Nassar M. The premature brain: developmental and lesional anatomy. Neuroradiology 2013; 55: 23–40

Richards SEV, Van Hooser SD. Neural architecture: From cells to circuits. J Neurophysiol 2018; 120: 854–866

Ritzmann R, Krause A, Freyler K, Gollhofer A. Gravity and Neuronal Adaptation: Neurophysiology of Reflexes from Hypo- to Hypergravity Conditions. Microgravity Sci Technol 2017; 29: 9–18

Roberts DR, Albrecht MH, Collins HR, Asemani D, Chatterjee AR, Spampinato MV, Zhu X, Chimowitz MI, Antonucci MU. Effects of Spaceflight on Astronaut Brain Structure as Indicated on MRI. New England Journal of Medicine 2017; 377: 1746–1753

Roberts DR, Stahn AC, Seidler RD, Wuyts FL. Towards understanding the effects of spaceflight on the brain. Lancet Neurol 2020; 19: 808

Robinton DA, Daley GQ. The promise of induced pluripotent stem cells in research and therapy. Nature 2012; 481: 295–305

Rognan D, Boulanger T, Hoffmann R, Vercauteren DP, Andre J-M, Durant F, Wermuth C-G. Structure and Molecular Modeling of GABAa Receptor Antagonists. J Med Chem 1992; 35: 1969–1977

Rolston JD, Gross RE, Potter SM. Common median referencing for improved action potential detection with multielectrode arrays. In: 2009 Annual International Conference of the IEEE Engineering in Medicine and Biology Society. Minneapolis: IEEE Conmputer Society,y 2009: 1604–1607

Ronchi S, Buccino AP, Prack G, Kumar SS, Schröter M, Fiscella M, Hierlemann A. Electrophysiological Phenotype Characterization of Human iPSC-Derived Neuronal Cell Lines by Means of High-Density Microelectrode Arrays. Adv Biol 2021; 5: 2000223

Rosenthal G, Váša F, Griffa A, Hagmann P, Amico E, Goñi J, Avidan G, Sporns O. Mapping higher-order relations between brain structure and function with embedded vector representations of connectomes. Nat Commun 2018; 9: 2178

Rösner H, Wassermann T, Möller W, Hanke W. Effects of altered gravity on the actin and microtubule cytoskeleton of human SH-SY5Y neuroblastoma cells. Protoplasma 2006; 229: 225–234

Roy-O'Reilly M, Mulavara A, Williams T. A review of alterations to the brain during spaceflight and the potential relevance to crew in long-duration space exploration. NPJ Microgravity 2021; 7: 5

Saalfrank D, Konduri AK, Latifi S, Habibey R, Golabchi A, Martiniuc AV, Knoll A, Ingebrandt S, Blau A. Incubator-independent cell-culture perfusion platform for continuous long-term microelectrode array electrophysiology and time-lapse imaging. R Soc Open Sci 2015; 2: 150031

Sasaki T, Suzuki I, Yokoi R, Sato K, Ikegaya Y. Synchronous spike patterns in differently mixed cultures of human iPSC-derived glutamatergic and GABAergic neurons. Biochem Biophys Res Commun 2019; 513: 300–305

Sauter EJ, Kutsche LK, Klapper SD, Busskamp V. Induced neurons for the study of neurodegenerative and neurodevelopmental disorders. Methods in Molecular Biology 2019; 1942: 101–121

Schindelin J, Arganda-Carreras I, Frise E, Kaynig V, Longair M, Pietzsch T, Preibisch S, Rueden C, Saalfeld S, Schmid B, Tinevez JY, White DJ, Hartenstein V, Eliceiri K, Tomancak P, Cardona A. Fiji: an open-source platform for biological-image analysis. Nat Methods 2012; 9: 676–682

Schmidt H, Hahn G, Deco G, Knösche TR. Ephaptic coupling in white matter fibre bundles modulates axonal transmission delays. PLoS Comput Biol 2021; 17: e1007858

Schmidt H, Knösche TR. Action potential propagation and synchronisation in myelinated axons. PLoS Comput Biol 2019; 15: e1007004

Schmieder F, Habibey R, Striebel J, Büttner L, Czarske J, Busskamp V. Tracking connectivity maps in human stem cell-derived neuronal networks by holographic optogenetics. Life Sci Alliance 2022; 5: e202101268

Segev R, Benveniste M, Shapira Y, Ben-Jacob E. Formation of Electrically Active Clusterized Neural Networks. Phys Rev Lett 2003; 90: 4

Seidler RD, Mao XW, Tays GD, Wang T, zu Eulenburg P. Effects of spaceflight on the brain. Lancet Neurol 2024; 23: 826–835

Serre T, Oliva A, Poggio T. A feedforward architecture accounts for rapid categorization. Proc Natl Acad Sci U S A 2007; 104: 6424–6429

Shi Y, Inoue H, Wu JC, Yamanaka S. Induced pluripotent stem cell technology: a decade of progress. Nat Rev Drug Discov 2016; 16: 115–130

Shivacharan RS, Chiang CC, Wei X, Subramanian M, Couturier NH, Pakalapati N, Durand DM. Neural recruitment by ephaptic coupling in epilepsy. Epilepsia 2021; 62: 1505–1517

Sibonga JD. Spaceflight-induced bone loss: Is there an Osteoporosis Risk? Curr Osteoporos Rep 2013; 11: 92–98

Sieber M, Hanke W, Kohn FPM. Modification of Membrane Fluidity by Gravity. Open J Biophys 2014; 04: 105–111

Silbereis JC, Pochareddy S, Zhu Y, Li M, Sestan N. The Cellular and Molecular Landscapes of the Developing Human Central Nervous System. Neuron 2016; 89: 248

Smirnova L, Caffo BS, Gracias DH, Huang Q, Morales Pantoja IE, Tang B, Zack DJ, Berlinicke CA, Boyd JL, Harris TD, Johnson EC, Kagan BJ, Kahn J, Muotri AR, Paulhamus BL, Schwamborn JC, Plotkin J, Szalay AS, Vogelstein JT, Worley PF, Hartung T. Organoid intelligence (OI): the new frontier in biocomputing and intelligence-in-a-dish. Frontiers in Science 2023; 1: 1017235

Smith SM, Wastney ME, Morukov B V., Larina IM, Nyquist LE, Abrams SA, Taran EN, Shih CY, Nillen JL, Davis-Street JE, Rice BL, Lane HW. Calcium metabolism before, during, and after a 3-mo spaceflight: Kinetic and biochemical changes. Am J Physiol Regul Integr Comp Physiol 1999; 277: R1-R10

Sporns O. Making sense of brain network data. Nat Methods 2013; 10: 491–493

Stacey RG, Hilbert L, Quail T. Computational study of synchrony in fields and microclusters of ephaptically coupled neurons. J Neurophysiol 2015; 113: 3229–3241

Steidl EM, Neveu E, Bertrand D, Buisson B. The adult rat hippocampal slice revisited with multi-electrode arrays. Brain Res 2006; 1096: 70–84

Stevens B, Polleux F, Barres BA. The Cells of the Nervous System. In: Kandel ER, Koester JD, Mack SH, Siegelbaum SA, editors. Principles of Neural Science 6th ed. 2021.

Stiles J, Jernigan TL. The basics of brain development. Neuropsychol Rev 2010; 20: 327–348

Striebel J, Habibey R, Wendland D, Gehring H, Podoliak E, Pawlick JS, Sharma K, Ng AHM, Pernice W, Busskamp V. Empirical validation of ephaptic coupling in printed human neural circuits. bioRxiv 2025a; 10.1101/2025.05.21.655141

Striebel J, Habibey R, Wendland D, Gehring H, Podoliak E, Pawlick JS, Sharma K, Ng AHM, Pernice W, Busskamp V. Reproducible Human Neural Circuits Printed with Single-Cell Precision Reveal Functional Roles of Ephaptic Coupling. ACS Nano 2025b; in press

Striebel J, Kalinski L, Sturm M, Drouvé N, Peters S, Lichterfeld Y, Habibey R, Hauslage J, El Sheikh S, Busskamp V, Liemersdorf C. Human neural network activity reacts to gravity changes in vitro. Front Neurosci 2023; 17: 1085282

Strumwasser F. Long-term recording from single neurons in brain of unrestrained mammals. Science 1958; 127: 469–470

Subramanian M, Chiang CC, Couturier NH, Durand DM. Theta waves, neural spikes and seizures can propagate by ephaptic coupling in vivo. Exp Neurol 2022; 354: 114109

Taga A, Dastgheyb R, Habela C, Joseph J, Richard JP, Gross SK, Lauria G, Lee G, Haughey N, Maragakis NJ. Role of Human-Induced Pluripotent Stem Cell-Derived Spinal Cord Astrocytes in the Functional Maturation of Motor Neurons in a Multielectrode Array System. Stem Cells Transl Med 2019; 8: 1272–1285

Takahashi K, Tanabe K, Ohnuki M, Narita M, Ichisaka T, Tomoda K, Yamanaka S. Induction of Pluripotent Stem Cells from Adult Human Fibroblasts by Defined Factors. Cell 2007; 131: 861–872

Takahashi K, Yamanaka S. Induction of Pluripotent Stem Cells from Mouse Embryonic and Adult Fibroblast Cultures by Defined Factors. Cell 2006; 126: 663–676

Tau GZ, Peterson BS. Normal development of brain circuits. Neuropsychopharmacology 2010; 35: 147–168

Taylor AM, Blurton-Jones M, Rhee SW, Cribbs DH, Cotman CW, Jeon NL. A microfluidic culture platform for CNS axonal injury, regeneration and transport. Nat Methods 2005; 2: 599–605

Tehovnik EJ. Electrical stimulation of neural tissue to evoke behavioral responses. J Neurosci Methods 1996; 65: 1–17

Teppola H, Aćimović J, Linne ML. Unique Features of Network Bursts Emerge From the Complex Interplay of Excitatory and Inhibitory Receptors in Rat Neocortical Networks. Front Cell Neurosci 2019; 13: 464549

The pandas development team. pandas-dev/pandas: Pandas. 2020.

Thomas CA, Springer PA, Loeb GE, Berwald-Netter Y, Okun LM. A miniature microelectrode array to monitor the bioelectric activity of cultured cells. Exp Cell Res 1972; 74: 61–66

Thompson AC, Stoddart PR, Jansen ED. Optical Stimulation of Neurons. Curr Mol Imaging 2014; 3: 162–177

Tibau E, Ludl AA, Rudiger S, Orlandi JG, Soriano J. Neuronal Spatial Arrangement Shapes Effective Connectivity Traits of in vitro Cortical Networks. IEEE Trans Netw Sci Eng 2020; 7: 435–448

Tsien RY. New Calcium Indicators and Buffers with High Selectivity Against Magnesium and Protons: Design, Synthesis, and Properties of Prototype Structures. Biochemistry 1980; 19: 2396–2404

Veeraraghavan R, Gourdie RG, Poelzing S. Mechanisms of cardiac conduction: A history of revisions. Am J Physiol Heart Circ Physiol 2014; 306: 619–627

Veeraraghavan R, Hoeker GS, Laviada AA, Hoagland D, Wan X, King DR, Alonso JS, Chen C, Jourdan J, Isom LL, Deschenes I, Smith JW, Gorelik J, Poelzing S, Gourdie RG. The adhesion function of the sodium channel beta subunit (β1) contributes to cardiac action potential propagation. Elife 2018; 7: e37610

Virtanen P, Gommers R, Oliphant TE, Haberland M, Reddy T, Cournapeau D, Burovski E, Peterson P, Weckesser W, Bright J, van der Walt SJ, Brett M, Wilson

J, Millman KJ, Mayorov N, Nelson ARJ, Jones E, Kern R, Larson E, Carey CJ, Polat İ, Feng Y, Moore EW, VanderPlas J, Laxalde D, Perktold J, Cimrman R, Henriksen I, Quintero EA, Harris CR, Archibald AM, Ribeiro AH, Pedregosa F, van Mulbregt P, Vijaykumar A, Bardelli A Pietro, Rothberg A, Hilboll A, Kloeckner A, Scopatz A, Lee A, Rokem A, Woods CN, Fulton C, Masson C, Häggström C, Fitzgerald C, Nicholson DA, Hagen DR, Pasechnik D V., Olivetti E, Martin E, Wieser E, Silva F, Lenders F, Wilhelm F, Young G, Price GA, Ingold GL, Allen GE, Lee GR, Audren H, Probst I, Dietrich JP, Silterra J, Webber JT, Slavič J, Nothman J, Buchner J, Kulick J, Schönberger JL, de Miranda Cardoso JV, Reimer J, Harrington J, Rodríguez JLC, Nunez-Iglesias J, Kuczynski J, Tritz K, Thoma M, Newville M, Kümmerer M, Bolingbroke M, Tartre M, Pak M, Smith NJ, Nowaczyk N, Shebanov N, Pavlyk O, Brodtkorb PA, Lee P, McGibbon RT, Feldbauer R, Lewis S, Tygier S, Sievert S, Vigna S, Peterson S, More S, et al. SciPy 1.0: fundamental algorithms for scientific computing in Python. Nat Methods 2020; 17: 261–272

Vroman R, Klaassen LJ, Kamermans M. Ephap tic communication in the vertebrate retina. Front Hum Neurosci 2013; 7: 60704

Wagenaar DA, Pine J, Potter SM. Searching for plasticity in dissociated cortical cultures on multi-electrode arrays. J Negat Results Biomed 2006; 5: 16

Wang B, Ke W, Guang J, Chen G, Yin L, Deng S, He Q, Liu Y, He T, Zheng R, Jiang Y, Zhang X, Li T, Luan G, Lu HD, Zhang M, Zhang X, Shu Y. Firing frequency maxima of fast-spiking neurons in human, monkey, and mouse neocortex. Front Cell Neurosci 2016; 10: 219052

Wang IE, Clandinin TR. The Influence of Wiring Economy on Nervous System Evolution. Current Biology 2016; 26: R1101–R1108

Warm D, Schroer J, Sinning A. Gabaergic Interneurons in Early Brain Development: Conducting and Orchestrated by Cortical Network Activity. Front Mol Neurosci 2022; 14: 807969

Waskom M. seaborn: statistical data visualization. J Open Source Softw 2021; 6: 3021

Watanabe K, Ueno M, Kamiya D, Nishiyama A, Matsumura M, Wataya T, Takahashi JB, Nishikawa S, Nishikawa SI, Muguruma K, Sasai Y. A ROCK inhibitor permits survival of dissociated human embryonic stem cells. Nat Biotechnol 2007; 25: 681–686

Wei N, Tolkacheva EG. Mechanisms of arrhythmia termination during acute myocardial ischemia: Role of ephaptic coupling and complex geometry of border zone. PLoS One 2022; 17: e0264570

Weiss SA, Faber DS. Field effects in the CNS play functional roles. Front Neural Circuits 2010; 4: 1541

Weydert S, Girardin S, Cui X, Zürcher S, Peter T, Wirz R, Sterner O, Stauffer F, Aebersold MJ, Tanner S, Thompson-Steckel G, Forró C, Tosatti S, Vörös J. A Versatile Protein and Cell Patterning Method Suitable for Long-Term Neural Cultures. Langmuir 2019; 35: 2966–2975

Wilk N, Habibey R, Golabchi A, Latifi S, Ingebrandt S, Blau A. Selective comparison of gelling agents as neural cell culture matrices for long-term microelectrode array electrophysiology. OCL 2016; 23: D117

Williams LA, Davis-Dusenbery BN, Eggan KC. SnapShot: Directed Differentiation of Pluripotent Stem Cells. Cell 2012; 149: 1174-1174.e1

Wollseiffen P, Klein T, Vogt T, Abeln V, Strüder HK, Stuckenschneider T, Sanders M, Claassen JAHR, Askew CD, Carnahan H, Schneider S. Neurocognitive performance is enhanced during short periods of microgravity - Part 2. Physiol Behav 2019; 207: 48–54

Yamamoto H, Moriya S, Ide K, Hayakawa T, Akima H, Sato S, Kubota S, Tanii T, Niwano M, Teller S, Soriano J, Hirano-Iwata A. Impact of modular organization on dynamical richness in cortical networks. Sci Adv 2018; 4: eaau4914

Yang Y, Cui Y, Sang K, Dong Y, Ni Z, Ma S, Hu H. Ketamine blocks bursting in the lateral habenula to rapidly relieve depression. Nature 2018; 554: 317–322

Yu Y, Zeng Z, Xie D, Chen R, Sha Y, Huang S, Cai W, Chen W, Li W, Ke R, Sun T. Interneuron origin and molecular diversity in the human fetal brain. Nature Neuroscience 2021 24:12 2021; 24: 1745–1756

Yuan J, Yankner BA. Apoptosis in the nervous system. Nature 2000; 407: 802–809

Yuan X, Schröter M, Obien MEJ, Fiscella M, Gong W, Kikuchi T, Odawara A, Noji S, Suzuki I, Takahashi J, Hierlemann A, Frey U. Versatile live-cell activity analysis platform for characterization of neuronal dynamics at single-cell and network level. Nat Commun 2020; 11: 4854

Yuste R. From the neuron doctrine to neural networks. Nat Rev Neurosci 2015; 16: 487–497

Zafeiriou MP, Bao G, Hudson J, Halder R, Blenkle A, Schreiber MK, Fischer A, Schild D, Zimmermann WH. Developmental GABA polarity switch and neuronal plasticity in Bioengineered Neuronal Organoids. Nat Commun 2020; 11: 3791

Zecevic N, Hu F, Jakovcevski I. Interneurons in the developing human neocortex. Dev Neurobiol 2011; 71: 18–33

Zeldenrust F, Wadman WJ, Englitz B. Neural coding with bursts - Current state and future perspectives. Front Comput Neurosci 2018; 12: 341146

Zhang Y, Pak CH, Han Y, Ahlenius H, Zhang Z, Chanda S, Marro S, Patzke C, Acuna C, Covy J, Xu W, Yang N, Danko T, Chen L, Wernig M, Südhof TC. Rapid single-step induction of functional neurons from human pluripotent stem cells. Neuron 2013; 78: 785–798

Zoghbi HY. Diseases of the Nervous System. In: Kandel ER, Koester JD, Mack SH, Siegelbaum SA, eds. Principles of Neural Science New York: McGraw Hill, 2021: 1417–1581

9. Appendix

9.1 Supplementary Information

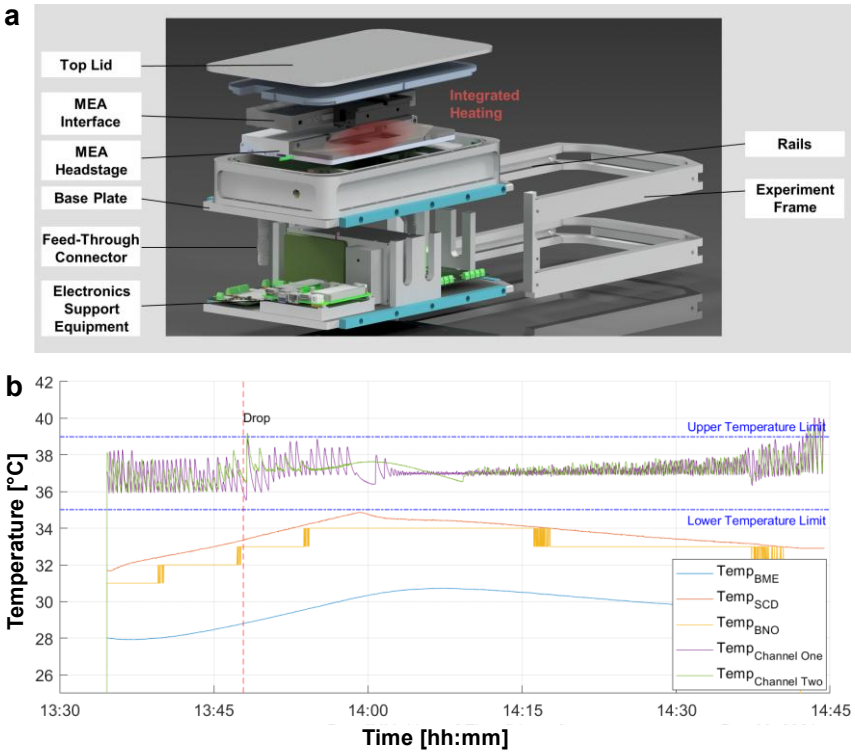

Supplementary Figure 1: Environmental chamber setup for MEA-based electrophysiology during altered gravity experiments. a, Schematic of the experimental system used for MEA recordings in altered gravity environments showing key components. **b**, Representative temperature profiles recorded during a single drop tower session. Just before the drop (indicated by the red striped line) a15 min baseline recording is taken. Temperature measurements at the two MEA chips are shown in purple and green, while additional traces represent readings from other positions within the pressure chamber. *Figure adapted from Striebel et al. (2023); original data and visualization generated by the Maximilian Sturm.*

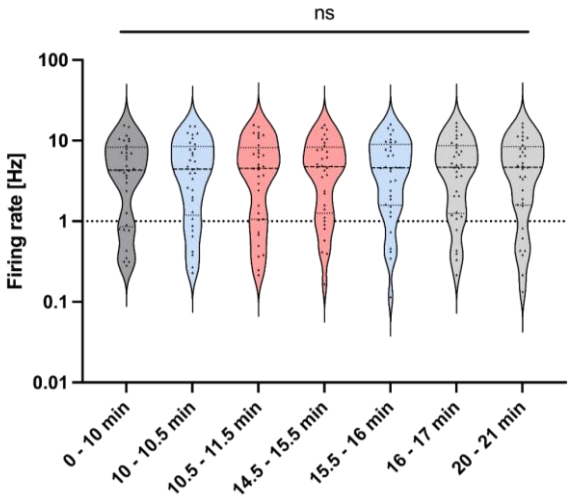

Supplementary Figure 2: Stability of electrophysiological activity in human neuronal networks maintained at 1 *g* across different time intervals. To assess baseline stability in long-term MEA recordings, firing rates were analyzed during defined time windows corresponding to those used in the centrifugation experiment (compare Supplementary Figure 3). Violin plots show the distribution of firing rates across seven temporal segments. Data were derived from 37 single units recorded across 5 MEAs (25–94 dpi) from five independent cultures. Each black triangle indicates the firing rate of an individual unit. Dashed lines represent the first, second (median), and third quartiles. Statistical comparisons with repeated measures one-way ANOVA and Tukey's multiple comparisons test revealed no significant differences (ns). *Figure adapted from Striebel et al. (2023); original data and visualization generated by the author.*

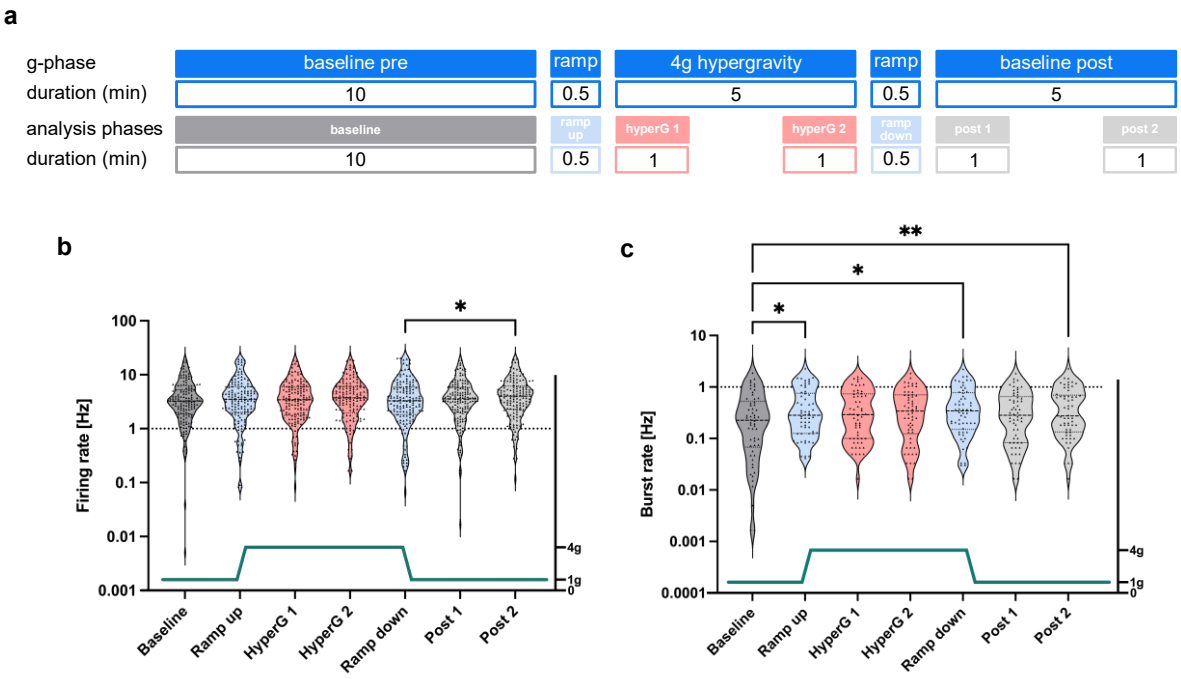

Supplementary Figure 3: Electrophysiological responses of human neuronal networks exposed to 4 *g* hypergravity. a, Schematic representation of the experimental protocol, outlining the various phases and the corresponding time intervals used for analysis. **b**,**c**, Spike rate (**b**) and burst rate (**c**) of neural cultures recorded during exposure to 4 *g* on a centrifuge. Each data point reflects activity recorded from five MEAs across five independent centrifugation experiments. A total of 153 units were included in the spike rate analysis and 58 in the burst rate assessment. Violin plots depict the distribution of activity, with dashed lines indicating the first, second, and third quartiles. Significant changes relative to baseline are denoted (Repeated measures one-way ANOVA and Tukey's multiple comparisons test, *$p < 0.05$, **$p < 0.01$). *Figure adapted from Striebel et al. (2023); original data and visualization generated by the author.*

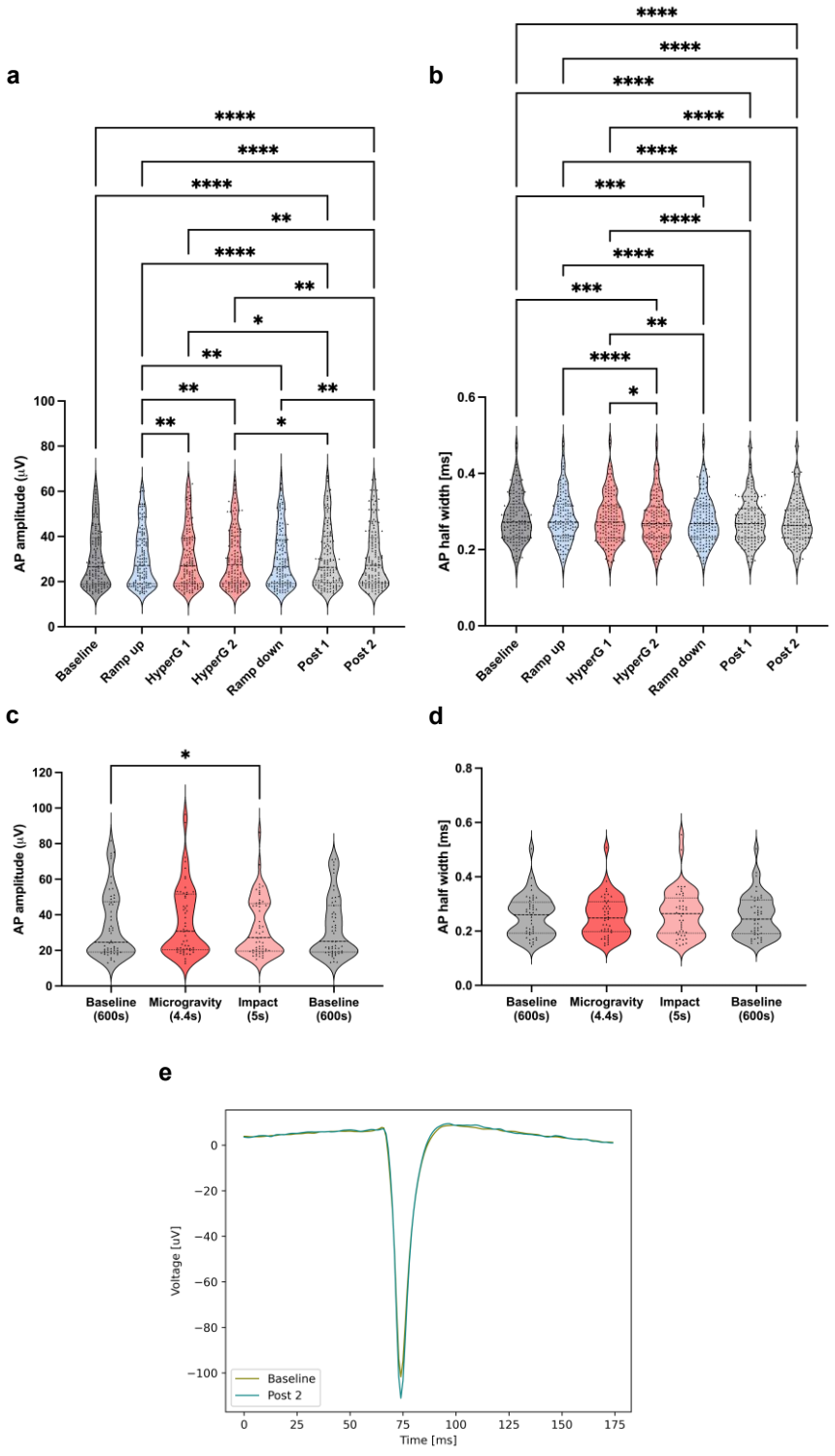

Supplementary Figure 4: Characterization of AP waveform features during altered gravity exposure in centrifuge and drop tower experiments. Waveform templates obtained from spike sorting were evaluated across different gravity conditions to assess potential changes in AP shape. **a**,**b**, AP amplitude (**a**) and half-width (**b**) of human neuronal cultures recorded under 6 *g* hypergravity using a centrifuge setup. **c**,**d**,

Corresponding waveform features recorded during microgravity exposure in the drop tower. **e**, Example of a single-unit waveform template illustrating changes between the baseline and post 2 phase. Waveform parameters were extracted using the SpikeInterface/Ironclust pipeline. Outliers were removed via the ROUT method (Q = 1 %), followed by Friedman's test for repeated measures. (ns = not significant, *$p < 0.05$, **$p < 0.01$, ***$p < 0.001$, ****$p < 0.0001$). *Figure adapted from Striebel et al. (2023); original data and visualization generated by the author.*

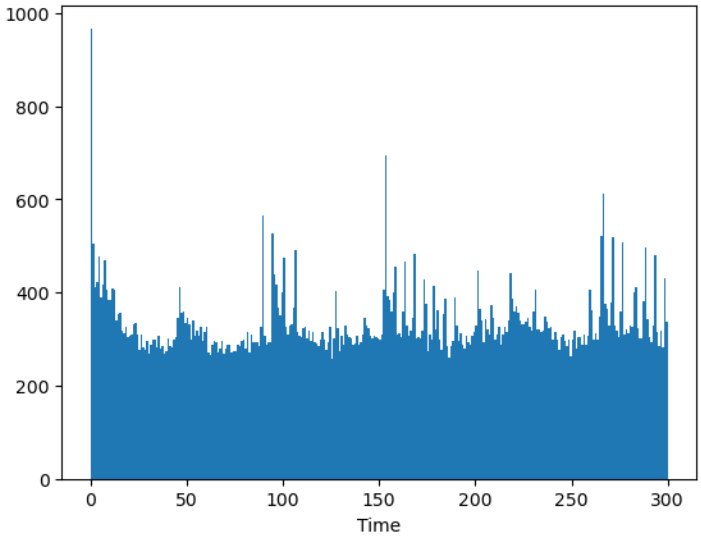

Supplementary Figure 5: Temporal distribution of spike activity following impact in the drop tower microgravity experiment. Spike timestamps from all drop tower runs were pooled and temporally aligned to the moment of capsule impact. A cumulative spike histogram covering the 300 s following impact was generated using 1 s time bins. A transient increase in firing rate was observed immediately after impact, which gradually returned to baseline levels within approximately 10–20 s. *Figure adapted from Striebel et al. (2023); original data and visualization generated by the author.*

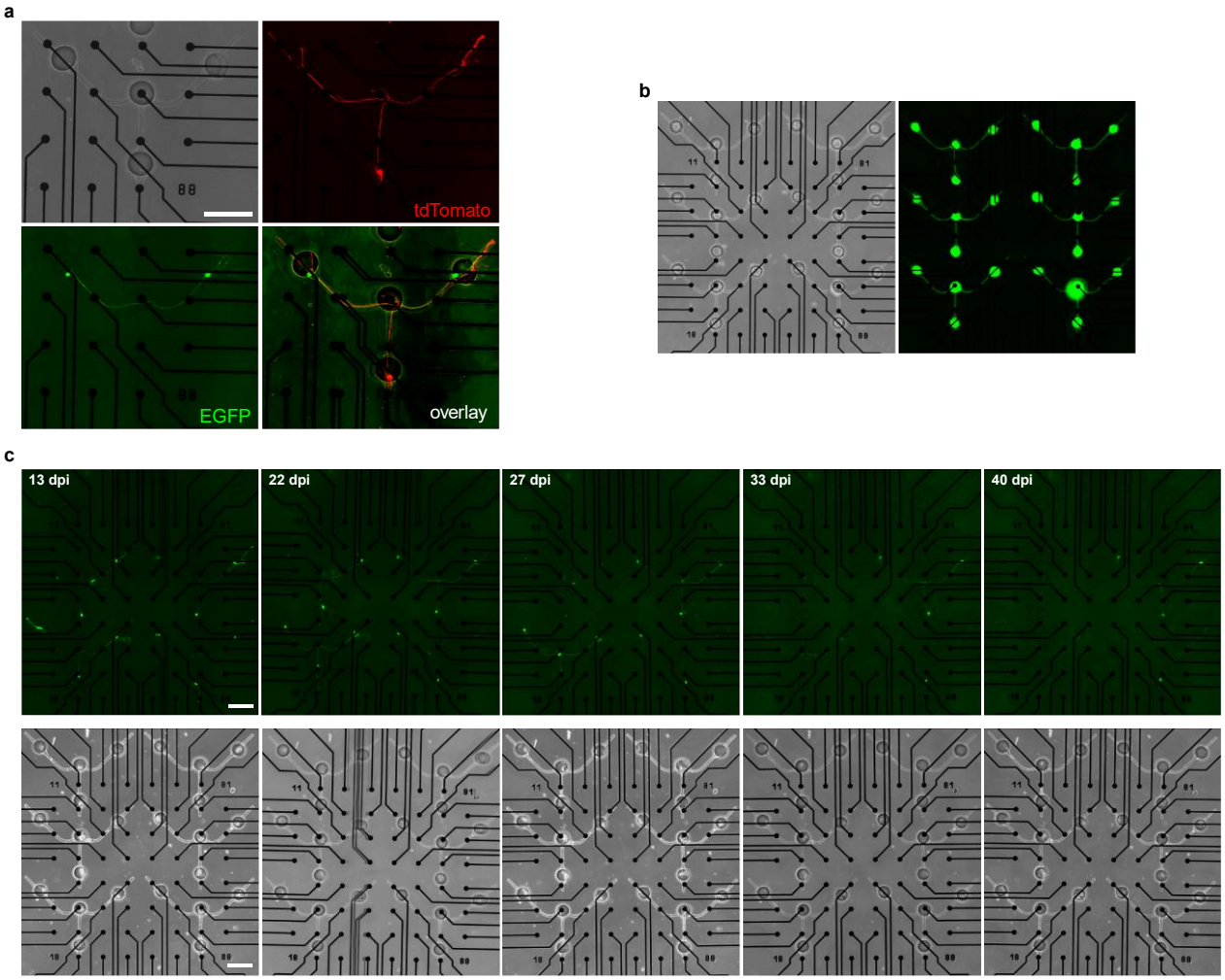

Supplementary Figure 6: Generation and maturation of SNAP motifs. a, Example of a defined SNAP circuit architecture composed of two neuronal subtypes: two iNGN neurons (in upper two microwells) and one EMX1 neuron (in the lower microwell), interconnected through microchannels. Fluorescence images show tdTomato expression in the EMX1 neuron and EGFP in iNGNs. **b**, Representative images (EGFP fluorescence and brightfield) of an MEA device seeded with iNGN populations embedded in a microfluidic system at 22 dpi. **c**, Time-lapse visualization of four Y-shaped microcircuits, each containing three iNGN neurons, developing on a single MEA (EGFP fluorescence and brightfield). Scale bars, 200 µm. *Figure reproduced from Striebel et al. (2025a); original data and visualization generated by the author.*

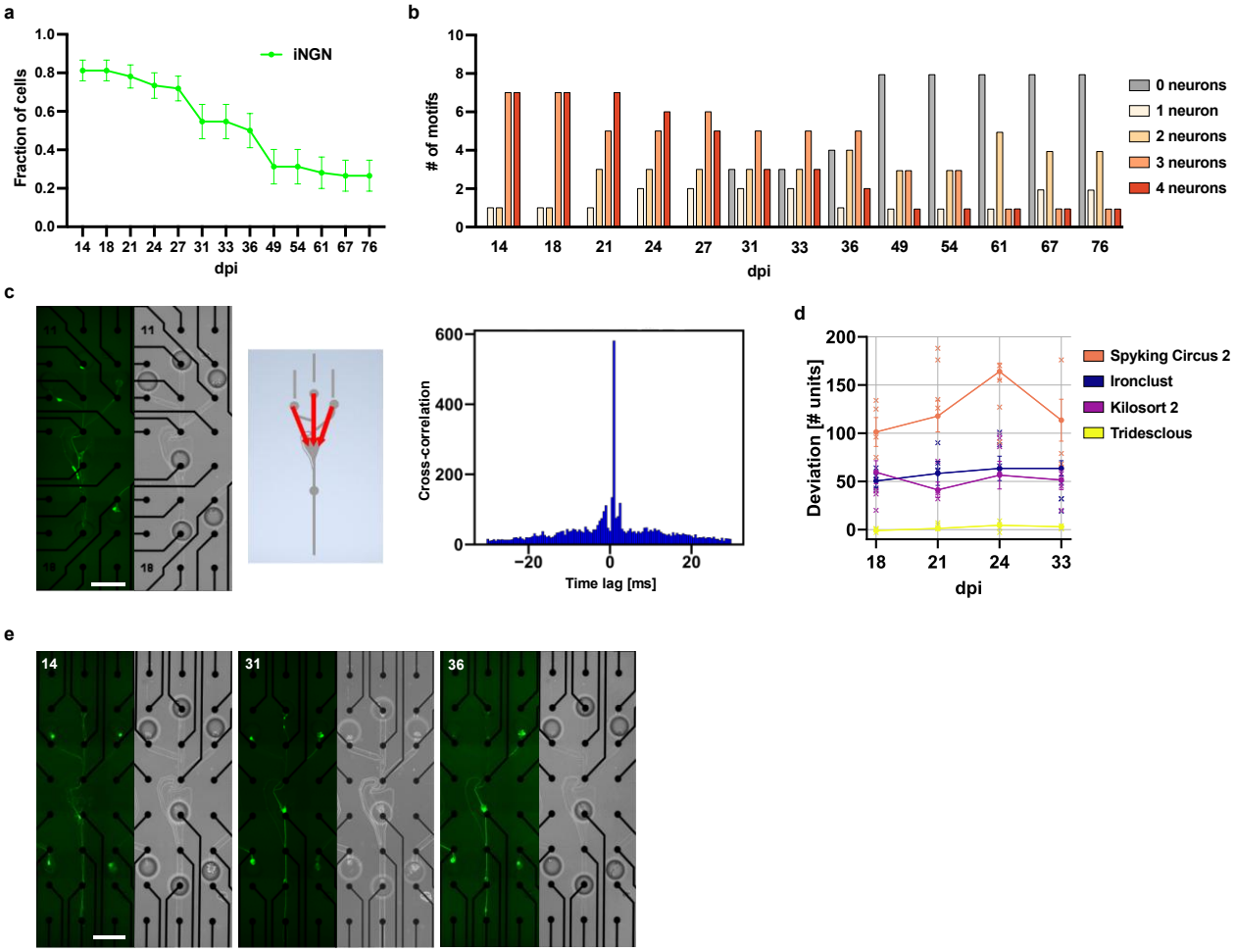

Supplementary Figure 7: Cell viability and signal processing in directional 4-iNGN SNAP microcircuits. a, Quantification of cell survival across several days post induction (dpi) in directional SNAP microcircuits composed of four iNGN neurons each (mean ± SEM, n = 16 circuits). **b**, Distribution of motifs containing 1–4 iNGN neurons per dpi. Data collected from four samples, each comprising four individual circuits. **c**, Example of signal propagation analysis within a directional circuit. Left: Fluorescence (EGFP) and brightfield image of the microfluidic structure. Middle: Schematic representation of the microchannel layout with arrows denoting the direction of AP propagation derived from cross-correlation analysis of electrode signals. Right: Example of cross-correlation from two electrode recordings in the same circuit. **d**, Evaluation of spike sorting algorithm accuracy in directional microcircuits. Four different algorithms were tested on data from four MEAs across four time points. The deviation from the ground truth (i.e., number of neurons identified in microscopy) was calculated to assess performance (mean ± SEM). **e**, EGFP fluorescence and brightfield images showing the structural development of the circuit motif displayed in Figure 3-12e. Timepoint in dpi denoted in upper left. Scale bars, 200 µm. *Figure reproduced from Striebel et al. (2025a); original data and visualization generated by the author.*

10. Statement of own contribution

The work presented here was carried out at the University Eye Hospital Bonn (Department of Ophthalmology, University of Bonn) under the supervision of Prof. Dr. Volker Busskamp.

The altered gravity study was designed in collaboration with Dr. Christian Liemersdorf, Laura Drouvé, Maximilian Sturm, and Dr. Yannick Lichterfeld from DLR (Cologne) as well as Nils Drouvé, Dr. Stefan Peters and Prof. Dr. Sherif El Sheikh from TH Cologne and Prof. Dr. Volker Busskamp. Experiment hardware was built by Maximilian Sturm. Culture of MEA samples was carried out by me. All other experiments were carried out by me in collaboration with Laura Drouvé, Maximilian Sturm, Nils Drouvé, Dr. Stefan Peters and Dr. Yannick Lichterfeld. Data processing, subsequent analyses, statistical evaluation, preparation of all figures expect Supplementary Figure 1 (all analysis and preparation by Maximilian Sturm) as well as interpretation were carried out by me with support from the previously mentioned team.

The study on development of *in vitro* networks was designed and lead by Dr. Rouhollah Habibey in collaboration with me and Prof. Dr. Volker Busskamp. All experiments were carried out by Dr. Rouhollah Habibey and supported by me. Spike sorting was carried out by me. Analysis, statistical evaluation, figure preparation and interpretation were done by Dr. Rouhollah Habibey in collaboration with me.

The *in vitro* learning experiment was ideated by me. Concept and methodology was further developed by me in collaboration with Dr. Christoph Miehl. All experiments were carried out by me. Data processing, analyses, statistical evaluation and interpretation were carried out by me with support from Dr. Christoph Miehl.

The study on ephpatic coupling in reproducible circuits at single-neuron resolution was designed in collaboration with my supervisor Prof. Dr. Volker Busskamp. All experiments, data processing and subsequent analyses as well as statistical evaluation, figure preparation and interpretation of results were carried out by me. EMX1 cells were provided by Alex H. M. Ng. Nucleofection of EMX1 cells with the tdTomato construct was carried out by Dr. Julia Pawlick. FACS sorting after nucleofection was carried out by the Flow Cytometry Core Facility with support of Mareike Eis. Direct laser writing of mircofluidic

master structures was done by Dr. Helge Gehring and Daniel Wendland at the University of Münster in the lab of Prof. Dr. Wolfram Pernice.

In preparing this work, I used DeepL and ChatGPT to improve the readability and language of the manuscript. After using the tools, I reviewed and edited the relevant passages and take full responsibility for the content of the published dissertation.

I confirm that I have written this thesis independently and have not used any sources or aids other than those specified by me.

I hereby confirm that my thesis complies with the Statement by the Executive Committee of the Deutsche Forschungsgemeinschaft (DFG, German Research Foundation) on the Influence of Generative Models of Text and Image Creation on Science and the Humanities and on the DFG’s Funding Activities.

11. Acknowledgements

This thesis would not have been possible without the guidance and support of many people.

First and foremost, I would like to sincerely thank my supervisor, Prof. Dr. Volker Busskamp, for his guidance and support, throughout my thesis. His expertise and mentorship were invaluable in shaping both the scientific direction and the overall experience during this time. The freedom and encouragement to pursue ideas and projects were very important to me and the overall development of the work.

I sincerely thank my thesis advisory committee consisting of Prof. Dr. Andreas Offenhäusser, Prof. Dr. Heinz Beck, and Prof. Dr. Dr. Florian Mormann for their insightful comments and guidance, which helped improve both the scientific content and clarity of this work.

I am grateful to the entire team of the Busskamp lab for creating an inspiring and collaborative environment, for their constant support in day-to-day research and for making this time unforgettable and fun. Especially I want to thank Dr. Rouhollah Habibey for his support and expertise that made this thesis possible. Special thanks go to Dr. Sarah Kunze and Dr. Kirsten Harmening for their technical assistance. Thanks also go to Dr. Kritika Sharma, Dr. Julia Pawlick, Dr. Robert Prior, and Elizaveta Podoliak, Mareike Eis, Melissa Meinert, and Jasmin Zorn, for their support.

I would also like to thank our collaborators at DLR and TH Cologne, especially Dr. Christian Liemersdorf, Laura Drouvé, Maximilian Sturm, Nils Drouvé, Dr. Stefan Peters and Dr. Yannick Lichterfeld. Further I thank the ESA Education Office and especially Dr. Nigel Savage and Jeffrey Gorissen for their continuous support and advice during the preparation of the experiment and the drop tower campaign.

Thanks to the lab of Prof. Dr. Wolfram Pernice at University of Münster and University of Heidelberg and especially to Dr. Helge Gehring and Daniel Wendland for their support in microstructure fabrication. I want to thank my collaboration partners at the University of Chicago, especially Prof. Dr. Brent Doiron and Dr. Christoph Miehl for their valuable discussions, constructive feedback and hosting me as a visiting scholar. I also want to thank Dr. Johannes Kirchner for the insightful discussions. Thanks go to Alex Ng, Ph.D., for sharing his cell lines.

I am also grateful to the Gene Editing Core Facility at the University Hospital Bonn, particularly Dr. Simon Schneider and Angela Egert, for their technical support. Thanks also go to the Flow Cytometry Core Facility of the Universtiy Hospital Bonn.
I acknowledge financial support from the Joachim Herz Foundation and the ESA Education Office as part of the Drop Your Thesis! program.
Thanks to the Bonn International Graduate School of Neuroscience for the support and the educational opportunities.
Thanks also go to Dr. Matthias Häußler, Dr. Johannes Kirchner, Dr. Philip Kohlmann and Christine Striebel for proofreading.
Above all, I owe my deepest thanks to my wife for her unwavering support, patience, and encouragement throughout this journey. I am also profoundly grateful to my family and friends, whose understanding and motivation carried me through the challenging and rewarding moments of this thesis.

12. List of publications

Striebel J, Habibey R, Wendland D, Gehring H, Podoliak E, Pawlick JS, Sharma K, Ng AHM, Pernice W, Busskamp V. Reproducible Human Neural Circuits Printed with Single-Cell Precision Reveal Functional Roles of Ephaptic Coupling. ACS Nano 2025; in press

Striebel J, Habibey R, Wendland D, Gehring H, Podoliak E, Pawlick JS, Sharma K, Ng AHM, Pernice W, Busskamp V. Empirical validation of ephaptic coupling in printed human neural circuits. bioRxiv 2025; 10.1101/2025.05.21.655141

Habibey R, Striebel J, Meinert M, Latiftikhereshki R, Schmieder F, Nasiri R, Latifi S. Engineered modular neuronal networks-on-chip represent structure-function relationship. Biosens Bioelectron 2024; 261: 116518

Gontier C, Kalinski L, Striebel J, Sturm M, Meerholz Z, Schunk S, Lichterfeld Y, Liemersdorf C. A computational model of altered neuronal activity in altered gravity. bioRxiv 2024; 10.1101/2024.07.30.605832

Striebel J, Kalinski L, Sturm M, Drouvé N, Peters S, Lichterfeld Y, Habibey R, Hauslage J, El Sheikh S, Busskamp V, Liemersdorf C. Human neural network activity reacts to gravity changes in vitro. Front Neurosci 2023; 17: 1085282

Habibey R, Striebel J, Latiftikhereshki R, Schmieder F, Latifi S. Microengineered 2D and 3D modular neuronal networks represent structure-function relationship. bioRxiv 2023; 10.1101/2023.04.07.535751

Habibey R, Jesús J, Arias ER, Striebel J, Busskamp V. Microfluidics for Neuronal Cell and Circuit Engineering. Chem Rev 2022; 122: 14842-14880

Habibey R, Striebel J, Schmieder F, Czarske J, Busskamp V. Long-term morphological and functional dynamics of human stem cell-derived neuronal networks on high-density micro-electrode arrays. Front Neurosci 2022; 16: 951964

Habibey R, Striebel J, Sharma K, Busskamp V. Optogenetic Control of Human Stem Cell-Derived Neurons. In: Gordeliy V, eds. Rhodopsin. Methods in Molecular Biology. New York: Humana, 2022; 2501: 339–360

Schmieder F, Habibey R, Striebel J, Büttner L, Czarske J, Busskamp V. Tracking connectivity maps in human stem cell-derived neuronal networks by holographic optogenetics. Life Sci Alliance 2022; 5: e202101268

Zuzic M, Striebel J, Pawlick JS, Sharma K, Holz FG, Busskamp V. Gene-independent therapeutic interventions to maintain and restore light sensitivity in degenerating photoreceptors. Prog Retin Eye Res 2022; 90: 101065

Liu S, Striebel J, Pasquini G, Ng AHM, Khoshakhlagh P, Church GM, Busskamp V. Neuronal Cell-type Engineering by Transcriptional Activation. Front Genome Ed 2021; 3: 22

Striebel J, Vorobii M, Kumar R, Liu H-Y, Yang B, Weishaupt C, Rodriguez-Emmenegger C, Fuchs H, Hirtz M, Riehemann K. Controlled Surface Adhesion of Macrophages via Patterned Antifouling Polymer Brushes. Adv Nanobiomed Res 2021; 1: 2000029